The Influence of Charge Geometry on the Response of Cylinders to Internal Air Blasting

Sean Davids (DVDSEA004)

Dissertation presented in part fulfilment of the degree of Master of Science in Mechanical Engineering

BLAST IMPACT AND SURVIVABILITY RESEARCH UNIT

Department of Mechanical Engineering

University of Cape Town

Supervisor: Professor Genevieve Langdon

Plagiarism Declaration

I, Sean Davids (DVDSEA004), hereby declare that this dissertation is my original work (except where acknowledgements indicate otherwise) and that neither the whole work nor any part of it has been, is being, or will be submitted for another degree to this or any other university. I hereby authorise the University of Cape Town to reproduce this work, either in full or in portion, for the purpose of research.

SIGNED: Sean Davids (DVDSEA004) DATE: 9 February 2016

Abstract

The effect of charge geometry on the structural response of right circular cylinders, subjected to internal blast loading, was investigated. Thin-walled, seamless 304 stainless steel cylinders were subjected to blast loads from partially confined bare cylindrical PE4 charges with different diameter and aspect ratios (charges length to charge diameter). The diameters of interest were:

- 25 mm (aspect ratios of 0.5 – 3).
- 30 mm (aspect ratios of 0.5 –1.6).
- 35 mm (aspect ratios of 0.5 – 1.1).
- 40 mm (aspect ratios of 0.5 – 0.9).

The effect of aspect ratio, for the constant diameter or constant mass cases, on the structural response of the cylinders (that is, diametric deflection, axial impulse, and axial shortening) is reported. Cylindrical charges with an aspect ratio of 1, were compared to spherical charges of equivalent mass.

For charges with constant diameter with varying length:

- The diametric deflection increased with increasing aspect ratio.
- The axial shortening increased with increasing aspect ratio.
- The axial impulse increased with increasing aspect ratio.

For charges with constant mass with varying diameter and length:

- The long charges (that is, charges with aspect ratios greater than 1) caused larger diametric deflections than their mass equivalent short (that is, charges with aspect ratios less than 1) charges. This is because the long charges had more side effective charge mass (that is, the mass of the charge that contributes directly to the diametric deflection of a cylinder) than the shorter charges.
- The short charges transferred more axial impulse to the ballistic pendulum, because they had more axial effective charge mass (that is, the mass of the charge that contributes directly to the axial impulse that is transferred to a ballistic pendulum) than their mass equivalent long charges.

It was observed that a lighter charge can diametrically deflect a cylinder more effectively than a heavier charge, if its side effective charge mass is greater than that of the heavier charge. The structural responses of the cylinders obtained from cylindrical charge detonations were greater than those obtained from the

mass equivalent spherical charge detonations. The deflections resulting from the cylindrical charges were also more localised compared to the spherical charges.

To gain insight into phenomena that could not be captured experimentally (for example, transient deflection and pressure), the experiments were simulated as an axisymmetric model in LS DYNA, a commercial numerical modelling package. Results from Vickers hardness and quasi-static tensile tests showed that the properties obtained were highly repeatable, and were incorporated in the Johnson-Cook model in the numerical simulation to characterise the material. The model gave good correlation to the experimental data, and predicted similar trends. The model revealed that:

- The longer charges produced more diametric deflections than their mass equivalent shorter charges because a high pressure zone ($P \geq 50MPa$) developed at the cylinder wall that covered a larger area, and had a longer duration.
- Cylindrical charges had more directional blast wave propagation, toward the cylinder wall, compared to the spherical propagation from the spherical charge.

Acknowledgements

First and foremost, all the glory, honour, praise, worship, power and thanks goes to the Almighty God. I thank Him for helping me to write this dissertation, and for helping me with my many endeavours in life. The following people are also acknowledged:

- My supervisor Prof. Genevieve Langdon: for making time to see me, advising me through my dissertation, and being one of my lecturers while I was a mechanical engineering undergraduate at the University of Cape Town.
- To the Mechanical Engineering workshop staff: Horst Emrich, Peter Jacobs, Gavin Doolings, Grant Springle, Brendon Daniels, Tyrone Newins, Dillon Jacobs, Pierre Smith, Hubert Tomlinson, and Willie Slaverse.
- To the staff at the UCT School of Architecture: especially John Coetzee.
- To the Centre of Materials Engineering staff: Penny Park-Ross, and Dr Sarah George.
- To Avatar Solutions staff: especially Michelle Bettie.
- To the staff at NDE Stainless Steel: especially Ron Pikker.
- To the people who were fellow postgraduates at the Blast Impact and Survivability Unit, while I did my M.Sc. coursework and dissertation: Richard Curry, Christopher Long, Sherlyn Gabriel, Ismail Ghoor, Dale Warncke, Dustin Fischer, Kelsey Hilton, Lee-Ann Welgemoed, Matthew Weyer, Alessandro Scribani, Ian Gallagher, Andrew Roginsky, Vinay Shekhar, Paul Shangase, and James Stock.
- To the lecturers who taught me my undergraduate coursework subjects from 2006–2011: Prof. Robert Knutsen, Prof. Gerald Nurick, Prof. Christiaan Redelinghuys, Prof. Ramesh Kuppuswamy, Prof. Chris von Klemperer, Mr Trevor Cloete, Mr Dirk Findeis, Mr Ernesto Ismail, Dr George Vicatos, Prof. Kevin Bennett, Prof. Jasson Gryzagoridis, Prof. Franz-Josef Kahlen, Prof. Robert Tait, Mr Marlan Perumal, Dr Howard Pearce, Dr Steeve Chung Kum Yuen, Mr Pierre Le Roux, Mrs Kalpana Kanjee, Mrs Evelyn Vicatos, Mr Adrian Jongens, Mr Roger Wood, Prof. Candice Laing, and Mr Alan Rynhoud.
- To the lecturers and who taught me my postgraduate coursework subjects from 2014–2015: Prof. Daya Reddy, Dr Sebastian Skatulla, Dr Andrew McBride, Kevin Sacks, Prof. Sue Harrison, Prof. Jean-Paul Franzidis, and Dr Miroslava Topic.

- To my fiancé Robin-Lee Johnston: for loving, supporting and encouraging me during this period in my life. Most of all, I thank her for coming into my life, and for the many sacrifices that she made, especially when I was not always able to spend time with her while I did my courses and wrote my dissertation. I am excited to be your husband God willing.
- To my parents Bernadette and James Davids: for doing their part to bring me into this world, for giving me a good school and university education, and for being the best parents that a son could ever have.
- To my brother Nathan Davids: for being supportive and for being a true friend.
- To the companies who sponsored me and made this dissertation possible: Armscor, the National Research Foundation, and the Centre for Scientific and Industrial Research.
- Computations were performed using facilities provided by the Blast Impact and Survivability Research Unit: `http://www.bisru.uct.ac.za`, and the University of Cape Town's ICTS High Performance Computing team: `http://hpc.uct.ac.za`.

This dissertation is dedicated to my grandparents who are alive and well: Ma Susan Pretorius (b. 22^{nd} December 1928), Pa Charles Davids (b. 10^{th} October 1930), and Ma Joanne Davids (b. 8^{th} August 1932).

Contents

Plagiarism Declaration i

Abstract ii

Acknowledgements iv

List of Tables x

List of Figures xiii

1 Introduction 1
- 1.1 Background . . . 2
- 1.2 Aim . . . 2
- 1.3 Outline . . . 3

2 Literature Review 4
- 2.1 Explosions . . . 5
  - 2.1.1 Definition . . . 5
  - 2.1.2 Types . . . 5
  - 2.1.3 Chemical Sources . . . 5
  - 2.1.4 Ideal Pressure History . . . 6
  - 2.1.5 Blast Scaling . . . 7
  - 2.1.6 TNT Equivalence . . . 9
- 2.2 Detonations . . . 10
  - 2.2.1 Comparison to Combustion and Deflagration . . . 10
  - 2.2.2 ZND Model . . . 10
  - 2.2.3 CJ State . . . 11
- 2.3 Cylindrical Charges . . . 13
  - 2.3.1 Effective Charge Mass . . . 13
  - 2.3.2 Ideal Detonation Velocity . . . 14
- 2.4 Confinement . . . 15
  - 2.4.1 Blast Load Categories . . . 15
  - 2.4.2 Gas Pressure and Afterburn . . . 16
- 2.5 Structural Response of Cylinders . . . 20
  - 2.5.1 Foundational Studies . . . 20

2.5.2 Recent Studies . . . 31

3 Blast Experimental Methodology **36**
3.1 Test Rig . . . 37
3.1.1 Explosive Material . . . 37
3.1.2 Ballistic Pendulum . . . 37
3.1.3 Cylinders . . . 38
3.1.4 Polystyrene Bridge . . . 39
3.2 Charge Matrix . . . 41

4 Experimental Results **42**
4.1 Tabulated Data . . . 43
4.2 Cylinder Profile . . . 44
4.2.1 Pictures . . . 44
4.2.2 Maximum Diametric Deflection . . . 47
4.2.3 Axial Shortening and Secondary Bulge Formation . . . 52
4.3 Axial Impulses . . . 54
4.4 Repeatability Tests . . . 56
4.5 Charge Geometry . . . 58
4.6 Detonator Position . . . 60

5 Material Characterisation **62**
5.1 Vickers Hardness Testing . . . 63
5.1.1 Description . . . 63
5.1.2 Results . . . 64
5.2 Quasi-Static Tensile Testing . . . 66
5.2.1 Curved Specimens and the Insert Design . . . 66
5.2.2 Force-Travel Data Processing . . . 67
5.2.3 Stress-Strain Data Processing . . . 68

6 Simulated Blast Model Development **73**
6.1 Air Mesh Sensitivity Study . . . 74
6.1.1 General . . . 74
6.1.2 Simulated Air, Explosive and Boss . . . 76
6.1.3 Simulated Impulse Calculation Methodology . . . 78
6.1.4 Richardson Extrapolation . . . 79
6.1.5 Air Mesh Sensitivity Results . . . 80
6.2 Cylinder Mesh Sensitivity Study . . . 81
6.2.1 General . . . 81
6.2.2 Simulated Cylinder . . . 82
6.2.3 Cylinder Mesh Sensitivity Results . . . 85

7 Numerical Simulation Results **86**
7.1 Tabulated Data . . . 87
7.2 Cylinder Profile . . . 88
7.2.1 Node Plots . . . 88
7.2.2 Maximum Diametric Deflection . . . 90
7.2.3 Axial Shortening and Secondary Bulge Formation . . . 94
7.2.4 Profile Comparison . . . 96
7.3 Axial Impulses . . . 98
7.3.1 Plotted Data . . . 98
7.3.2 Averaged Peak Pressure . . . 100
7.4 Charge Geometry . . . 103
7.5 Detonator Position . . . 106

8 Conclusions **108**

9 Recommendations **111**

References **114**

A Ballistic Pendulum Impulse Inference **A-1**
A.1 Derivations . . . A-2
A.1.1 The Homogeneous Differential Equation . . . A-2
A.1.2 General Solution . . . A-2
A.1.3 Under Damped Case Solution . . . A-4
A.2 Impulse Calculation Methodology . . . A-6
A.2.1 The Oscilloscope Method . . . A-6
A.2.2 The Pen Method . . . A-8
A.2.3 Correlation of Pen and Oscilloscope Method Impulses . . . A-11

B Raw Data **B-1**
B.1 Maximum Diametric Deflection . . . B-2
B.2 Axial Shortening . . . B-3

C Code **C-1**
C.1 LS DYNA Blast Keyword File (Base Units: g, mm, ms, and K) . . . C-2
C.2 Averaged Cylinder Profile . . . C-5
C.3 Richardson Extrapolation . . . C-7
C.4 Pendulum-Oscilloscope Impulse Calculator . . . C-8

D Assessment of Ethics in Research Projects Form **D-1**

List of Tables

2.1 Examples of Primary Explosives [1] . . . 5
2.2 Examples of Secondary Explosives [1] . . . 6
2.3 Parameters Used in Each Annealed Mild Steel Cylinder Test [2] . . . 24
2.4 Parameters Used in the 304 Stainless Steel Cylinder Validations [2] . . . 25

3.1 Polystyrene Bridge Dimensions for the Charge Diameters Used Herein . . . 40
3.2 Matrix of Charge Specifications for Each Test . . . 41

4.1 Experimental Data Table . . . 43
4.2 Proportionality of Effective Charge Mass to Maximum Deflection and Impulse . . . 49
4.3 Repeatability Test Results (10g_25d_0.5) . . . 57
4.4 Repeatability Test Results (17g_30d_0.5) . . . 57
4.5 Comparison of Loading and Responses from Tests with Cylindrical (Aspect Ratio = 1) and Mass Equivalent Spherical Charges . . . 58
4.6 Deflections, Impulses, and Shortenings of Cylindrical and Mass Equivalent Spherical Charges 61

5.1 Vickers Hardness Test Results (HV Units in kg/mm^2) . . . 64
5.2 0.2% Engineering Yield Stress, UTS, and Fracture Strains . . . 70
5.3 Final Johnson-Cook Parameters . . . 72

6.1 Cylindrical Charge Container Geometry Maxima and Minima . . . 75
6.2 JWL EOS and CJ State Parameters Values [3] . . . 76
6.3 Comparison of Detonation Velocities with respect to RDX Percentage . . . 76
6.4 Parameters Used to Capture Air Behaviour [4] . . . 78
6.5 ALE Mesh Sensitity Test Results . . . 80
6.6 Johnson-Cook Parameters [5, 6, 7] and Other Material Properties . . . 82
6.7 Grüneisen EOS Values [5] . . . 83
6.8 ALE and Lagrangian Mesh Sensitivity Results . . . 85

7.1 Tabulated Simulated Results . . . 87
7.2 Comparison of Simulated and Experimental Maximum Diametric Deflections . . . 91
7.3 Comparison of Simulated and Experimental Axial Shortenings . . . 95
7.4 Comparison Simulated and Experimental Impulses . . . 99
7.5 Comparison of Simulated and Experimental Data (Spherical and Cylindrical Charges, $R_{ld} = 1$) . . . 106

7.6 Comparison of Simulated and Experimental Data of 34g_30d_1 Charges (Different Det. Pos.) 107

A.1 The Effect of Damping on ζ A-3
A.2 Horizontal Position of the Pendulum with respect to Time (1^{st} Cycle) A-5
A.3 Ballistic Pendulum Constants A-6
A.4 Sixth Order Polynomial Fit Parameters for Clipped Displacement Histories A-8
A.5 Impulse Data Comparison (Pen and Oscilloscope Methods) A-11

B.1 Maximum Diametric Deflection Measurements B-2
B.2 Axial Shortening Measurements B-3

List of Figures

2.1 Idealised Pressure History [8, 9] 6
2.2 The Similarity Principle [10, 11] 8
2.3 Hugoniot Curves of Unreacted Explosives and Detonation Products [12] 11
2.4 Schematic Showing the Conical Mass of the Charge Contributes to the Axial Impulse [10, 13] 13
2.5 Graph of Asymptotic Convergence of Detonation Velocity and Critical Charge Diameter [12] 14
2.6 Pictorial Presentation of the Blast Load Categories [14] 15
2.7 Shock and Gas Pressure Trendlines with respect to Time [14] 17
2.8 Schematic of Cubicle Geometry Reported by Feldgun and Co-workers [15, 16, 17] 17
2.9 Effect of Afterburn on the Pressure History of a Sensor for a 4 kg TNT Charge [16, 17] . 18
2.10 Localisation of the Deformation after Loading by Pentolite Charges [18] 20
2.11 Schematic Showing the Test Rig Used by Proctor and Wise [18] 21
2.12 Comparison of the Radial Strains for Air and Water Filled Cylinders [18] 22
2.13 Geometry of the Problem Investigated by Duffey and Mitchell [2] 22
2.14 Experimental - Theoretical Correlation of a Mild Steel Cylinder Loaded by $50g$ C4 [2] . . 25
2.15 Experiment - Theory Correlation of a 304 Stainless Steel Cylinder Loaded by $50g$ C4 [2] . 26
2.16 Schematic Showing Cylinder Geometry Investigated by Benham and Duffey [19] 26
2.17 Assumed Pressure History According to Benham and Duffey [19] 27
2.18 Schematic Showing Cross-Section of the Test Rig Used by Benham and Duffey [19] 29
2.19 Comparison of the Theoretical Solutions to the Experimental Data [19] 29
2.20 Graph of Strain Ratio *vs* $\bar{\eta}$, Showing Experimental Correlation With the Theory, Proposed in Ref. [19] 30
2.21 Layout of the Test Rig Used by Schleyer and Rushton [20, 21] 31
2.22 Effect of Changing Charge Dimensions on Circumferential Strain (1 kg Charge) [20] . . . 32
2.23 Fractured Cylinders After Loading by 1.225, 1.3, and 1.5 kg PE4 [21] 32
2.24 Spherical Charge Positions used by Ozinsky *et al.* [22, 23] 33
2.25 Graph of Radial Deflection *vs* Charge Mass, From Ozinsky *et al.* [22, 23] 34
2.26 Experimental-Numerical Correlation of the Impulse Transfer Values [22, 23] 35

3.1 Schematic of Test Rig 37
3.2 Schematic of Cylinder, Boss, Clamp, and Mounting Plate 38
3.3 Photo Showing Marker Layout on Specimens 39
3.4 Schematic of Bridge Design (Dimensions on Table 3.1) 40

4.1 Photographs of Cylinders Blast Loaded by 25 *mm* Cylindrical Charges (Diameters After Testing in Brackets) . . . 44
4.2 Photographs of Cylinders Blast Loaded by 30 *mm* Cylindrical Charges (Diameters After Testing in Brackets) . . . 45
4.3 Photographs of Cylinders Blast Loaded by 35 *mm* Cylindrical Charges (Diameters After Testing in Brackets) . . . 46
4.4 Photographs of Cylinders Blast Loaded by 40 *mm* Cylindrical Charges (Diameters After Testing in Brackets) . . . 46
4.5 Graphs of Maximum Diametric Deflection *vs* Aspect Ratio . . . 47
4.6 Side Effective Charge Mass Comparison – 64g_40d_0.8, 54g_30d_1.6, and 49g_25d_2.5 Charges (Green Represents the Axial Effective Mass, and White is the Side Effective Mass) . . . 50
4.7 Pictorial Comparison of 64g_40d_0.8, 54g_30d_1.6, and 49g_25d_2.5 Cylinders . . . 50
4.8 Graph of Maximum Diametric Deflection *vs* Side Effective Charge Mass . . . 51
4.9 Ruptured Cylinders . . . 51
4.10 Photographs Showing Axial Shortening of, and Secondary Bulge Formation on a Cylinder (64g_40d_0.8) . . . 52
4.11 Graph of Axial Shortening (Constant Diameter *vs* Maximum Diametric Deflection . . . 53
4.12 Graphs of Axial Impulse *vs* Aspect Ratio . . . 54
4.13 Proportionality of Axial Impulse to Axial Effective Charge Mass (Constant Diameter) . . . 55
4.14 Effect of Increasing Axial Effective Charge Mass on the Impulse (Green Represents the Axial Effective Charge Mass) . . . 56
4.15 Photographs of Original and Repeatability Test Cylinders (10g_25d_0.5) . . . 56
4.16 Photographs of Original and Repeatability Test Cylinders (17g_30d_0.5) . . . 57
4.17 Photographs of Cylinders Loaded with Cylindrical and Mass Equivalent Spherical Charges ($R_{ld} = 1$) . . . 58
4.18 Superposed Schematics of 34 *g* Cylindrical and Spherical Charges ($R_{ld} = 1$) . . . 60
4.19 Cylinders Loaded by 34g_30d_1 Charges . . . 60

5.1 Dimensions of the Curved Specimen . . . 62
5.2 Vickers Hardness Test Schematic [24] (View of Indentation Also Shown) . . . 63
5.3 Schematic of the Curved Specimen Between the Inserts . . . 66
5.4 Raw Force-Displacment Curves . . . 67
5.5 Modified Force-Displacment Curves . . . 68
5.6 Corrected Force-Travel Curves . . . 69
5.7 Engineering Stress-Engineering Strain Curves . . . 69
5.8 True Stress-Plastic Strain Curves . . . 71

6.1 Schematic of the ALE Domain Used For the Air Mesh Sensitivity Test . . . 74
6.2 Detonation Velocity of Cyclotol 75/25 with Respect to Charge Diameter [12] . . . 77
6.3 Schematic of Elements at the Reflective Boundary Used to Record Pressure Histories . . . 78
6.4 Schematic of the Simulated Blast Model Domain . . . 81
6.5 Typical Displacement-Time Graph of a Node on Outer Radius of the Cylinder . . . 84

7.1 Simulated Profiles of Cylinders Loaded by 25 *mm* Diameter Charges . . . 88

7.2 Simulated Profiles of Cylinders Loaded by 30 mm Diameter Charges 88
7.3 Simulated Profiles of Cylinders Loaded by 35 mm Diameter Charges 89
7.4 Simulated Profiles of Cylinders Loaded by 40 mm Diameter Charges 89
7.5 Maximum Diametric Deflections (Simulated) 90
7.6 Blast Wave Propagation Comparison (43 g Charges) 92
7.7 Blast Wave Propagation (49g, 54g, and 64g Charges) 93
7.8 Simulated Axial Shortening and Secondary Bulge Formation (64g_40d_0.8 Simulation) . . 94
7.9 Blast Wave Superposition at the Clamped Region Causing Secondary Bulge Formation . . 94
7.10 PE4 Propagation During Secondary Bulge Formation 95
7.11 Graphs Showing the Comparison Between Simulated and Experimental Profiles 96
7.12 Axial Impulses (Simulated) 98
7.13 Pressure Contour Plots Comparison of Simulated Pressure (43 g Charges) 100
7.14 Simulated Peak Pressure (Constant Diameter) 100
7.15 Averaged Peak Pressure Histories Obtained Using LS DYNA (25 mm Charges) 101
7.16 Averaged Peak Pressure Histories Obtained Using LS DYNA (30 mm Charges) 102
7.17 Averaged Peak Pressure Histories Obtained Using LS DYNA (35 mm Charges) 102
7.18 Averaged Peak Pressure Histories Obtained Using LS DYNA (40 mm Charges) 103
7.19 Example of Force and Impulse Histories at Reflective Boundary (48g_30d_1.4) 103
7.20 Simulated Profiles of Cylinders Loaded by Detonations of 20 g Cylindrical and Spherical Charges 104
7.21 Simulated Profiles of Cylinders Loaded by Detonations of 34 g Cylindrical and Spherical Charges 104
7.22 Simulated Profiles of Cylinders Loaded by Detonations of 54 g Cylindrical and Spherical Charges 105
7.23 Simulated Blast Wave Propagation Shape After 0.01 ms 105
7.24 Simulated Profiles of Cylinders Affected by 34g_30d_1 Charges (Different Detonator Positions) 106
7.25 Pressure Wave Profile Shape of Cylindrical and Mass Equivalent Spherical Charge 107

A.1 Schematic drawing of the Ballistic Pendulum Oscillation [25] A-2
A.2 Damping Curves with respect to Time for the Same Initial Amplitude and Velocity A-4
A.3 Conversion of Voltage History to Displacement History (An Example) A-6
A.4 Graph Showing Voltage Histories 72g_40d_0.9 and 64g_40d_0.8 Tests (Minus Clipped Data) A-7
A.5 Parameters Used to Fit Polynomial to Displacement History A-8
A.6 Curve Fitting of Sixth Order Polynomial to Test 16 and 17 Displacement Histories A-8
A.7 Parity Graph of the Correlation of the Pen and Oscilloscope Impulses A-12

1

Introduction

1.1 Background

Explosions, whether deliberate or accidental, have devastating effects. Infrastructure damage and loss of life are often the consequences of these events. Studies have proven that increasing confinement leads to greater damage to infrastructure and civilians [25, 26, 27, 28]. The damage increase is caused by the the reflection of a blast wave off surfaces and its interaction with another blast wave, and the accumulation of detonation products that react with the remaining oxygen in the confined space (that is, afterburn) [14, 15, 16, 17]. Reflections lead to an increase in the peak blast pressure on surfaces, and afterburn leads to an accumulation of the gas (that is, quasi-static) pressure in the structure. The quasi-static pressure has a lower magnitude but higher duration than the initial blast wave, and is affected by the geometry, volume, and degree to which the structure confines a charge [14]. It is for these reasons that terrorists detonate bombs in confined structures such as elevators, vehicles and train tunnels, culverts and litter bins.

Subsequently, governments, companies, research institutions and law enforcement agencies have made it a priority to experimentally investigate blast phenomena in confined geometries. However, in many cases, cost and time constraints have limited the scale of these experiments. Fortunately, improvements in computational power, computer aided design software, and codes for finite element analysis and computational fluid dynamics have paved the way for cheaper alternatives to simulate experiments and real world events.

Ozinsky *et al.* [22, 23] investigated the structural response of seamless 304 stainless steel right circular cylinders to partially confined bare spherical PE4 charges. It is noted that PE4 is the British equivalent of C4 explosive, and that seamless implies that the cylinders were extruded, not seam welded. Ozinsky *et al.* [22, 23] reported that the charge mass and the charge position had an effect on the overall structural response of the cylinders.

In this dissertation, the work of Ozinsky *et al.* [22, 23] was extended to partially confined bare cylindrical PE4 charges with different aspect ratios (henceforth defined as the quotient of the charge length to diameter), to determine the effect of charge geometry on the structural response of right circular cylinders to internal air blasting. Bare spherical PE4 charges were detonated, and their effects on the same kind of cylinders were compared to mass equivalent cylindrical charges with an aspect ratio of 1. A preliminary investigation into the effect of detonator position, in a cylindrical charge, on a cylinders structural response was also conducted.

To gain insight into the structural response of the cylinders, with respect to transient physical quantities that could not be measured experimentally (for example, pressure and cylinder wall deflection), the experiments were simulated with a commercially available numerical modelling package. The simulated data was used in conjunction with the experimental data to explain how charge geometry and detonator position affected the structural response of cylinders to internal air blasting.

1.2 Aim

The overall aim of this investigation was to investigate the effect of charge geometry on the structural response of right circular cylinders to internal air blasting. This aim is divided into the following primary objectives:

- Objective 1: Investigate the effect of cylindrical charges, with different aspect ratios, on the structural response of right circular cylinders.
- Objective 2: Compare the effects of spherical and mass equivalent cylindrical charges, both with an aspect ratio of 1, on the structural response of right circular cylinders.
- Objective 3: Characterise seamless 304 stainless steel in the as received (that is, curved) state, and use the material properties in the simulated blast model.
- Objective 4: Simulate the experiments with a numerical modelling package to gain insight into time dependent phenomena that cannot be captured experimentally. Use the simulated data, in conjunction with the experimental data, to explain how charge geometry affects the structural response of right circular cylinders.

1.3 Outline

Chapter 2 provides the background to the current investigation. Chapter 3 describes the apparatus and methodology used to test the cylinders. Chapter 4 presents the results of the experiments. Chapter 5 describes the methods used to characterise the cylinder material, and presents the material properties that were used in the simulated blast model. Chapter 6 describes the development of the simulated blast model, where two mesh sensitivity studies are presented. Chapter 7 presents the simulated results and their correlation to the experimental data. Chapter 7 also uses the simulated data, in conjunction with the experimental data, to explain how charge geometry influences the structural response of right circular cylinders. Chapter 8 presents the conclusions of the investigation. Chapter 9 presents recommendations for future research based on the conclusions.

Appendix A presents the derivation of the equations that were used to infer the axial impulse that was transferred to the ballistic pendulum. Two impulse calculation methodologies are also presented here. Appendix B presents measurements of the maximum diametric deflections and axial shortenings before processing. Appendix C presents a reduced version of the input deck that was used for the final simulations, MATLAB codes of the Richardson Extrapolation algorithm, the averaged cylinder profile, and the oscilloscope method impulse calculation.

2

Literature Review

2.1 Explosions

2.1.1 Definition

An explosion is an event where energy is liberated almost instantaneously from an explosive, which causes a pressure wave to propagate in a medium [1, 9, 11]. Explosions are usually classified as physical, chemical or nuclear [1, 11].

2.1.2 Types

Nuclear explosions involve the transfer of protons and neutrons between atoms without affecting the surrounding electrons. Nuclear explosions are divided into fission and fusion. Fission is the splitting up of nuclei (for example, a neutron collides with fissile Uranium and breaks up to form Krypton and Barium), and fusion is the merging of nuclei (for example, two Hydrogen nuclei combine to form a Helium nucleus). Nuclear explosions liberate large quantities of energy in the form of gamma, infra-red, and ultraviolet radiation [1].

Physical explosions involve the transfer of energy from a high pressure region to a low pressure region (for example, volcanic activity or an over-pressurised vessel). Physical explosions liberate potential energy, which is converted into kinetic and thermal energy [1].

Chemical explosions are exothermic reactions that transfer electrons between atoms without affecting the atoms' nuclei. Chemical explosions typically have reaction times in the order of microseconds, activation temperatures in the order of hundreds of degrees Celsius (for example, the ignition temperature of TNT is 300°C), and pressures in the order of hundreds of Megapascals. Chemical explosions require heat, oxygen and fuel to liberate the internal energy, which is converted into kinetic, thermal, and chemical energy [1].

2.1.3 Chemical Sources

Chemical explosives are either classified according to their phase at room temperature (for example, solid, liquid, or gas), molecular group (for example, nitro compounds, nitric esters, nitramines, or azides), or their sensitivity to detonation (for example, primary high, and secondary high) [1, 9]. Akhavan [1] reports that explosives should be classified according to their sensitivity to detonation.

Primary explosives burn and detonate rapidly after encountering a heat source or an impact load. These kind of explosives are commonly used to activate secondary explosives [1]. Table 2.1 presents the names and chemical compositions of well known primary high explosives.

Table 2.1: Examples of Primary Explosives [1]

Name	**Composition**
Lead Azide	PbN_6
Mercury Fulimate	$(CNO)_2 Hg$
Lead Styphnate	$C_6H_3N_3O_9Pb$
Silver Azide	AgN_3
Tetrazine	$C_2H_8N_{10}O$

Secondary explosives do not detonate as easily as primary explosives. Detonations are initiated using a primary explosive [1]. Secondary explosives are more powerful and stable than primary explosives, thus,

making these explosives safer to handle, store over long periods, and use in blasting applications [22]. Table 2.2 presents the names and chemical compositions of common secondary explosives.

Table 2.2: Examples of Secondary Explosives [1]

Name	**Composition**
Research Department eXplosive (RDX/ Cyclonite)	$C_3H_6N_6O_6$
Nitroglycerine	$C_3H_5N_3O_9$
Tetryl	$C_7H_5N_5O_8$
Trinitrotoluene (TNT)	$C_7H_5N_3O_6$
Nitroguanidine	$CH_4N_4O_2$
Hexanitrostilbene (HNS)	$C_14H_6N_6O_{12}$

2.1.4 Ideal Pressure History

Figure 2.1 depicts an idealised pressure history, after an explosive was detonated in free air.

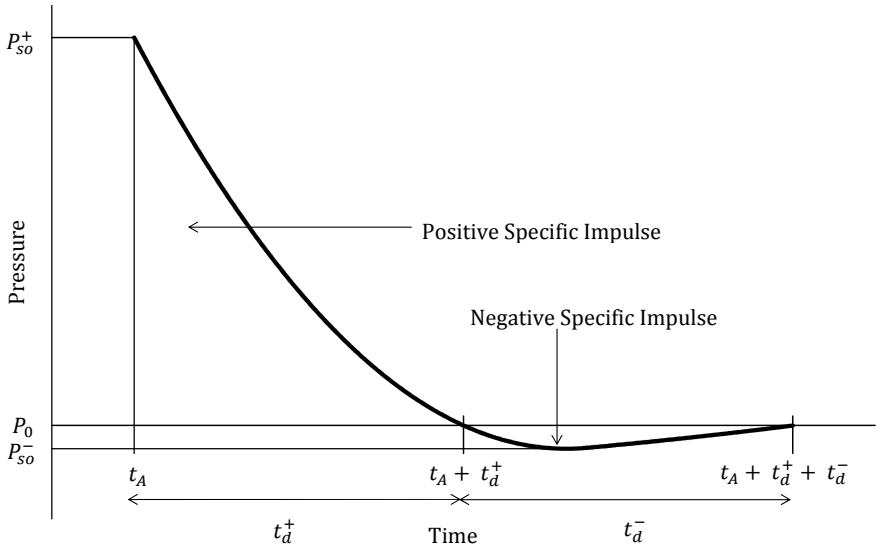

Figure 2.1: Idealised Pressure History [8, 9]

Before the pressure wave arrives (that is, $t < t_A$), the air particles are at rest, and the pressure is at atmosphere, P_0. When the pressure wave arrives (that is, $t = t_A$), the air particles expand almost instantaneously, and the pressure increases to a side on peak overpressure P_{so}^+. For the positive duration (that is, $t_A < t < t_A + t_d^+$), the pressure decreases quasi-exponentially to atmosphere [9]. At $t = t_A + t_d$, the instantaneous velocities of the particles are zero, and the absolute pressure is at atmosphere. For the negative duration (that is, $t_A + t_d < t < t_A + t_d + t_d^-$), the particles contract. As contraction occurs, the pressure reverses direction and becomes a vacuum, which decreases to a negative side on under pressure P_{so}^-. Thereafter, the pressure gradually increases to atmosphere [11].

The specific impulses are calculated using Equation 2.1 [11].

$$\begin{aligned} \text{positive specific impulse} \qquad I^{+} &= \int_{t_A}^{t_A+t_d^{+}} \left(P(t) - P_0\right)\, dt \\ \text{negative specific impulse} \qquad I^{-} &= \int_{t_A+t_d^{+}}^{t_A+t_d^{+}+t_d^{-}} \left(P_0 - P(t)\right)\, dt \end{aligned} \tag{2.1}$$

This idealised pressure history does not account for wave reflections, which amplify the peak overpressure. The mass of the explosive, stand-off distance (SOD) from an obstacle, the level and geometry of confinement, and the charge geometry will affect the peak overpressure and transient profile.

The Friedlander equation is a commonly fit equation to the positive specific impulse of ideal and non-ideal pressure histories. Equation 2.2 [8, 29] describes this.

$$P\left(t\right) = P_{SO}^{+}\left[1 - \frac{t}{t_d^{+}}\right] e^{\left(\frac{-\alpha t}{t_d^{+}}\right)} \tag{2.2}$$

Where t_d^{+} is the positive specific impulse duration time, and α is a parameter which describes the rate at which the pressure decays from the side on peak overpressure.

2.1.5 Blast Scaling

Scaled Distance

Full scale experiments can be time consuming and/ or costly to perform. To overcome these problems, scientists and engineers scale these experiments. The cube root method, which was developed by Hopkinson [11] is commonly used. The scaled distance is calculated using Equation 2.3.

$$Z = \frac{R}{W^{\frac{1}{3}}} \tag{2.3}$$

Where Z is the scaled distance (also known as the constant of proportionality), R is the stand off distance (SOD) in meters, and W is the mass of the explosive in kg TNT [8]. The method is based on the geometric similarity of spherical charges.

Figure 2.2 demonstrates the principle of geometric similarity of two spherical charges, which are at different stand off distance values. If the ratio of the charge masses is directly proportional to the cube of the ratio of the SOD values, the scaled distances of the charge 1 and 2 are the same (that is, $Z_1 = Z_2$). Hence, the pressure on obstacles 1 and 2 will be the same. The derivation of the scaled distance begins with Equation 2.4.

$$\frac{W_1}{W_2} = \left(\frac{R_1}{R_2}\right)^3 \tag{2.4}$$

Thus:

$$\left(\frac{W_1}{W_2}\right)^{\frac{1}{3}} = \frac{W_1^{\frac{1}{3}}}{W_2^{\frac{1}{3}}} = \frac{R_1}{R_2} \tag{2.5}$$

Finally:

$$\frac{R_2}{W_2^{\frac{1}{3}}} = \frac{R_1}{W_1^{\frac{1}{3}}} = Z \tag{2.6}$$

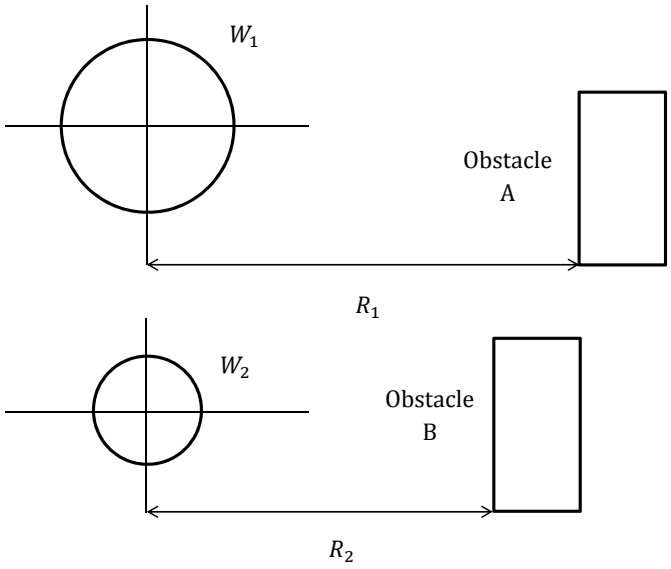

Figure 2.2: The Similarity Principle [10, 11]

Peak Side on Overpressure and Scaled Distance

Cube root scaling aids in the calculation of the side on peak overpressure. Different empirically derived peak side on overpressure equations, with respect to scaled distance, were developed.

Smith and Hetherington [8] presented the Brode equations for the peak side on overpressure, for near and far field effects, which are described by Equation 2.7.

$$\begin{aligned} P_{SO}^{+} = \frac{0.975}{Z} + \frac{1.455}{Z^2} + \frac{5.85}{Z^3} - 0.019 \text{ bar, for far field effects} \qquad & \left(0.1 < P_{SO}^{+} < 10\ bar\right) \\ P_{SO}^{+} = \frac{6.7}{Z^3} + 1 \text{ bar, for near field effects} \qquad & \left(10 < P_{SO}^{+}\ bar\right) \end{aligned} \tag{2.7}$$

Also, Smith and Hetherington [8] presented the Henrych equations for the peak side on overpressure, which are valid over a range of scaled distances. These equations are described by Equation 2.8.

$$\begin{aligned} P_{SO}^{+} &= \frac{14.072}{Z} + \frac{5.540}{Z^2} - \frac{0.357}{Z^3} + \frac{0.00625}{Z^4}\ bar \qquad \left(0.05 \leq Z < 0.3 \frac{m}{(kg)^{\frac{1}{3}}}\right) \\ P_{SO}^{+} &= \frac{6.194}{Z} - \frac{0.326}{Z^2} + \frac{2.132}{Z^3}\ bar \qquad \left(0.3 \leq Z < 1 \frac{m}{(kg)^{\frac{1}{3}}}\right) \\ P_{SO}^{+} &= \frac{0.662}{Z} + \frac{4.05}{Z^2} + \frac{3.288}{Z^3}\ bar \qquad \left(1 \leq Z < 10 \frac{m}{(kg)^{\frac{1}{3}}}\right) \end{aligned} \tag{2.8}$$

Kinney [9] presented a peak overpressure equation, for chemical explosions, which can be calculated using Equation 2.9.

$$P_{SO}^{+} = P_0 \frac{808\left[1+\left(\frac{Z}{4.5}\right)^2\right]}{\sqrt{\left(1+\left(\frac{Z}{0.048}\right)^2\right)\left(1+\left(\frac{Z}{0.32}\right)^2\right)\left(1+\left(\frac{Z}{1.35}\right)^2\right)}}\ bar \tag{2.9}$$

Mills [30] proposed another peak overpressure relation with respect to scaled distance, which is calculated using Equation 2.10.

$$P_{SO}^{+} = \frac{1}{100}\left(\frac{1772}{Z^3} - \frac{114}{Z^2} + \frac{108}{Z}\right)\ bar \tag{2.10}$$

These equations assume that TNT is used. To determine the scaled distance of non-TNT explosives, a TNT equivalent mass is required [8].

2.1.6 TNT Equivalence

The effectiveness of a blast load is determined by the magnitude of the energy released after an explosive decomposes [9], because the quantity of the energy affects the side on peak overpressure and the impulse. The TNT equivalence of an explosive is defined as the mass of TNT required to produce the same peak overpressure as that of any other explosive [31]. The Unified Facilities Criteria (UFC) manual [14] presented Equation 2.11.

$$W_E = \frac{H_{EXP}^d}{H_{TNT}^d} W_{EXP} \tag{2.11}$$

Where W_E is the mass of TNT, H_{TNT}^d is the TNT heat of detonation, W_{EXP} is the mass of the other explosive, and H_{EXP}^d is the detonation heat of the other charge. Cooper and Kurowski [32] presented Equation 2.12 as an alternative to Equation 2.11.

$$W_E = 0.078 W_{EXP} \frac{P_{CJ}}{D} \tag{2.12}$$

Where P_{CJ} is the Chapman-Jouget (CJ) state pressure, and D is the detonation velocity. Both physical quantities are specific to the explosive in question.

After conducting an experimental and numerical investigation into the TNT equivalence of buried PE4 charges. Weckert and Anderson [33] concluded that TNT equivalence depends on the measurement in question. Wharton *et al.* [46] reported that TNT equivalence varies greatly. In terms of peak overpressure and impulse, the United States Counterterrorism Centre [34] presents values of 1.3 and 1.5, respectively. Rigby and Sielicki [31] reported that 1.2 is the TNT equivalence value of spherical PE4. TNT equivalence is an ongoing field of research and has implications for studies where explosives are numerically modelled.

2.2 Detonations

2.2.1 Comparison to Combustion and Deflagration

Combustion is an exothermic chemical reaction that occurs when a substance is oxidised. Combustion involves the ignition of oxygen to form a flame, which increases the oxidation rate of the substance in question. Similar to combustion, deflagration is an exothermic reaction that occurs in the presence of oxygen. Deflagration reactions are subsonic, and are accompanied by a high pitched crack or hiss [1]. The deflagration rate is directly proportional to the confinement of the reaction, because the accumulation of gas (that is, quasi-static) pressure and the inability of the reactants to escape causes the reaction rate to accelerate. A detonation is a supersonic event that involves shock waves. These shock waves aid the decomposition of a substance [1]. Detonations cause explosions to occur.

2.2.2 ZND Model

Cooper [12], and Ficket and Davis [29] reported that the ideas behind the simple (also known as ZND) detonation model were independently developed by Zeldovich (1940), von-Neumann (1943), and Doering (1943). The ZND model is based on the following assumptions [12, 29]:

- The shock front travels in one direction.
- The effects of heat conduction, radiation, and diffusion are excluded from the analysis. Hence, the shock front is a discontinuous jump between states.
- The products are in chemical and thermodynamic equilibrium after detonation. Hence, the reaction is complete.
- The detonation velocity is constant, and the reaction moves with the shock front. Hence, the reaction is always in a steady state.
- The reaction rate is infinite, and the reaction zone length is zero.

2.2.3 CJ State

Figure 2.3 depicts the Hugoniot curves in the $P - v$ plane, of the reactants and products of an explosive. The Rayleigh line, which describes the jump discontinuity from the detonation reactant to the detonation product(s), intersects the Hugoniot of the detonation product(s), tangentially at point (B). If the Rayleigh line were to lay below the products Hugoniot curve, the discontinuous jump from the reactants to the products would exclude the Hugoniot. Point (B) is known as the CJ state, which was hypothesised by Chapman and Jouget in the 1800s as the steady state detonation point. The magnitude of the Rayleigh line slope is directly proportional to the shock front velocity, which for detonation phenomena is known as the detonation velocity D.

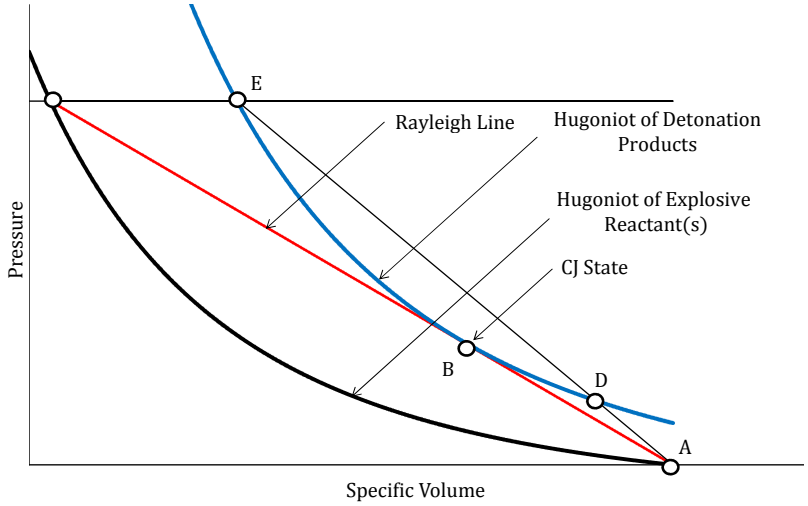

Figure 2.3: Hugoniot Curves of Unreacted Explosives and Detonation Products [12]

The ZND model states that the detonation velocity is constant, and the reaction moves with the shock front. At point (E), the magnitude of products Hugoniot slope is greater than the magnitude of the Rayleigh line slope. Hence, the shock front overtakes the reaction. This violates the ZND criterion. At point (D), the magnitude of the Hugoniot slope is less than the magnitude of the Rayleigh line slope. Hence, the reaction overtakes the shock front. This also violates the ZND criterion. Therefore, both states are ignored in favour of the CJ state, where all ZND criterion are met.

Thus, the mass conservation law is calculated using Equation 2.13.

$$\rho_{CJ} = \rho_0 \frac{D}{(D - u_{CJ})} \tag{2.13}$$

Where ρ_{CJ} and u_{CJ} is the density and particle velocity at the CJ state, respectively, and ρ_0 is the density of the explosive reactant(s). The momentum conservation is calculated using Equation 2.14.

$$P_{CJ} = \rho_0 D u_{CJ} \tag{2.14}$$

Where P_{CJ} is the pressure at the CJ state.

The energy conservation law is described by Equation 2.15.

$$e_{CJ} - e_0 = \frac{P_{CJ} u_{CJ}}{\rho_0 D} - \frac{1}{2} u_{CJ}^2 = \frac{1}{2} P_{CJ} \left(v_0 - v_{CJ} \right) \tag{2.15}$$

Where e_{CJ} and e_0 are the specific energies at the CJ and initial states, respectively, and v_0 and v_{CJ} are the specific volumes at the initial and CJ state, respectively. The conservation laws also assume that the shock front travels in one direction, as per the ZND criterion. The detonation velocity with respect to the velocity at the CJ state is calculated using Equation 2.16.

$$D = C_0 + s u_{CJ} \tag{2.16}$$

Where C_0 and s are experimentally determined coefficients. The pressure at the CJ state with respect to the velocity at the CJ state is calculated using Equation 2.17.

$$P_{CJ} = \rho_0 C_0 u_{CJ} + \rho_0 s u_{CJ}^2 \tag{2.17}$$

The Chapman Jouget pressure is an important parameter for numerically modelling explosives (in this dissertation, LS DYNA was used to simulate PE4 explosive — refer to Section 6.1.2.

2.3 Cylindrical Charges

2.3.1 Effective Charge Mass

The charge aspect ratio is defined by Equation 2.18.

$$R_{ld} = \frac{l}{d} \tag{2.18}$$

Where l is the charge length, and d is the charge diameter. Kennedy [13] reported that as the magnitude of the aspect ratio increases, the charge mass that contributes to the axial impulse transfer to a metal plate does not increase beyond a limit. Kennedy [13] stated that this effective charge mass is a cone with a 60˚angle, and the rest of the charge contributes to the "side losses". Figure 2.4 depicts two cylindrical charges with different aspect ratios, and their effective charge masses, on metal plates.

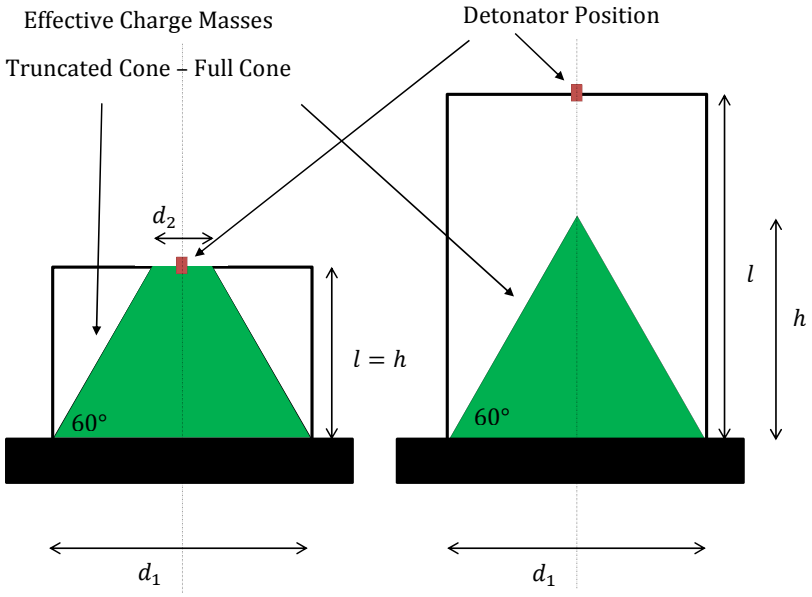

Figure 2.4: Schematic Showing the Conical Mass of the Charge Contributes to the Axial Impulse [10, 13]

The mass of a cylindrical charge is calculated using Equation 2.19.

$$m_{cyl} = \rho \frac{\pi d^2}{4} l \tag{2.19}$$

Where ρ is the density of the explosive, d is the charge diameter, and l is the charge length. The mass of a cone is calculated using Equation 2.20.

$$m_{con} = \rho V = \rho \frac{\pi}{12} \left(d_1^2 + d_1 d_2 + d_2^2\right) h \tag{2.20}$$

Where d_1 is the larger cone diameter, d_2 is the smaller cone diameter, and h is the cone height.

According to Kennedy [13], the magnitude of the aspect ratio, after which the axial impulse does not increase, is calculated using Equation 2.21.

$$R_{ld} = \frac{h}{d_1} = \frac{1}{2} tan\left(\frac{\pi}{3}\right) = \frac{\sqrt{3}}{2} \tag{2.21}$$

If the magnitude of the smaller cone diameter is not equal to zero, the effective charge mass will be a truncated cone. If the magnitude of the smaller cone diameter is zero, the effective charge mass will be a full cone. This is shown in the piecewise form of Equation 2.22.

$$R_{ld} \leq \frac{\sqrt{3}}{2} \texttt{ if } l = h \texttt{ and } d_2 \neq 0 \qquad \texttt{OTHERWISE} \qquad R_{ld} > \frac{\sqrt{3}}{2} \texttt{ if } l \geq h \texttt{ and } d_2 = 0 \tag{2.22}$$

It is also simply showed that for an aspect ratio of $\frac{\sqrt{3}}{2}$, the quotient of the effective charge mass to the actual charge mass is $\frac{1}{3}$.

2.3.2 Ideal Detonation Velocity

Cooper [12] reported that the change in detonation velocity is directly proportional to the change in charge diameter. At some diameter, the energy loss overtakes the energy produced, at which point, detonation fails to occur. This value is the critical charge diameter. As the diameter increases, the magnitude of the detonation velocity asymptotically converges to a value. This value is ideal detonation velocity. Equation 2.23 describes the relationship of the detonation velocity with respect to charge diameter [12].

$$D = D_\infty - W\frac{1}{d} \tag{2.23}$$

Where D_∞ is the ideal detonation velocity, and A is a constant. Both values are specific to each explosive. Note that when $d = W/D_\infty$, detonation will fail to occur. Figure 2.5 depicts an example of the asymptotic convergence of the detonation velocity as the charge diameter increases.

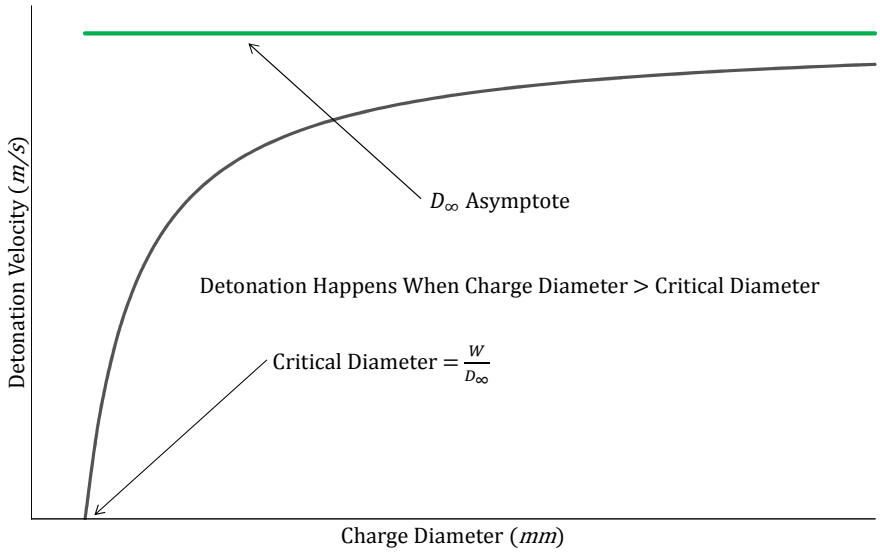

Figure 2.5: Graph of Asymptotic Convergence of Detonation Velocity and Critical Charge Diameter [12]

2.4 Confinement

2.4.1 Blast Load Categories

The UFC manual [14] reports that explosions are classified as either unconfined or confined. Each classification is further subdivided into three groups. Figure 2.6 depicts the subdivisions of the different blast load categories.

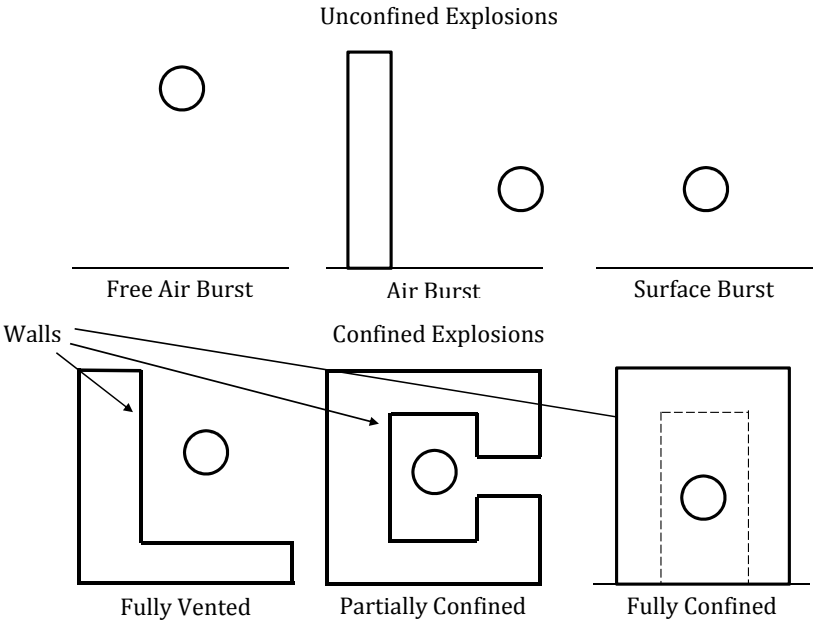

Figure 2.6: Pictorial Presentation of the Blast Load Categories [14]

Unconfined

- a free air burst explosion occurs above ground level, such that amplification of the initial pressure wave is negligible.
- an air burst explosion occurs such that the ground amplifies the initial pressure wave, before the structure encounters it.
- a surface burst explosion occurs close to or at ground level, such that the ground amplifies the pressure wave significantly.

Confined

- a fully vented explosion occurs when a charge is positioned adjacent to, or inside, a structure that has one or more surfaces open to the atmosphere. The walls of the structure withstands the blast, reflect and amplify the initial pressure wave. The detonation products, which were accumulated in the structure, are removed from the confined structure to the atmosphere (that is, leakage occurs) almost immediately. For fully vented explosives, Keenan and Tancreto [35] reported that Equation 2.24 should be satisfied.

$$\frac{A_{opening}}{V_{closed}^{\frac{2}{3}}} > 0.6 \tag{2.24}$$

Where $A_{opening}$ is the cross sectional area of the open end of the cylinder, V_{closed} is the volume of the cylinder if the explosive was fully confined.

- a partially confined explosion occurs when a charge is positioned within a structure, that has one or more gaps open to the atmosphere. The size of the gaps directly affects the magnitude of the gas pressure [14], and causes leakage which leads to the eventual restoration of the total pressure to atmospheric pressure. Keenan and Tancreto [35] reported that for partially confined explosives, Equation 2.25 should be satisfied.

$$\frac{A_{opening}}{V_{closed}^{\frac{2}{3}}} < 0.6 \tag{2.25}$$

- a fully confined explosion occurs when a charge is positioned in a structure with gaps that have negligible dimensions, which leads to insignificant leakage from the structure. The negligible gap dimensions also lead to the accumulation of gas pressure and high temperature detonation products. [14]. If the walls of the structure withstand the blast, post-detonation ventilation is crucial, because occupants who wish to open and enter an enclosed structure should proceed with caution as detonation products therein may be toxic (for example, the detonation products of Nitroglycerine) [1, 14].

2.4.2 Gas Pressure and Afterburn

UFC Manual [14]

Unconfined and fully vented explosions have much exposure to the atmosphere, which limits the temperature rise, accumulation of detonation products, and the gas pressure [14] duration and magnitude. However, partially and fully enclosed structures cause the accumulation of high temperature detonation products, and a significant gas pressure accumulation in the structure. This gas pressure has a smaller magnitude, yet a longer duration than the initial shock wave pressure. Figure 2.7 depicts the duration and magnitude of the gas pressure relative to those of the shock pressure.

Where P_s and T_s are the maximum shock pressure and duration, respectively, and P_g and T_g are the maximum gas pressure and duration, respectively. For partially and fully confined explosions, $T_g \ggg T_s$, and in the case of fully vented and unconfined explosions, $T_g \to 0$ [14], because the abundance of oxygen and the lack of charge confinement prevents detonation product and gas pressure accumulation.

Feldgun, and Co-workers et al. [15, 16, 17]

Feldgun, and co-workers *et al.* [15, 16, 17] conducted an experimental and numerical investigation into the behaviour of partially confined explosions in a cubicle, and the effect of charge mass to volume ratio on the pressure distribution. For the experimental component [15], a cubicle was constructed using high strength reinforced concrete. The walls were 350 mm thick, which allowed the authors [15] to assume that the walls were rigid throughout the investigation. Truncated corners, of 200 mm base and height,

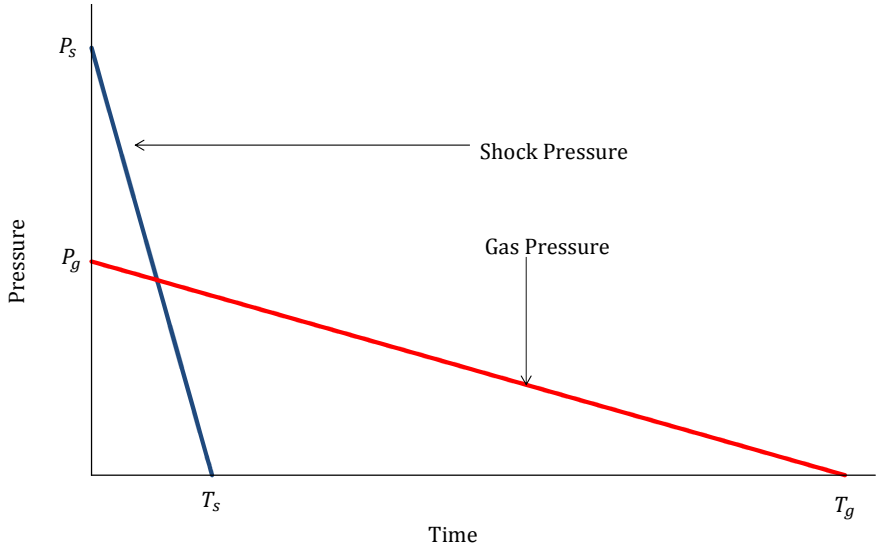

Figure 2.7: Shock and Gas Pressure Trendlines with respect to Time [14]

were included in the construction. Centrally located cubiodal TNT charges of different charge masses were detonated in the cubicle, which is depicted in Figure 2.8. Pressure sensors were placed at different locations in the cubicle, and pressure histories were collected.

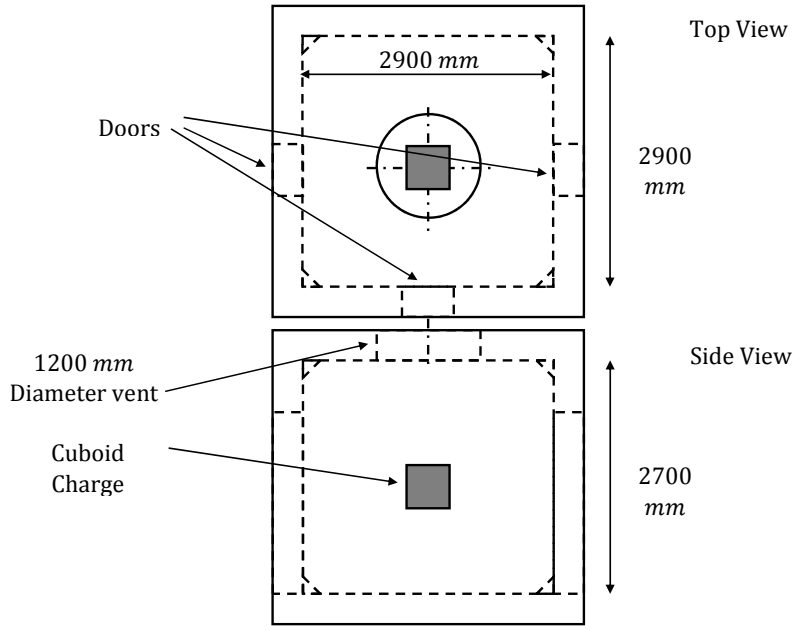

Figure 2.8: Schematic of Cubicle Geometry Reported by Feldgun and Co-workers [15, 16, 17]

The authors [15, 16, 17] reported that the ratio of the corner pressure to the centroid pressure was proportional to charge mass. For all charge masses, the corner pressure was always lower than the

centroid pressure, because the centroid sensor was closer to the detonation point than the corner sensor.

A numerical investigation was carried out to gain insight into the pressure distribution, where the authors [16] simulated the experiments with AUTODYN. The first peaks in the simulated pressure histories correlated well with that from the experiments, yet, subsequent peaks underpredicted, or were out of phase with, the experimental values [16]. This is shown in Figure 2.9(a) which depicts the simulated and experimental pressure histories from a pressure sensor, where afterburn was excluded, and the charge was 4 kg.

The lack of correlation motivated the need to investigate the effects of afterburn on the pressure histories and structural response of the cubicle. The authors [17] added afterburning effects to the simulations, and found that the correlation of the subsequent simulated peaks to the experimental peaks improved with respect to to magnitude and phase. Figure 2.9(b) depicts the simulated and experimental pressure histories, for the same sensor position and charge mass, where afterburning was included.

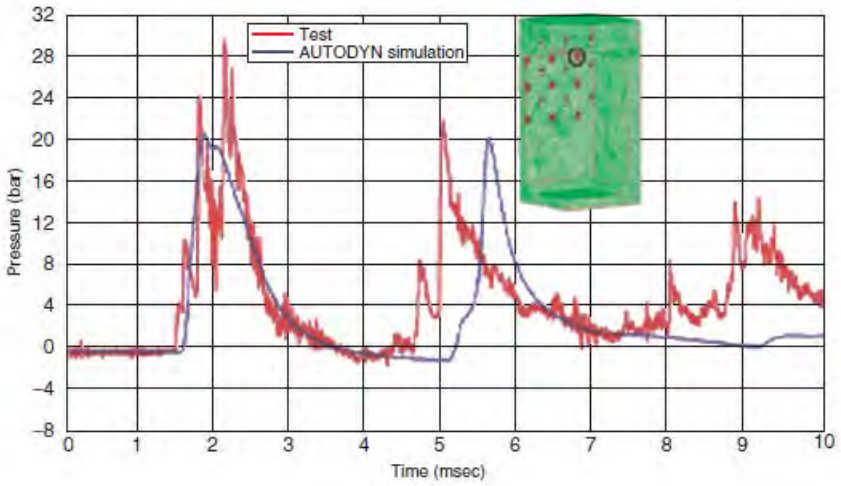

(a) Excluding Afterburn [16]

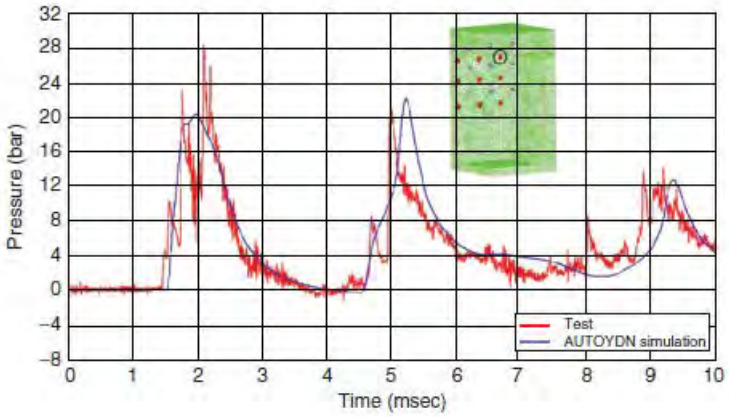

(b) Including Afterburning [17]

Figure 2.9: Effect of Afterburn on the Pressure History of a Sensor for a 4 kg TNT Charge [16, 17]

After an explosion, which occurs in the order of microseconds [1, 17], afterburning occurs when the detonation products of an explosive are ignited. This phenomenon is enhanced if the charge confinement is increased, because the gas pressure and temperature has more time to rise, and the detonation products are trapped in the confined space. As the initial shock wave is reflected off the non-breakable surfaces of a structure, the reflected shock wave interacts with the advancing air/ detonation product interface. If the detonation products are flammable, the oxygen content in the atmosphere is sufficient, and the temperature is high enough, an exothermic reaction (which happens in the order of milliseconds [1, 17]) will occur. This slower reaction is known as afterburn. The findings of Feldgun *et al.* [17] confirmed work by Neal *et al.* [36], who presented the results of an investigation into the effect of blast loading on spherical vessels.

2.5 Structural Response of Cylinders

2.5.1 Foundational Studies

Influence of Filling Media

Proctor and Wise [18] wanted to determine the containment ability of primary vessels in nuclear reactors, and to make information available to the nuclear engineering sector. Cube root scaling was used to relate the parameters associated with primary vessels to those of water or air filled cylinders. TNT and pentolite charges were used to simulate the loading that might arise from a nuclear incident [18]. General case equations were developed for impulse transfer and deformation work. The authors imposed the following constraints on the investigation:

- the cylinder's internal length with respect to its internal radius is given by $L \geq 4R_i$. This constraint was based on the localised deformation along $4R_i$ lengths of air or water filled cylinders. Figure 2.10 depicts this.

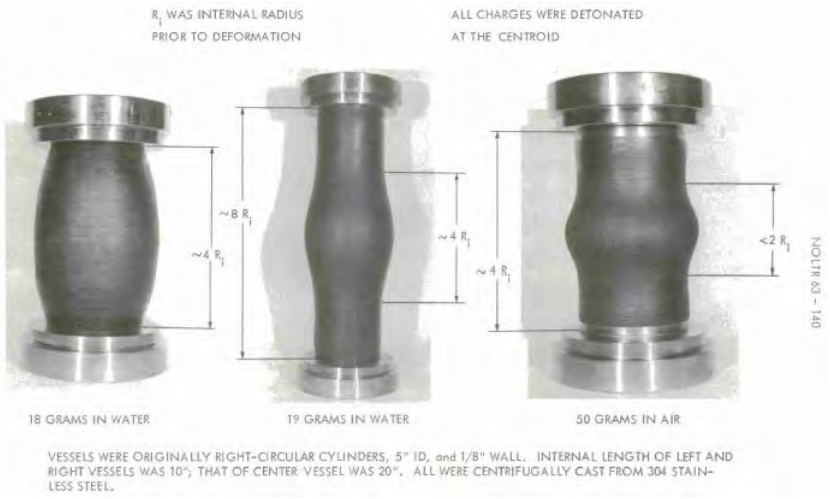

Figure 2.10: Localisation of the Deformation after Loading by Pentolite Charges [18]

- the cylinder's internal radius with respect to its wall thickness is described by $10 \leq \frac{R_i}{h_o} \leq 40$. The lower limit was based on thin cylinder theory, and the upper limit was selected for the investigation.
- the cylinder's internal radius with respect to its charge radius is described by $R_i \geq 4R_c$ based on the limited knowledge of the behaviour of air and water closer to the charge [18].
- the water is in a liquid state (that is, room temperature and atmospheric pressure) before, during, and after detonation. The authors justified ignoring the elevated pressure, because it was assumed that only the elastic strain energy would be affected. Hence, the plastic strain energy had preference in this investigation.
- the mechanical properties of the cylinder material are the same at every point (that is, homogeneous) and in every direction (that is, isotropic).

- only the tensile and shearing constraints in the cylinder wall retard the plastic deformation of the vessel.
- the cylindrical charges have unified aspect ratio, and the charge is always detonated at the cylinders centre of mass.
- the cylinders are perfect/ ideal (that is, no welds, defects or holes).

These constraints simplified the analyses, which allowed the authors [18] to develop equations for water or air filled cylinders. More than 100 experiments were performed for the investigation. Figure 2.11 depicts a heavily simplified layout of the test rig used in the experiments.

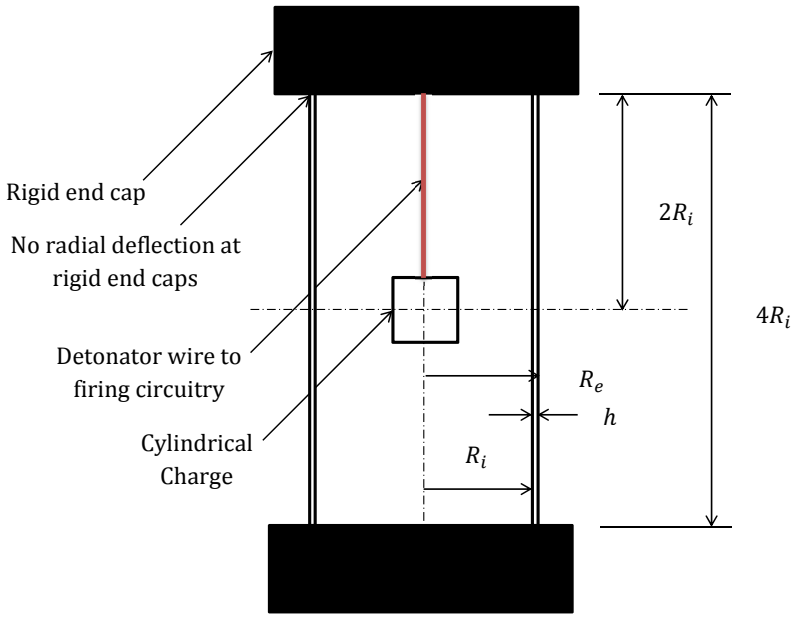

Figure 2.11: Schematic Showing the Test Rig Used by Proctor and Wise [18]

The authors [18] proposed Equation 2.26, which describes the relationship between the maximum charge mass (TNT or pentolite) that a cylinder can withstand before rupture, the cylinder material properties and the dimensions.

$$\left(\bar{W}_R\right)_{max} = \left[\frac{0.1563\epsilon_u\rho^{0.85}\left(3.41+0.117\frac{R_i}{h_o}\right)\left(R_e^2-R_i^2\right)^{1.85}}{10^5\left[\left(1.47+0.0373\frac{R_i}{h_o}\right)R_i\right]^{0.15}\left(2\sigma_y+\sigma_u+\sigma_u\epsilon_u\right)^{-1}}\right]^{0.811} \tag{2.26}$$

Where ρ is the density, ϵ_u is the engineering strain of the material at UTS, R_e is the external radius of the cylinder, σ_u is the UTS of the material, R_i is the inner radius of the cylinder, and σ_y is the engineering yield strength of the material.

The radial strain was affected by the filler material (that is, water or air). The air filled cylinders had lower radial strains than the water filled cylinders, because water has a higher bulk modulus. This is depicted in Figure 2.12.

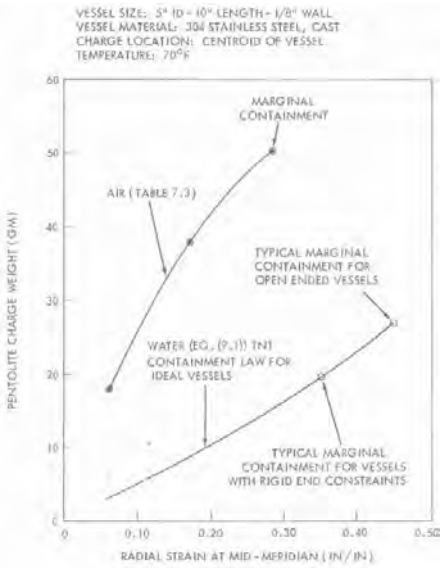

Figure 2.12: Comparison of the Radial Strains for Air and Water Filled Cylinders [18]

Air Filled Cylinder Response

Duffey and Mitchell [2] reported that the work done by Proctor and Wise [18] was comprehensive, yet could not be used to calculate the diametric deflection for a given charge mass, or predict the diametric deflection as a function of axial distance. Duffey and Mitchell [2] wanted to develop a theory that could predict the deflection of a cylinder, which was loaded by a centrally located bare spherical charge. Figure 2.13 depicts the problem.

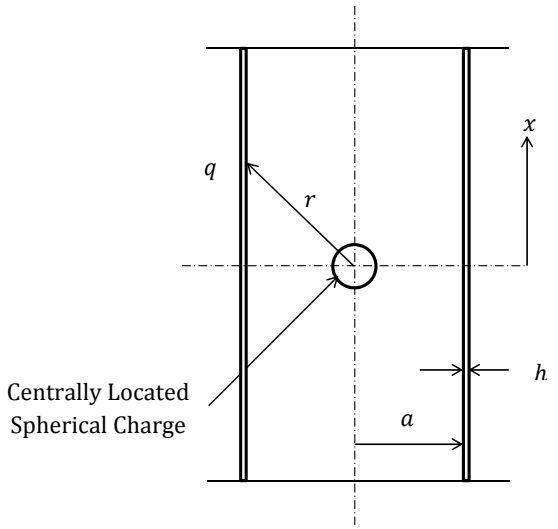

Figure 2.13: Geometry of the Problem Investigated by Duffey and Mitchell [2]

The problem was designed so that a cylinder with an internal radius a could be loaded by a charge of mass W, and that the deflection of an arbitrary point q, which was some axial distance x from the charge centre, could be calculated. The authors [2] made the following assumptions about the charge load, and the cylinder's wall response:

- the initial shockwave is a purely impulsive load, and the load application time can be ignored. Hence, the kinetic energy from the impulse is converted to strain energy.
- the wall has an non-zero velocity at $t = 0$.
- based on the findings of Proctor and Wise [18], the effects of gas pressure can be ignored.
- the cylinders wall thickness is small relative to the other dimensions. Hence, the wave propagation through the wall, and the axial bending moment can be ignored.
- the cylinder has no end caps, and the length is large compared to diameter. Hence, the time it takes for the structure to respond is smaller than the time required for the pressure wave to reach the end. Hence, the resultant axial strain can be ignored.

While developing the theory, the authors [2] assumed that the material is rate sensitive, and that strain hardening is linear. Equation 2.27 was developed.

$$\epsilon\left(x\right) = \sqrt{\frac{1}{\lambda^2} + \frac{I_{eff}^2\left(x\right)}{\rho h^2 \lambda \sigma_y \left[1 + \left(\frac{I_{eff}(x)}{\rho h a D}\right)^{\frac{1}{P}}\right]}} - \frac{1}{\lambda} \qquad \text{valid for } \lambda > 0 \tag{2.27}$$

Where λ is the linear strain hardening parameter, ρ is the density of the material, a is the wall thickness, σ_y is the yield stress, D and p are Cowper-Symonds constants specific to the material, and I_{eff} is the effective impulse per unit area. The linear strain hardening parameter is calculated using Equation 2.28.

$$\lambda = \frac{\left(\frac{UTS}{\sigma_y} - 1\right)}{e_{ult}} \tag{2.28}$$

Where e_{ult} is the engineering strain at the UTS. To exclude strain hardening (that is, $\lambda = 0$ and $\sigma_y = UTS$), the authors [2] developed Equation 2.29.

$$\epsilon\left(x\right) = \frac{I_{eff}^2\left(x\right)}{2\rho h^2 \sigma_y \left[1 + \left(\frac{I_{eff}(x)}{\rho h a D}\right)^{\frac{1}{P}}\right]} \tag{2.29}$$

The authors [2] presented another case, for materials that had no strain hardening or rate sensitivity (that is, $D \to \infty$). For this case, the circumferential strain is calculated using Equation 2.30.

$$\epsilon\left(x\right) = \frac{I_{eff}}{2\rho h^2 \sigma_y} \tag{2.30}$$

The authors [2] used Equation 2.31 to calculate the effective impulse.

$$I_{eff} = \left(I_{nr} - I_{so}\right) \frac{a}{\sqrt{a^2 + x^2}} + I_{so} \tag{2.31}$$

Where I_{nr} is the resultant of the normal incident and reflected impulses, and I_{so} is the incident impulse. The authors [2] reported that the impulse quantities are time integrals, and are affected by the magnitude of the atmospheric pressure, P_0. Empirical equations for the impulse quantities in terms of the atmospheric pressure and the scaled distance Z were developed. The incident impulse is calculated using Equation 2.32.

$$\frac{I_{so}}{P_0^{\frac{2}{3}} W^{\frac{1}{3}}} = \frac{a_1}{P_0^{\frac{1}{3}} Z} + \frac{a_2}{\left(P_0^{\frac{1}{3}} Z\right)^2} \qquad \text{valid for } 2.38 \leq P_0 Z \leq 68 \tag{2.32}$$

Where a_1 and a_2 are experimentally determined coefficients, described by Equation 2.33.

$$a_1 = 0.06333 \frac{lbf/\left(in^2 s\right)}{ATM^{\frac{1}{3}} lbf^{\frac{2}{3}}/\left(ft\right)} \qquad a_2 = -0.06289 \frac{lbf/\left(in^2 s\right)}{lbf/\left(ft^2\right)} \tag{2.33}$$

The resultant of the normal incident and reflected impulses is calculated using Equation 2.34.

$$\frac{I_{nr}}{P_0^{\frac{2}{3}} W^{\frac{1}{3}}} = \frac{b_1}{P_0^{\frac{1}{3}} Z} + \frac{b_2}{\left(P_0^{\frac{1}{3}} Z\right)^2} + \frac{b_3}{\left(P_0^{\frac{1}{3}} Z\right)^3} \qquad \text{valid for } 0.1096 \leq P_0 Z \leq 23.80 \tag{2.34}$$

Where b_1, b_2, and b_3 are experimentally determined coefficients, which are described by Equation 2.35.

$$b_1 = 0.1204 \frac{lbf.s/in^2}{ATM^{\frac{1}{3}} lbf^{\frac{2}{3}}/\left(ft\right)} \qquad b_2 = 0.1384 \frac{lbf.s/in^2}{lbf/\left(ft^2\right)} \qquad b_3 = 0.003708 \frac{lbf.s/in^2}{ATM^{-\frac{1}{3}} lbf^{\frac{4}{3}}/\left(ft^3\right)} \tag{2.35}$$

From Figure 2.13, and by cube root scaling, the scaled SOD is calculated using Equation 2.36.

$$Z = \frac{r}{W^{\frac{1}{3}}} = \frac{\sqrt{x^2 + a^2}}{W^{\frac{1}{3}}} \tag{2.36}$$

To validate the theory, Duffey and Mitchell [2] tested four annealed mild steel cylinders, with different charge masses of C4. In these tests, strain hardening was excluded, yet rate sensitivity was included. Table 2.3 presents the parameters used in the validation. Metric equivalent values were added for ease of reference.

Table 2.3: Parameters Used in Each Annealed Mild Steel Cylinder Test [2]

Physical Quantity	**Units**	**Test 1**	**Test 2**	**Test 3**	**Test 4**
a	in (mm)	5 (127)	3.874 (98.40)	3.874 (98.40)	3.874 (98.40)
W	lb (g)	0.772 (350)	0.1103 (50)	0.1323 (60)	0.1763 (80)
h	in (mm)	0.25 (6.35)	0.08 (2.03)	0.08 (2.03)	0.08 (2.03)
$P_0 = 0.836\ atm$, $\rho = 7.29e-4\ s^2 lbf/\left(in^4\right)$, $\sigma_y = 3e4\ lb/\left(in^2\right)$				$p = 5.0$, $D = 40.4$, $\lambda = 0$	
$P_0 = 84.71\ MPa$, $\rho = 7790.75\ kg/m^3$, $\sigma_y = 206.84\ MPa$				—	

Figure 2.14 presents the correlation of the theory to the experimental data set, for a mild steel cylinder that was loaded by $50g$ of C4 (that is, Test 2 in Table 2.3).

The theory seems to under predict the results of the one half of the cylinder by a constant value. It is clear that the circumferential strain with respect to axial distance was not symmetric. The possible causes of the asymmetry are that either the detonator was not inserted into the charge at its centre of mass, or the charge was not in the cylinders centre of mass at the time of detonation. Duffey and Mitchell [2] did not discuss the asymmetry of the circumferential strain, nor mention the possible underlying causes. Figure 2.14 demonstrates that the theory has some correlation with the experimental data. It is within reason to conclude that if the asymmetry was removed, the mild steel theory would credibly predict the circumferential strain with respect to axial distance.

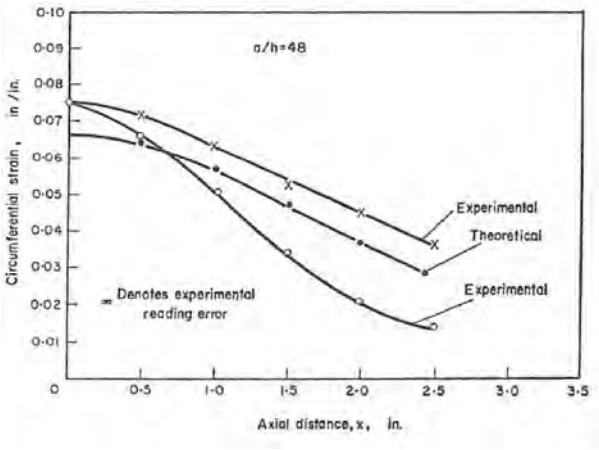

Figure 2.14: Experimental - Theoretical Correlation of a Mild Steel Cylinder Loaded by $50g$ C4 [2]

To further validate the theory, the authors [2] used the properties of 304 stainless steel, to plot a theoretical circumferential strain with respect to axial distance. The curve was compared to the experimental data from Proctor and Wise [18]. Strain hardening was included, yet rate sensitivity was excluded, to develop Equation 2.37.

$$\epsilon(x) = \sqrt{\frac{1}{\lambda^2} + \frac{I_{eff}^2(x)}{\rho h^2 \lambda \sigma_y}} - \frac{1}{\lambda} \qquad \text{valid for } \lambda > 0 \tag{2.37}$$

Table 2.4 presents the parameters used in the validation. Metric equivalent values are added for ease of reference.

Table 2.4: Parameters Used in the 304 Stainless Steel Cylinder Validations [2]

P_0	a	W	ρ	h	σ_y	p	D	λ
$ATM\ (KPa)$	in	$lb\,(g)$	$s^2lbf/\,(in^4)$	in	$lb/\,(in^2)$	–	–	–
1	2.5	0.1101	7.29e-4	0.125	3e4	5.0	∞	1.95
KPa	mm	g	kg/m^3	mm	MPa	—		
101.325	63.5	50	7 790.75	3.175	206.84	—		

Figure 2.15 depicts the correlation of the theory to the experimental data set from Proctor and Wise [18]. Upon comparing the results of Figure 2.15 to that of Figure 2.14, it can be seen that the theory has better correlation with the experimental data of the 304 stainless steel.

Lastly, the authors [2] reported that the theory is appropriate for explosive containment design, yet is limited to air filled cylinders, loaded by fully vented bare spherical high explosive charges.

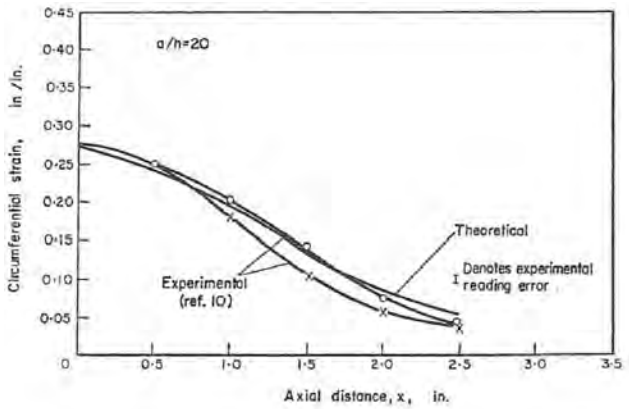

Figure 2.15: Experiment - Theory Correlation of a 304 Stainless Steel Cylinder Loaded by $50g$ C4 [2]

Influence of Cylindrical End Caps

Benham and Duffey [19] studied the effect of end caps on the structural response of cylinders subjected to internal air blast loading. Figure 2.16 depicts the geometry of the new problem.

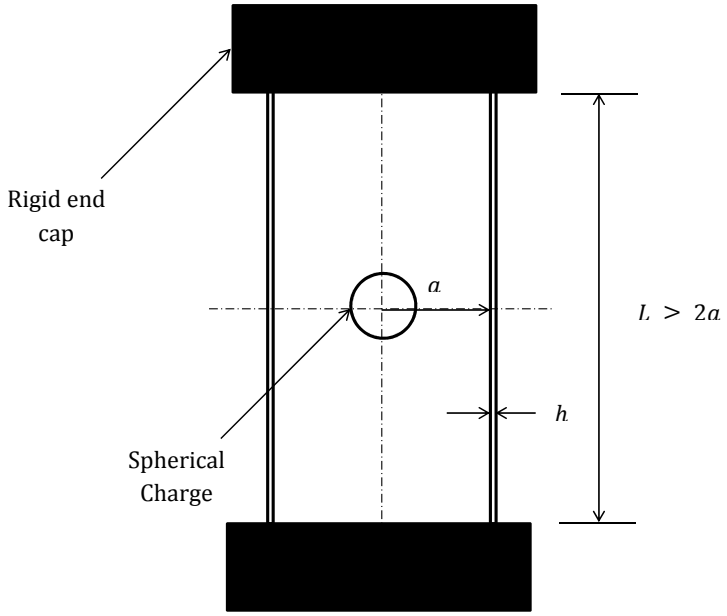

Figure 2.16: Schematic Showing Cylinder Geometry Investigated by Benham and Duffey [19]

Benham and Duffey [19] developed a theory which predicted the maximum radial deflection, while accounting for end cap effects. Unlike Duffey and Mitchell [2], the authors [19] were not interested in the variation of the circumferential strain with respect to axial distance. The problem was designed so that

a cylinder with thickness h, internal radius a, and length L, which was closed at both ends by end caps, would be loaded by a centrally located spherical charge of mass W. It was assumed that the end caps were rigid. Also, it was assumed that the pressure history was purely impulsive (that is, $I_0\delta(t)$), followed by exponential decay (that is, $U(t-T)P_0e^{-\alpha(t-T)}$), as depicted by Figure 2.17.

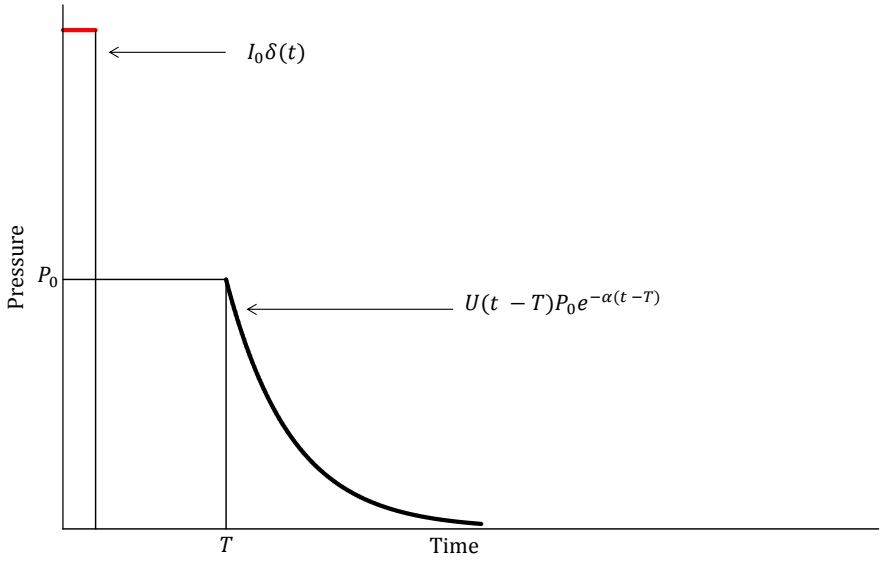

Figure 2.17: Assumed Pressure History According to Benham and Duffey [19]

The initial pressure was idealised as a purely impulsive load I_0 against the cylinder wall. After which, the initial pressure wave travelled towards the end caps. When the initial pressure wave encountered the end caps (that is, $t = T$), amplification due to reflection occurred, which caused the pressure to converge to equilibrium at P_0. Thereafter, the pressure decayed exponentially. The assumed pressure history, as per Figure 2.17, is calculated using Equation 2.38.

$$p(t) = I_0\delta(t) + U(t-T)P_0e^{-\alpha(t-T)} \tag{2.38}$$

Where α is a pressure decay constant, T is the time delay between the application of the purely impulsive load and the equilibrium pressure, and $U(t-T)$ is the Heaviside unit step function. The equilibrium pressure is calculated using Equation 2.39.

$$P_0 = \frac{CW}{V} \tag{2.39}$$

Where V is the internal volume of the cylinder, W is the explosive weight, and C is a constant specific to the kind of explosive (for example, primary high, secondary high, etcetera) used. To calculate I_0, the authors used Equation 2.34, as per the Duffey and Mitchell [2] paper. The scaled distance Z, which was mentioned in Equation 2.7 – 2.10, was calculated using Equation 2.40.

$$Z = \frac{a}{W^{\frac{1}{3}}} \tag{2.40}$$

Following Duffey and Mitchell [2], the axial stresses and bending moments were excluded from, and linear strain hardening was included in the analysis. Equation 2.41 was developed.

$$\frac{d^2w}{dt^2} + \frac{\lambda\sigma_y^D}{\rho a^2}w + \frac{\sigma_y^D}{\rho a} = I_0\delta\left(t\right) + U\left(t-T\right)P_0e^{-\alpha(t-T)} \tag{2.41}$$

Equation 2.42 is the solution to Equation 2.41, for a constant strain rate and dynamic yield strength.

$$w\left(t\right) = \frac{\mu}{\sqrt{\beta}}sin\left(\sqrt{\beta}t\right) - \frac{\gamma}{\beta}\left[1 - cos\left(\sqrt{\beta}t\right)\right] + \zeta U\left(t-T\right)\left[\frac{e^{-\alpha(t-T)}}{\alpha^2+\beta} + \frac{sin\left(\sqrt{\beta}\left(t-T\right)-\xi\right)}{\sqrt{\beta\left(\alpha^2+\beta\right)}}\right] \tag{2.42}$$

Where the constants are calculated using Equation 2.43.

$$\beta = \frac{\lambda\sigma_y^D}{\rho a^2} \qquad \gamma = \frac{\sigma_y^D}{\rho a} \qquad \mu = \frac{I_0}{\rho h} \qquad \zeta = \frac{P_0}{\rho h} \qquad \xi = tan^{-1}\left(\frac{\sqrt{\beta}}{\alpha}\right) \tag{2.43}$$

Similar to the Duffey and Mitchell [2] paper, the initial strain rate with respect to the initial impulse is calculated using Equation 2.44.

$$\dot{\epsilon_1} = \frac{I_0}{\rho h a} \tag{2.44}$$

To determine the maximum radial deflection, the time t_{max} at which the wall reached this maximum (that is, when $\frac{dw(t)}{dt} = 0$), was found. This t_{max} magnitude was substituted back into Equation 2.42, to get the maximum displacement. This displacement is reduced when the end caps are removed (that is, $\zeta = 0$ for open cylinders). Hence, the lower boundary of the maximum displacement for a given charge mass, was found. For constant σ_y^D and $\zeta = 0$

$$t_{max} = \frac{1}{\sqrt{\beta}}tan^{-1}\left(\frac{\mu\sqrt{\beta}}{\gamma}\right) \tag{2.45}$$

When the deflection with respect to time follows a non-linear trend (that is, variable strain rate and σ_y^D), Equation 2.41 cannot be solved analytically. Also, because the pressure decay from the magnitude of equilibrium is slow (that is, small α value), the radial deflection will increase. Runge-Kutta methods were used to find numerical solutions. The upper boundary of the maximum displacement assumed that the equilibrium pressure and the initial impulse were applied simultaneously (that is, $T = 0$), and that the cylinder was closed (that is, $\zeta > 0$ when gas pressure is accumulated).

To validate the theory, the authors [19] tested nine steel cylinders that were clamped between thick end caps. Every cylinder had a 10.5 *in.* (266.7 *mm*) inner diameter, and a 0.25 *in.* (6.35 *mm*) wall thickness. Prior to testing, the cylinders were annealed. Centrally located bare spherical C4 charges were used. Figure 2.18 depicts a simplified layout of the test rig that was used by Benham and Duffey [19].

Figure 2.19 shows a comparison between the experimental data and the theoretical solutions. Curves 1 and 3 represents the lower and upper boundary maximum displacements with respect to charge mass, respectively. Curve 2 represents the numerical solution. Like Curve 1, curve 2 assumes that the cylinder is open (that is, $P_0 = 0$), yet the dynamc yield strength is not constant. Curve 4 represents the numerical solution, which, like Solution 3, assumes that the cylinder is closed, with the impulsive load applied some time before gas pressure is accumulated.

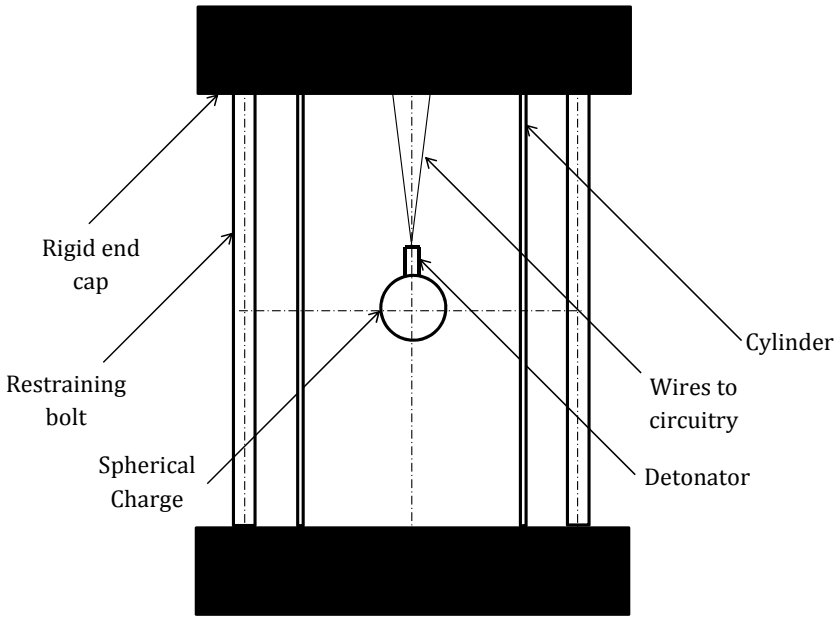

Figure 2.18: Schematic Showing Cross-Section of the Test Rig Used by Benham and Duffey [19]

In the lower domain (that is, $0 \leq W < 0.3$), there is very little difference between the curves. Hence, it can be stated that test points 1 and 2 correlates very well with the theory.

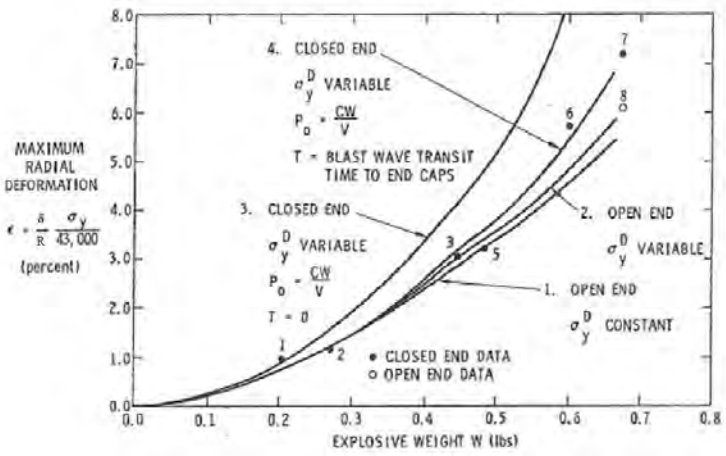

Figure 2.19: Comparison of the Theoretical Solutions to the Experimental Data [19]

In the upper domain (that is, $0.4 \leq W$), the deviation of curve 3 from the other curves is significant, because the time delay has a greater effect on the maximum radial deflection. In the region where test points 3 and 5 lie, the difference between curves 1, 2, and 4 is not significant. Hence, it can be stated that despite the slight deviation, test points 3 and 5 had reasonable correlation with curve 4. Test points 6 and 7 had better correlation with curve 4, illustrating that the time delay significantly influenced the maximum radial deflection.

Test 8 was conducted with the same charge mass as test 7, yet excluding the end caps. Figure 2.19 shows that test 8 correlates with curve 2, as might be expected. It should be noted that test 8 was the only test conducted to separate the effect of the end caps.

To separate the effect of the gas pressure from the initial impulse, the authors defined a modified pressure ratio $\bar{\eta}$, which is calculated using Equation 2.46.

$$\bar{\eta} = P_0 \left(\frac{a}{h\,UTS}\right)\left(\frac{t_{max} - T}{t_{max}}\right) \qquad \text{where } \bar{\eta} = 0 \text{ for } T > t_{max} \tag{2.46}$$

The condition on Equation 2.46 implies that if the cylinder wall reaches its maximum radial deflection before the time delay (that is, a purely impulsive load), the gas pressure accumulation can be ignored. Figure 2.20 presents the effect of separating the gas pressure from the impulsive load.

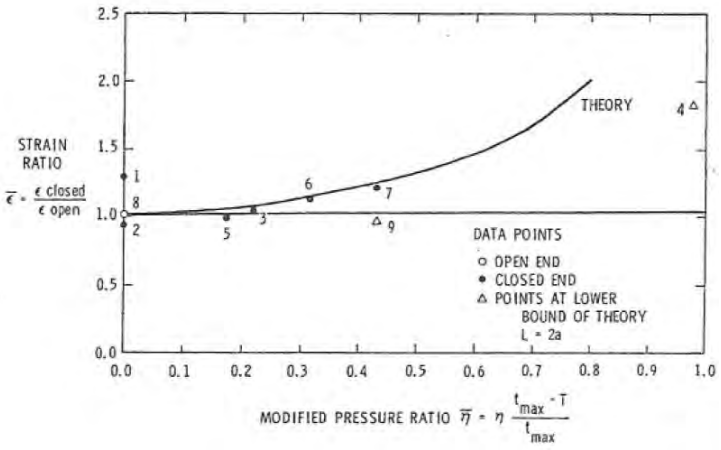

Figure 2.20: Graph of Strain Ratio *vs* $\bar{\eta}$, Showing Experimental Correlation With the Theory, Proposed in Ref. [19]

The strain ratio is 1 because a purely impulsive load (that is, $T = 0$) does not see the end caps. Any deviation of the strain ratio from 1 implies that the accumulated gas pressure is important. In the lower domain (that is, $0 \leq \bar{\eta} \leq 0.3$) the difference between the theory, the experimental data, and the unity line is not significant. In the middle domain (that is, $0.3 \leq \bar{\eta} \leq 0.45$), the effect of gas pressure is evident. In the upper domain (that is, $0.45 < \bar{\eta}$), no data points are shown, yet, test point 4 seems to indicate that the theory may overpredict the strain.

The work of Benham and Duffey [19] is mentioned herein because Ozinsky [22, 23] scaled the work of the authors [19] (refer to Section 3.1.2).

2.5.2 Recent Studies

Open-Ended Cylinder Subjected to Internal Blast Loading

The primary objectives of Clayton *et al.* [20] and Rushton *et al.* [21] were to determine the maximum circumferential strain and the minimum charge mass required to induce wall failure. In both investigations cylindrical PE4 charges, which were detonated at both ends, were used. The detonation at both ends ensured that the blast loading was symmetric, and that most of the impulse was transferred to the wall. The cylinders were $800mm$ long, had a $9.5mm$ wall thickness, and a $324mm$ outer diameter. Figure 2.21 depicts the arrangement used by the authors [20, 21], which is similar to that used by Duffey and Mitchell [2]. Cardboard collars were used to mount the charges in the cylinders. It was assumed that the collars vapourised after detonation [21].

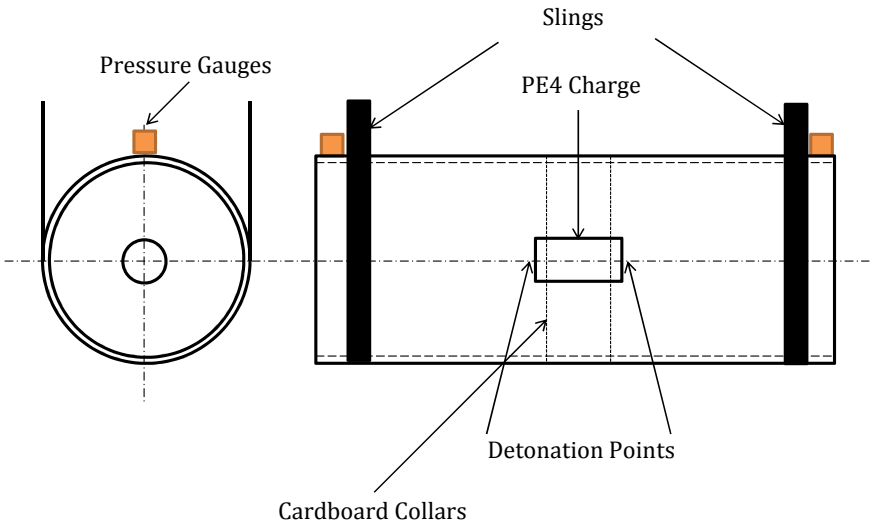

Figure 2.21: Layout of the Test Rig Used by Schleyer and Rushton [20, 21]

Rushton *et al.* [21] presented data sets for the 0.6 and 0.8 kg charges. Both papers [20, 21] presented numerical simulations of the experiments in AUTODYN. The cylinders were modelled axisymmetrically in the Lagrangian configuration, and the air/ explosive mixture was modelled in the Eulerian configuration. Clayton *et al.* [20] presented simulated data sets for charge masses, yet did not present experimental validations. Figure 2.22 presents simulated data from Clayton *et al.* [20], which predicts the effect of the half reciprocal of the aspect ratio (that is, $\frac{1}{2R_{ld}} = \frac{r}{L}$) on the circumferential strain, for a 1 kg charge.

These simulated results predict that the circumferential strain is strongly influenced by the aspect ratio. These results also predict that a cylindrical charge with a unified aspect ratio will cause a greater amount of circumferential strain than its mass equivalent spherical charge. This finding was not experimentally validated.

Rushton and Schleyer [21] used cylindrical charges with unified aspect ratios. Charge masses of 0.5 to 1.5 kg were used to load the cylinders. The consequences of detonating the charges at both ends was that

the shock waves propagated longitudinally and collided. The collision caused the superimposed wave to propagate radially, to deform the walls. Subsequently, localised thermal softening, quasi-static pressure accumulation, and shock pressure created a bulge. The authors [21] observed wall thinning at the bulge, and reported that at least 1.225 kg of PE4 was required to initiate tensile fracture and adiabatic shear. In addition to tensile fracture and adiabatic shear, the charges with masses larger than 1.225 kg caused tearing, as shown in Figure 2.23.

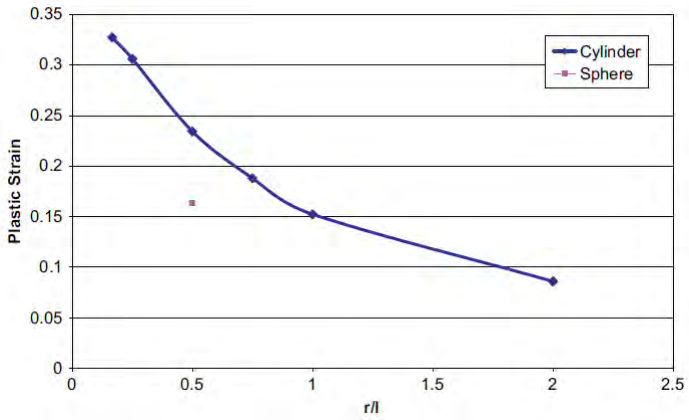

Figure 2.22: Effect of Changing Charge Dimensions on Circumferential Strain (1 kg Charge) [20]

Figure 2.23: Fractured Cylinders After Loading by 1.225, 1.3, and 1.5 kg PE4 [21]

The cylinders that were loaded with charge masses of 1.225 and 1.3 kg did not show equidistant fracture points along the circumference as evidently as the cylinder that was loaded by a 1.5 kg charge. Localised wall thinning midway between the fracture points was reported by the authors [21].

Response of Cylinders to Partially Confined Internal Explosions

Ozinsky *et al.* [22, 23] conducted an experimental and numerical investigation into the structural response of right circular cylinders to partially confined blast loads. The work of Benham and Duffey [19] was scaled to derive the experimental geometry. The cylinders had a $330mm$ length ($30mm$ of which was clamped), a $150mm$ inner diameter, and a $2mm$ thickness. Spherical charges of different masses were positioned at $0.5L$ and $0.75L$ from the closed end, where L is the non-clamped length of the cylinder. Full polystyrene annuli were used to mount the charges at the cylinders radial centres, similar to Schleyer and Rushton [21]. Figure 2.24 depicts the charge position cases, where the clamped region is the closed end, and the other end is open to the atmosphere.

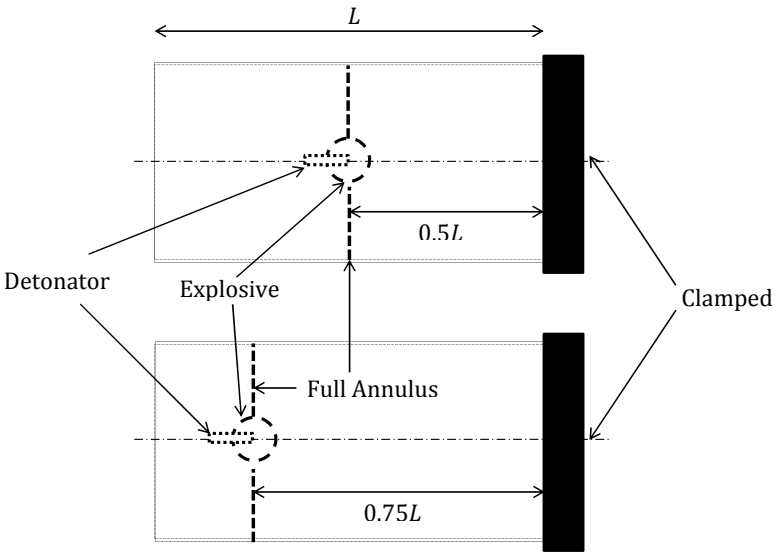

Figure 2.24: Spherical Charge Positions used by Ozinsky *et al.* [22, 23]

The rate at which radial deflection increased with respect to mass was affected by the charge position. Figure 2.25(a) depicts the experimental and the numerical radial deflections with respect to charge mass, for a $0.5L$ charge position.

The numerical and experimental deflections are linearly proportional to the charge mass for the 0.5 L position. Also, it is clear that the deviation of the numerical deflections from the experimental deflections is not significant, proving that the numerical model has credibility in predicting the radial deflection.

The experimental and numerical data do not follow the same trend at 0.75 L [22, 23]. For detonations up to 40 g, the deviation of the numerical data from the experimental data is not significant. However above 40 g, the numerical model is not accurate, underpredicting the radial deflections. Ozinsky *et al.* [22, 23] suggested that afterburning of the detonation products [1, 17, 36] could have caused the elevated deflections at the detonation centre.

The partial confinement and the position of the spherical charges had an effect on bulge development at the closed end, particularly at $0.75L$ for large charge masses (above $45g$).

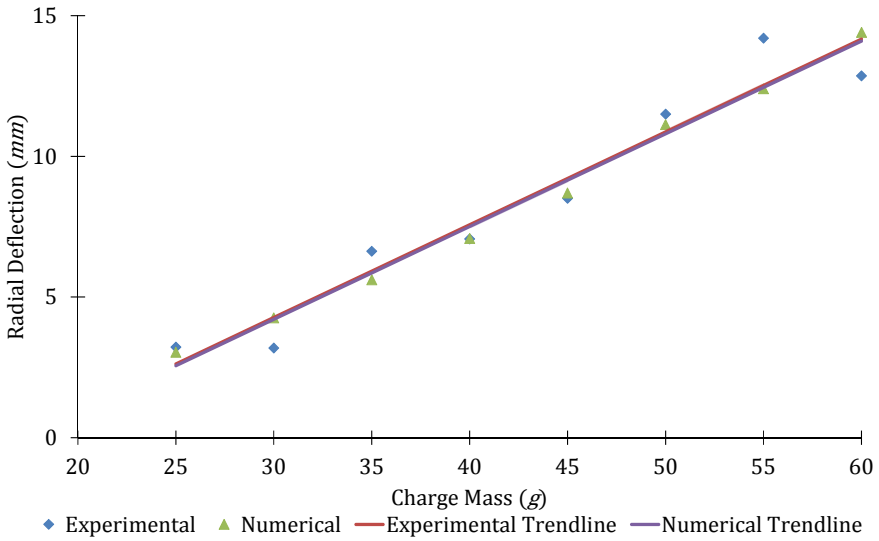

(a) 0.5 L Charge Position

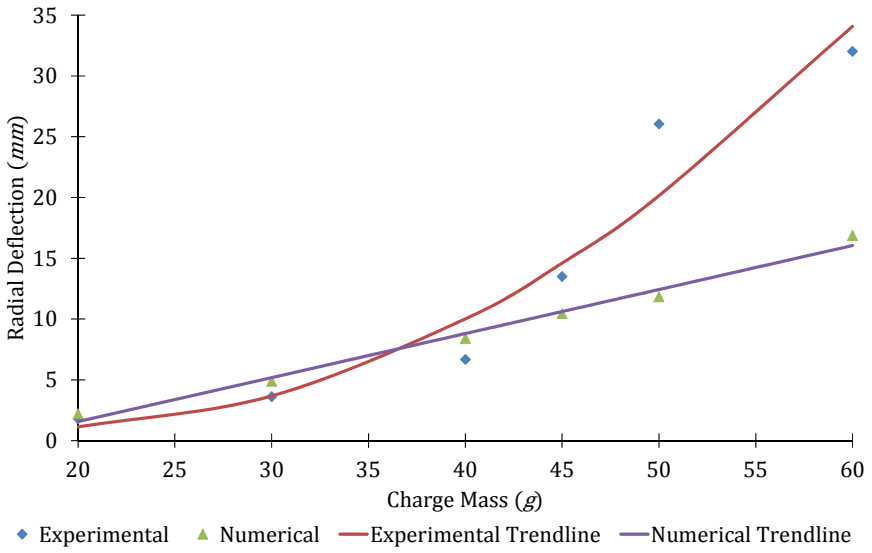

(b) 0.75 L Charge Position

Figure 2.25: Graph of Radial Deflection *vs* Charge Mass, From Ozinsky *et al.* [22, 23]

Ozinsky *et al.* [22, 23] used a ballistic pendulum to determine the impulse transfer to the closed end. Figure 2.26 depicts the experimental and numerical correlation of the impulse transfer values, for both axial locations (that is, $0.5L$, and $0.75L$). Impulse transfer is dependent on the charge mass, yet independent of the charge position, and the numerical model appears to correlate well when predicting the impulse transfer.

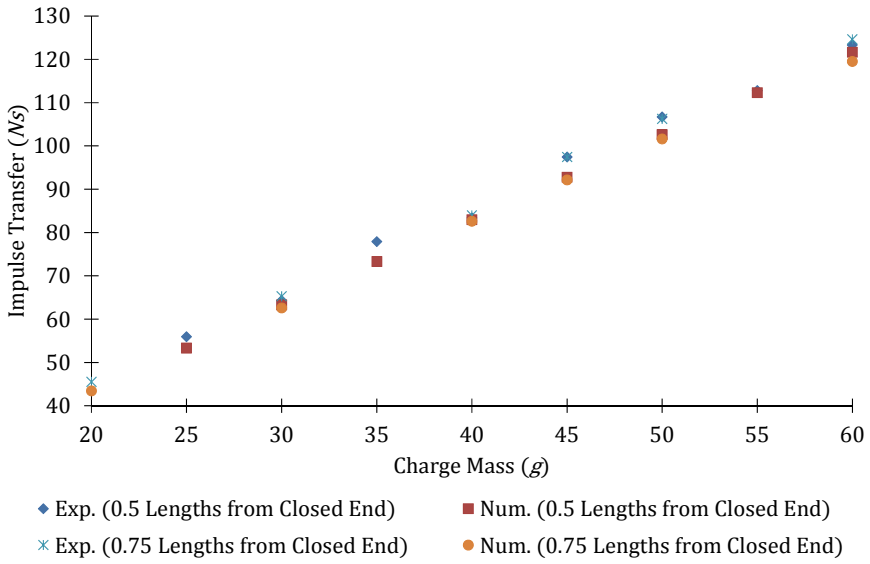

Figure 2.26: Experimental-Numerical Correlation of the Impulse Transfer Values [22, 23]

3

Blast Experimental Methodology

This Chapter presents the experimental methods used to test the seamless 304 stainless steel cylinders.

3.1 Test Rig

3.1.1 Explosive Material

Detonators

- Instantaneous electrical detonators were used to initiate the explosion.
- The detonators were placed in rear of the cylindrical charges and detonated a depth of 5 mm.
- The detonators were centrally located in the spherical charges to ensure that the blast wave propagated spherically.

3.1.2 Ballistic Pendulum

Figure 3.1 shows a schematic of the test rig which was used for all blast tests. The cylinder dimensions were determined by Ozinsky *et al.* [22] after scaling the work of Benham and Duffey [19]. The ballistic pendulum was used to infer the axial impulse, where the experimental and simulated values were compared, to ensure that the simulated load definition was correct.

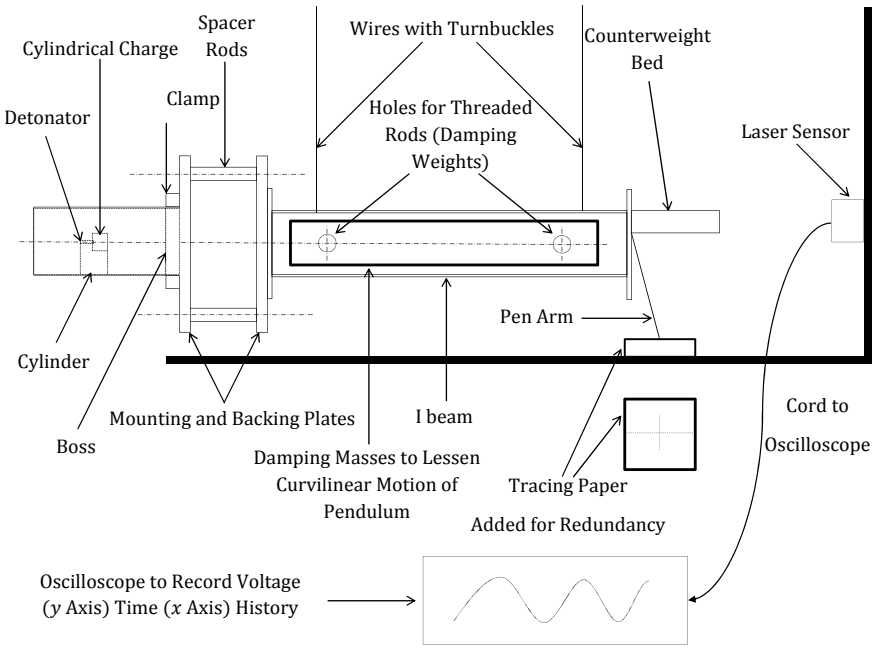

Figure 3.1: Schematic of Test Rig

A 400 mm x 400 mm backing plate was mounted to an I-beam, and a 400 mm x 400 mm mounting plate was mounted to the backing plate with spacers. A boss, with a 150 mm diameter, was used to attach the cylinders to the mounting plate, and a clamp, with a 154 mm inner diameter was used to keep the cylinder in place during testing. Four wires suspended the assembly to ensure that the pendulum followed a curvilinear motion. A wall mounted laser sensor, which was attached to an oscilloscope, was used to record the voltage history, to calculate the impulse. A pen arm was added to the pendulum

for redundancy, where the pen movement was also used to infer the impulse (refer to Appendix A for details).

To ensure that the sum of the forces and the moments on the ballistic pendulum were equal to zero before testing, the wires were set to be at the same length. Counterweights were also placed on the counterweight bed to balance the pendulum, and a spirit level was used to ensure that the weights were distributed evenly.

3.1.3 Cylinders

Similar to Ozinsky *et al.* [22], three $6m$ long seamless (extruded, not seam welded) 304 stainless steel DIN metric hygiene tubes (150 inner diameter, and 154 outer diameter) were purchased. These tubes were cut into 330 mm long cylinders, 30 mm of which was clamped. Figure 3.2 depicts the cylinders in the clamped configuration. The seamless cylinders allowed for the experiments to be simulated axisymmetrically, which reduced computation time.

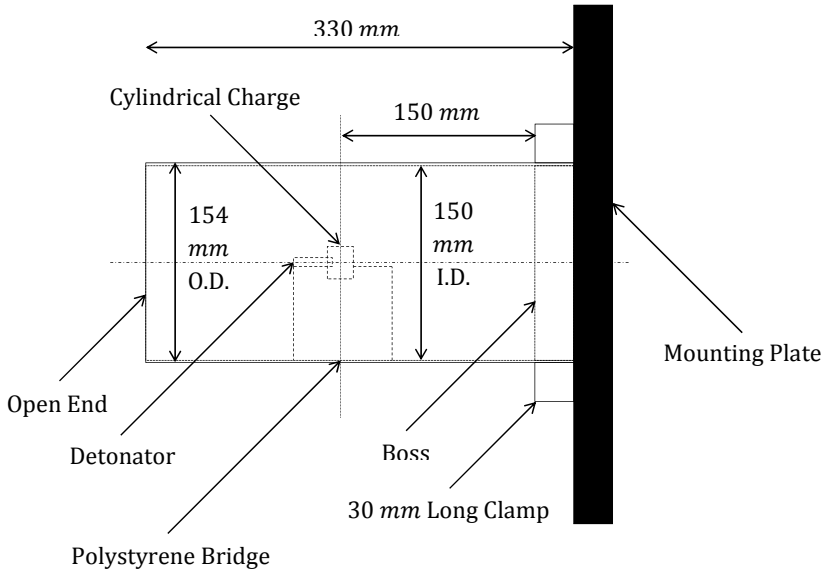

Figure 3.2: Schematic of Cylinder, Boss, Clamp, and Mounting Plate

A lattice was designed to aid the visualisation of the deformation around each cylinder. The design was modelled in SOLIDWORKS and laser cut into self-adhesive book wrap.

The cylinders were cleaned with thinners to remove any residue that would have prevented adherence of the book wrap. Thereafter, the book wrap was placed around each cylinder and spray painted. After spray painting, the book wrap was removed. The sixteen dots around the circumference were used to measure eight diametric deflections [22, 23], where ten sets of these dots along the length were used to plot diametric deflection profiles. Figure 3.3 depicts a cylinder with a lattice on it.

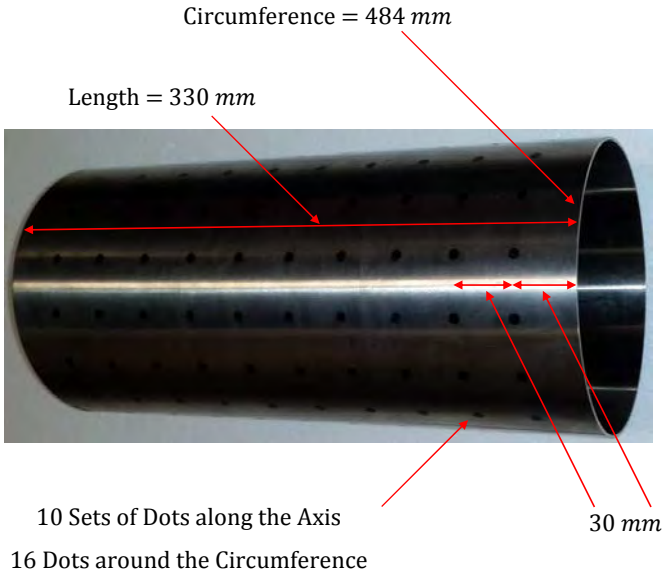

Figure 3.3: Photo Showing Marker Layout on Specimens

3.1.4 Polystyrene Bridge

Past members at the Blast Impact and Survivability Research Unit (BISRU) research group used polystyrene to mount explosives to test rigs. It was assumed that the polystyrene had little to no effect on the blast wave propagation or the transfer of energy. To minimise the influence of the polystyrene, the annulus used by Ozinsky *et al.* [22, 23] was replaced with a bridge arrangement shown in Figure 3.4. The polystyrene bridge was designed to:

- be stable while supporting the charge,
- have minimal influence on the blast wave propagation after detonation,
- have enough resting space for the detonator to rest after being placed in the charge, to ensure that the detonators longitudinal axis was collinear with that of the charge,
- and be adaptable to support spherical charges.

Table 3.1 presents the dimensions of the polystyrene bridges which were used for each charge diameter of interest, where the polystyrene thickness, t, was $14mm$.

Table 3.1: Polystyrene Bridge Dimensions for the Charge Diameters Used Herein

Physical Quantity	**Symbol**	$d = 25mm$	$di = 30mm$	$di = 35mm$	$d = 40mm$
Slot Length	l	$25R_{ld}$	$30R_{ld}$	$35R_{ld}$	$40R_{ld}$
Overall Length	L_o	$25R_{ld} + 2t$	$30R_{ld} + 2t$	$35R_{ld} + 2t$	$40R_{ld} + 2t$
Slot Width	w	20	25	30	35
Overall Width	W_o	48	53	58	63
Height (Excl. Radius)	h_s	50	48	46	44
Detonator Rest Height	h_r	4	5	6	6

Figure 3.4 depicts the design of the polystyrene bridge. The bridge has an overall length, width and height of L_o, W_o, and H_o, respectively.

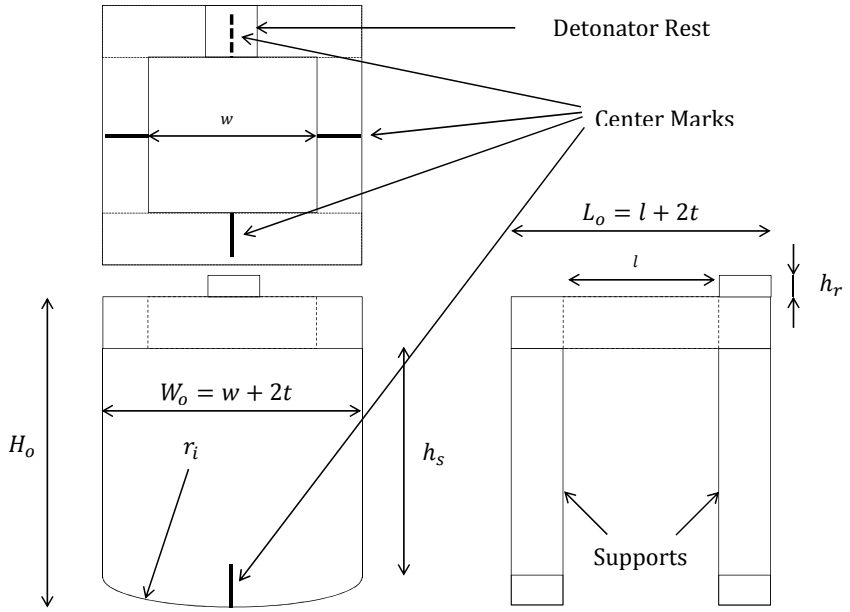

Figure 3.4: Schematic of Bridge Design (Dimensions on Table 3.1)

A detonator rest of height h_r ensured that the detonator was concentric to the charge and the cylinder. The rest height was constant for each charge diameter. The supports had a radius of $r_i = 75mm$, which was the same as the internal radius of the cylinders, for stability.

3.2 Charge Matrix

Table 3.2 presents a matrix of the charges which were within the mass allowance (that is, 75 g) for the BISRU blast chamber, where charges heavier than 72 g were excluded.

The diameters of interest were 25, 30, 35, and 40 mm, because it was assumed that at these diameters the detonation velocity did not change significantly, and detonation failure would not occur [12]. The charge specification (that is, **Charge**) column uses the following notation: CHARGE MASS_CHARGE DIAMETER_ASPECT RATIO (charge radius for spherical charges).

The charge masses were calculated by combining Equation 2.19 and Equation 2.18. Equation 3.1 presents the final expression.

$$m_{cyl} = \rho \frac{\pi R_{ld} d^3}{4} \tag{3.1}$$

Table 3.2: Matrix of Charge Specifications for Each Test

Charge	m	d	**Charge**	m	d	**Charge**	m	d
m Markers: 20 (♣), 24 (✿), 27 (➲) 31 (❣), 34 (✜), 43 (✂), 48 (▼), 49 (✌), 54 (✖) g Charges								
d Markers: 25 (ȣ), 30 (✷—), 35 (△), and 40 (**T**) mm Diameter Charges								
10g_25d_0.5		ȣ	20g_30d_0.6	♣	✷—	54g_35d_1	✖	△
12g_25d_0.6		ȣ	24g_30d_0.7	✿	✷—	59g_35d_1.1		△
14g_25d_0.7		ȣ	27g_30d_0.8	➲	✷—	65g_35d_1.2		△
16g_25d_0.8		ȣ	31g_30d_0.9	❣	✷—	40g_40d_0.5		**T**
18g_25d_0.9		ȣ	34g_30d_1	✜	✷—	48g_40d_0.6	▼	**T**
20g_25d_1	♣	ȣ	48g_30d_1.4	▼	✷—	56g_40d_0.7		**T**
24g_25d_1.2	✿	ȣ	54g_30d_1.6	✖	✷—	64g_40d_0.8		**T**
31g_25d_1.6	❣	ȣ	27g_35d_0.5	➲	△	72g_40d_0.9		**T**
43g_25d_2.2	✂	ȣ	32g_35d_0.6		△	20g_14.39d_1	♣	Spherical
49g_25d_2.5	✌	ȣ	38g_35d_0.7		△	34g_17.18d_1	✜	Spherical
59g_25d_3		ȣ	43g_35d_0.8	✂	△	54g_20.04d_1	✖	Spherical
17g_30d_0.5		✷—	49g_35d_0.9	✌	△	34g_30d_1[a]	✜[a]	✷—[a]
[a] Cylindrical charge that was detonated at its centre for a preliminary investigation								

Blast loading of the seamless 304 stainless steel cylinders was performed with these charge masses. The aspect ratios were chosen to determine the effect of charge geometry on the structural response of right circular cylinders to internal air blasting. The charge matrix was also designed so that the charges could be grouped by:

- keeping the charge mass constant and varying the aspect ratio (that is, the m column),
- keeping the charge diameter constant and varying the aspect ratio (that is, the d column).

Spherical charge tests were included for comparison with cylindrical charges of the same mass and an aspect ratio of 1. The charge pairs were: 20g_25d_1 and 20g_14.39d_1, 34g_30d_1 and 34g_17.18d_1, and 54g_35d_1 and 54g_20.04d_1.

4

Experimental Results

This chapter presents the experimental results with a discussion.

4.1 Tabulated Data

Table 4.1 presents the results of the tests with the cylindrical charges, where the detonators were positioned at a depth of 5 mm. The "**Charge**" column presents the charge specifications, the "m **Group**" column sorts the charges by mass, the "d **Group**" column sorts the charges by diameter, the "**Impulse**" column presents the impulses transferred to the pendulum, the "**Max. Defl.**" column presents the maximum diametric deflections of each cylinder, and the "**Short.**" column presents the axial shortenings of the cylinders.

The impulses were calculated using the oscilloscope or pen method. If both methods were used for a test, the oscilloscope impulse was chosen for tabulation and plotting (refer to Appendix A for details and comparison).

Table 4.1: Experimental Data Table

Charge	m **Group**	d **Group**	**Impulse** (Ns)	**Max. Defl.** (mm)	**Short.** (mm)
m Markers: 20 (♣), 24 (✿), 27 (➲) 31 (❣), 34 (✜), 43 (✂), 48 (▼), 49 (✌), 54 (✖) g Charges					
d Markers: 25 (ϑ), 30 (✷—), 35 (△), and 40 (**T**) mm Diameter Charges					
10g_25d_0.5		ϑ	24.96	1.95	0.73
12g_25d_0.6		ϑ	28.90	2.30	0.63
14g_25d_0.7		ϑ	31.81	3.93	0.41
16g_25d_0.8		ϑ	36.79	6.11	0.68
18g_25d_0.9		ϑ	39.32	8.91	1.26
20g_25d_1	♣	ϑ	42.63	9.22	2.08
24g_25d_1.2	✿	ϑ	49.75	13.89	2.80
31g_25d_1.6	❣	ϑ	60.63	25.67	5.76
43g_25d_2.2	✂	ϑ	78.26	44.41	11.70
49g_25d_2.5	✌	ϑ	87.93	53.59	16.05
59g_25d_3		ϑ	77.89	Ruptured	Ruptured
17g_30d_0.5		✷—	38.11	5.42	1.05
20g_30d_0.6	♣	✷—	43.48	8.26	1.20
24g_30d_0.7	✿	✷—	51.38	8.48	2.18
27g_30d_0.8	➲	✷—	53.64	15.11	2.77
31g_30d_0.9	❣	✷—	61.77	20.65	4.73
34g_30d_1	✜	✷—	66.71	21.80	4.55
48g_30d_1.4	▼	✷—	89.74	43.66	12.92
54g_30d_1.6	✖	✷—	97.11	55.58	18.25
27g_35d_0.5	➲	△	54.70	10.34	1.84
32g_35d_0.6		△	63.74	17.05	3.49
38g_35d_0.7		△	73.44	25.66	6.20
43g_35d_0.8	✂	△	81.67	30.44	8.72
49g_35d_0.9	✌	△	93.36	38.48	11.87
54g_35d_1	✖	△	102.07	44.24	15.05
59g_35d_1.1		△	81.45	45.08	15.52
65g_35d_1.2		△	113.44	Ruptured	Ruptured
40g_40d_0.5		**T**	79.80	19.41	5.38
48g_40d_0.6	▼	**T**	91.71	26.38	8.55
56g_40d_0.7		**T**	108.36	35.91	13.14
64g_40d_0.8		**T**	118.78	45.33	18.79
72g_40d_0.9		**T**	119.28	Ruptured	Ruptured

4.2 Cylinder Profile

4.2.1 Pictures

Figure 4.1 shows photographs of the cylinders that were tested with 25 *mm* charges. Remember that the notation used to describe each cylinder is: CHARGE MASS_CHARGE DIAMETER_ASPECT RATIO. As the aspect ratio of the 25 *mm* charges (that is, charge mass) increased, the amount of deformation that was localised at the charge location, henceforth called the primary bulge, increased.

(a) 10g_25d_0.5 (155.15) (b) 12g_25d_0.6 (156.30) (c) 14g_25d_0.7 (157.93) (d) 16g_25d_0.8 (160.11)

(e) 18g_25d_0.9 (162.91) (f) 20g_25d_1 (163.22) (g) 24g_25d_1.2 (167.89) (h) 31g_25d_1.6 (179.67)

(i) 43g_25d_2.2 (198.41) (j) 49g_25d_2.5 (207.59)

Figure 4.1: Photographs of Cylinders Blast Loaded by 25 *mm* Cylindrical Charges (Diameters After Testing in Brackets)

Figure 4.2, 4.3, and 4.4 shows photographs of the cylinders that were tested with 30, 35, and 40 mm charges, respectively. In each case, as the aspect ratio increased, the size of the primary bulge increased. For the 30 mm charges with aspect ratios of 0.7 (Figure 4.2(a) – Figure 4.2(h)) and above, localised deformation at the clamped side of each cylinder, henceforth called the secondary bulge, formed.

(a) 17g_30d_0.5 (159.42) (b) 20g_30d_0.6 (162.26) (c) 24g_30d_0.7 (162.48) (d) 27g_30d_0.8 (169.11)

(e) 31g_30d_0.9 (174.65) (f) 34g_30d_1 (175.80) (g) 48g_30d_1.4 (197.66) (h) 54g_30d_1.6 (209.58)

Figure 4.2: Photographs of Cylinders Blast Loaded by 30 mm Cylindrical Charges (Diameters After Testing in Brackets)

Every cylinder that was blast loaded by the 35 and 40 *mm* charges had a secondary bulge, the size of which increased with aspect ratio, as shown in Figure 4.3 and 4.4, respectively.

(a) 27g_35d_0.5 (164.34) (b) 32g_35d_0.6 (171.05) (c) 38g_35d_0.7 (179.66) (d) 43g_35d_0.8 (184.44)

(e) 49g_35d_0.9 (192.48) (f) 54g_35d_1 (198.24) (g) 59g_35d_1.1 (209.08)

Figure 4.3: Photographs of Cylinders Blast Loaded by 35 *mm* Cylindrical Charges (Diameters After Testing in Brackets)

(a) 40g_40d_0.5 (173.41) (b) 48g_40d_0.6 (180.38) (c) 56g_40d_0.7 (189.91) (d) 64g_40d_0.8 (199.33)

Figure 4.4: Photographs of Cylinders Blast Loaded by 40 *mm* Cylindrical Charges (Diameters After Testing in Brackets)

4.2.2 Maximum Diametric Deflection

Figure 4.5 presents the maximum diametric deflections with respect to aspect ratio, where the diameter and mass were kept constant. The maximum diametric deflections of the original and repeat tests were added herein.

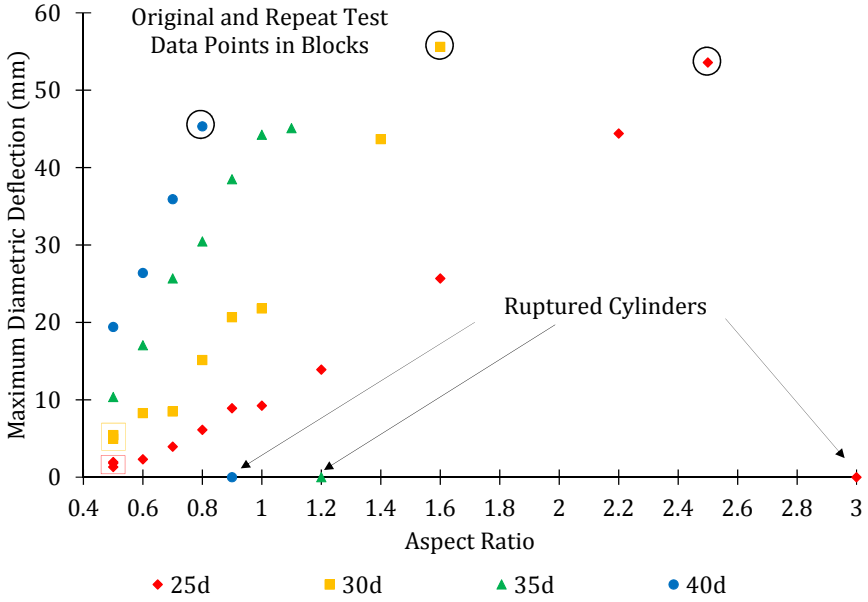

(a) Constant Diameter

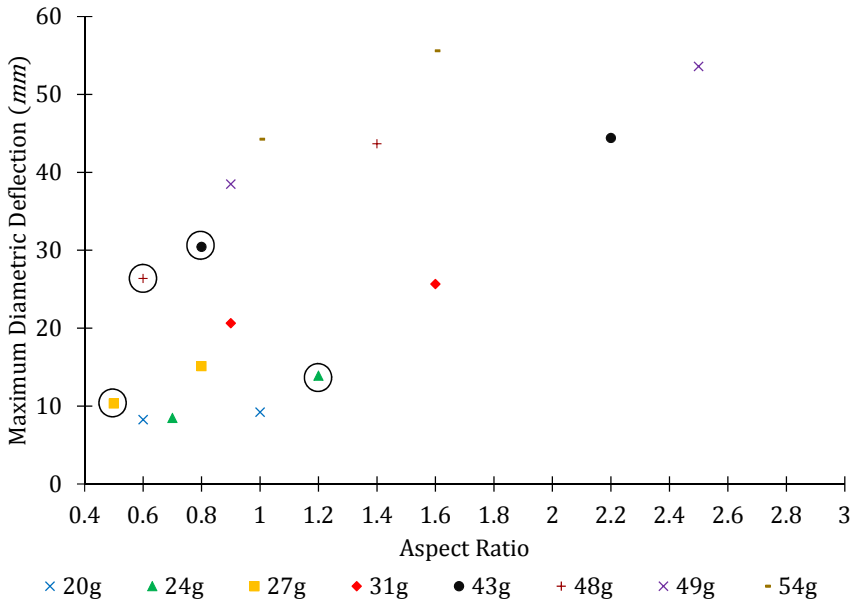

(b) Constant Mass

Figure 4.5: Graphs of Maximum Diametric Deflection *vs* Aspect Ratio

Constant Diameter

Figure 4.5(a) presents the maximum deflections with respect to aspect ratio, where the diameter was kept constant. When the diameter was kept constant, mass increased with the aspect ratio. Thus, it can be stated that Figure 4.5(a) also presents the effect of mass on the maximum diametric deflection. As expected, the change in maximum diametric deflection is directly proportional to the change in aspect ratio. The plotted data also shows that the slopes of the maximum diametric deflection curve increased as the diameter increased. The 64g_40d_0.8 charge caused the cylinder to have a significant amount of localised deformation at the primary and secondary bulges, yet the 59g_25d_3 charge, which is 5 g lighter caused its cylinder to fail. The 49g_25d_2.5 and 54g_30d_1.6 charges also produced higher deflections than 64g_40d_0.8 charge (see circled points on Figure 4.5(a)). In other words, lighter charges with smaller diameters (but larger aspect ratios) were observed to produce greater deformations and failures than charges with large diameters and low aspect ratios.

Constant Mass

Figure 4.5(b) presents the maximum diametric deflection with respect to aspect ratio, where the mass was kept constant. This plotted data shows that a long charge will diametrically deflect a cylinder more than its mass equivalent short charge. The plotted data also more clearly shows that a lighter charge that is long can cause higher deflections of its cylinder than a heavier charge (for example, compare the maximum deflections of 27g_35d_0.5 to 24g_25d_1.2, and 48g_40d_0.6 to 43g_35d_0.8 as circled on Figure 4.5(b)).

Side Effective Charge Mass and Maximum Diametric Deflection

According to Kennedy [13] the axial effective charge mass of a cylindrical charge (that is, the mass of the charge that contributed to the axial deflection of a plate) is a cone. This knowledge was used to calculate the side effective charge mass. Equation 4.1 was used to calculate the maximum height, H_{eff}^{max} of the axial effective charge mass [13] (refer to Figure 2.4).

$$H_{eff}^{max} = \frac{\sqrt{3}d}{2} \tag{4.1}$$

Equation 4.2 was used to calculate the actual height, H_{eff}, of the axial effective charge mass based on the charge specifications.

$$H_{eff} = H_{eff}^{max} \texttt{ if } H_{eff}^{max} \leq R_{ld}d\texttt{, else } R_{ld}d \tag{4.2}$$

Which means that the axial effective charge mass can be a full or a truncated cone. Equation 4.3 was used to calculate the smaller diameter, d_2 of the axial effective charge mass.

$$d_2 = \frac{H_{eff}^{max} - H_{eff}}{tan\left(\frac{\pi}{3}\right)} \tag{4.3}$$

Equation 4.4 was used to calculate the axial effective charge mass, m_{eff}^{axial}.

$$m_{eff}^{axial} = \rho\frac{\pi}{12}\left(d_1^2 + d_1d_2 + d_2^2\right)H_{eff} \tag{4.4}$$

Equation 4.5 was used to calculate the axial effective charge mass, where m is the total charge mass.

$$m_{eff}^{side} = m - m_{eff}^{axial} \tag{4.5}$$

Table 4.2 presents the axial and side effective charge masses of the cylindrical charges that were detonated, and their corresponding maximum diametric deflections and impulses. The side effective masses are directly proportional to the maximum diametric deflections, when mass is kept constant (which correlates with the plotted data on Figure 4.5(b)). The tabulated data also shows that the side effective charge mass of the 27g_35d_0.5 charge is lower than that of the 24g_25d_1.2 charge, and that the side effective charge mass of the 48g_40d_0.6 charge is lower than that of the 43g_35d_0.8 charge. This explains why the lighter charges caused higher deflections than the heavier charges.

Table 4.2: Proportionality of Effective Charge Mass to Maximum Deflection and Impulse

m (g)		R_{ld}	d (mm)	**Max. Defl.** (mm)	**Imp.** (Ns)	m_{eff}^{axial} (g)	m_{eff}^{side} (g)
m Markers: 20 (♣), 24 (✿), 27 (➲) 31 (❣), 34 (✜), 43 (✄), 48 (▼), 49 (✌), 54 (✖) g Charges							
10		0.5	25	1.95	24.96	5.243	4.757
12		0.6	25	2.30	28.90	5.507	6.493
14		0.7	25	3.93	31.81	5.632	8.368
16		0.8	25	6.11	36.79	5.669	10.331
18		0.9	25	8.91	39.32	5.672	12.328
20	♣	1	25	9.22	42.63	5.672	14.328
24	✿	1.2	25	13.89	49.75	5.672	18.328
31	❣	1.6	25	25.67	60.63	5.672	25.328
43	✄	2.2	25	44.41	78.26	5.672	37.328
49	✌	2.5	25	53.59	87.93	5.672	43.328
59		3	25	RUPTURED	77.89	5.672	53.328
17		0.5	30	5.42	38.11	9.061	7.939
20	♣	0.6	30	8.26	43.48	9.517	10.483
24	✿	0.7	30	8.48	51.38	9.732	14.268
27	➲	0.8	30	15.11	53.64	9.796	17.204
31	❣	0.9	30	20.65	61.77	9.801	21.199
34	✜	1	30	21.80	66.71	9.801	24.199
48	▼	1.4	30	43.66	89.74	9.801	38.199
54	✖	1.6	30	55.58	97.11	9.801	44.199
27	➲	0.5	35	10.34	54.70	14.388	12.612
32		0.6	35	17.05	63.74	15.112	16.888
38		0.7	35	25.66	73.44	15.453	22.547
43	✄	0.8	35	30.44	81.67	15.556	27.444
49	✌	0.9	35	38.48	93.36	15.563	33.437
54	✖	1	35	44.24	102.07	15.563	38.437
59		1.1	35	45.08	81.45	15.563	43.437
65		1.2	35	RUPTURED	113.44	15.563	49.437
40		0.5	40	19.41	79.80	21.477	18.523
48	▼	0.6	40	26.38	91.71	22.558	25.442
56		0.7	40	35.91	108.36	23.067	32.933
64		0.8	40	45.33	118.78	23.221	40.779
72		0.9	40	RUPTURED	119.28	23.231	48.769

To determine why the 49g_25d_2.5 and 54g_30d_1.6 charges caused higher deflections than the 64g_40d_0.8 charge, their side effective charge masses were compared. Figure 4.6 depicts the respective charge geometries and their respective side effective charge masses.

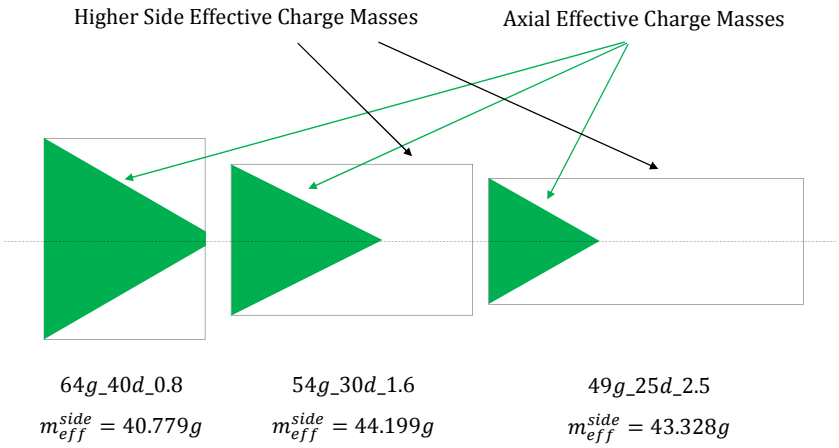

Figure 4.6: Side Effective Charge Mass Comparison – 64g_40d_0.8, 54g_30d_1.6, and 49g_25d_2.5 Charges (Green Represents the Axial Effective Mass, and White is the Side Effective Mass)

The schematic shows that the 54 and 49 g charges (10 and 15 g lighter, respectively) had more side effective charge mass than the 64 g charge, and that explains their greater effect on the maximum diametric deflection of their cylinders. Figure 4.7 depicts the 64g_40d_0.8 cylinder alongside the 54g_30d_1.6, and 49g_25d_2.5 cylinders for comparative purposes.

(a) 64g_40d_0.8 (b) 54g_30d_1.6 (c) 49g_25d_2.5

Figure 4.7: Pictorial Comparison of 64g_40d_0.8, 54g_30d_1.6, and 49g_25d_2.5 Cylinders

Figure 4.8 shows a graph of the maximum diametric deflection *vs* side effective charge mass, grouped according to diameter. The plotted data shows that the maximum diametric deflection is directly proportional to the side effective charge mass, when the diameter is kept constant.

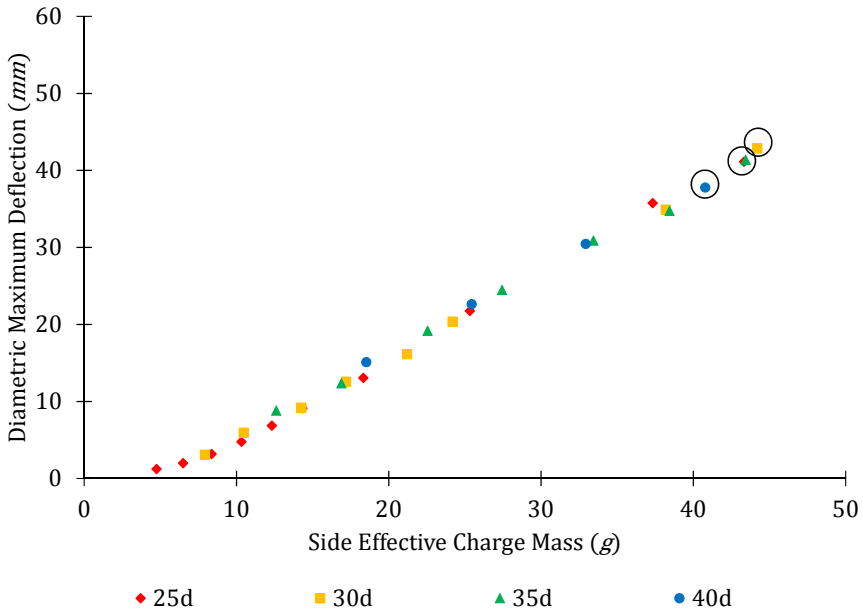

Figure 4.8: Graph of Maximum Diametric Deflection *vs* Side Effective Charge Mass

This graph is the main point of this dissertation, where it is evident that charge geometry plays a major role in the structural response of right circular cylinders to partially confined air blasting. The circled charges (64g_40d_0.8, 54g_30d_1.6, and 49g_25d_2.5) show that light charges can be used to deform a cylinder more effectively than a heavier charge, by increasing the charges length to increase its side effective charge mass.

Photographs of Ruptured Cylinders

Photographs of the cylinders that ruptured are shown in Figure 4.9. These cylinders experienced longitudinal failure and significant axial shortening.

(a) 72g_40d_0.9 (b) 59g_25d_3 (c) 65g_35d_1.2

Figure 4.9: Ruptured Cylinders

4.2.3 Axial Shortening and Secondary Bulge Formation

Figure 4.10 depicts the axial shortening of, and secondary bulge formation on a cylinder after testing. As the aspect ratio of a charge increased, where the diameter was kept constant, the axial shortening of its cylinder increased (as shown in Table 4.1). Some 25 mm diameter tests displayed little to no evidence of a secondary bulges at their clamped ends (that is, the $10 - 18$ g tests). The remaining cylinders had secondary bulges.

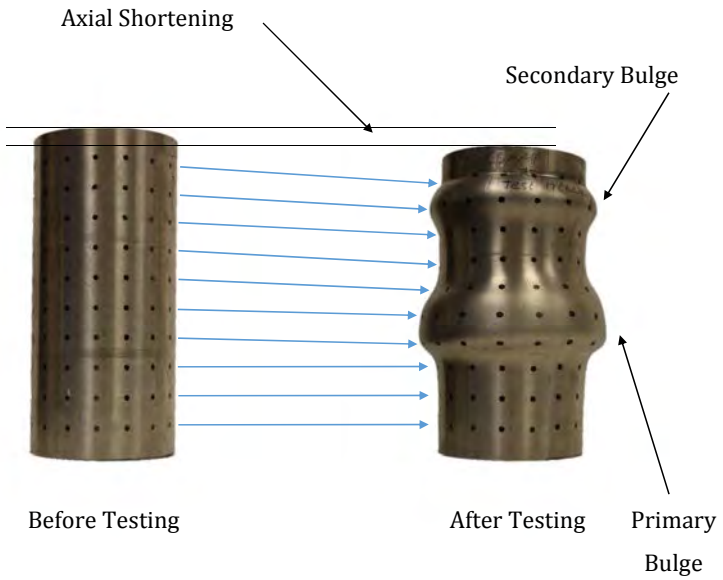

Figure 4.10: Photographs Showing Axial Shortening of, and Secondary Bulge Formation on a Cylinder (64g_40d_0.8)

Figure 4.11 presents a graph of shortening to the maximum diametric deflection. The axial shortening is directly proportional to the maximum diametric deflection because the sideways movement of the cylinder wall caused the face at the open end of each cylinder to travel in the direction of the clamped region. Figure 4.11 and 4.8 are complimentary because it is evident that an increase of the side effective charge mass causes an increase in the axial shortening.

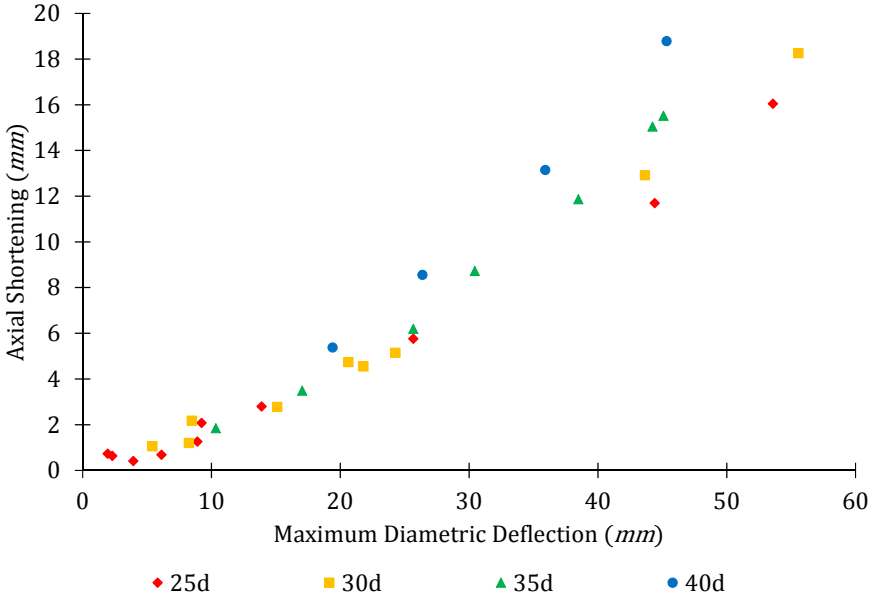

Figure 4.11: Graph of Axial Shortening (Constant Diameter *vs* Maximum Diametric Deflection

4.3 Axial Impulses

Figure 4.12 shows graphs of axial impulse versus aspect ratio, where the diameter and mass are kept constant. The axial impulses of the original and repeat tests were added herein.

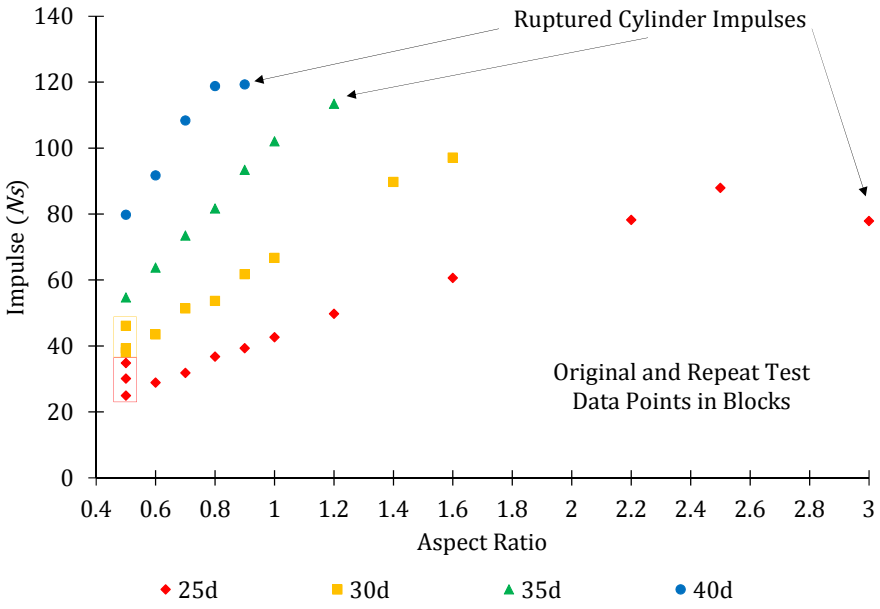

(a) Constant Diameter

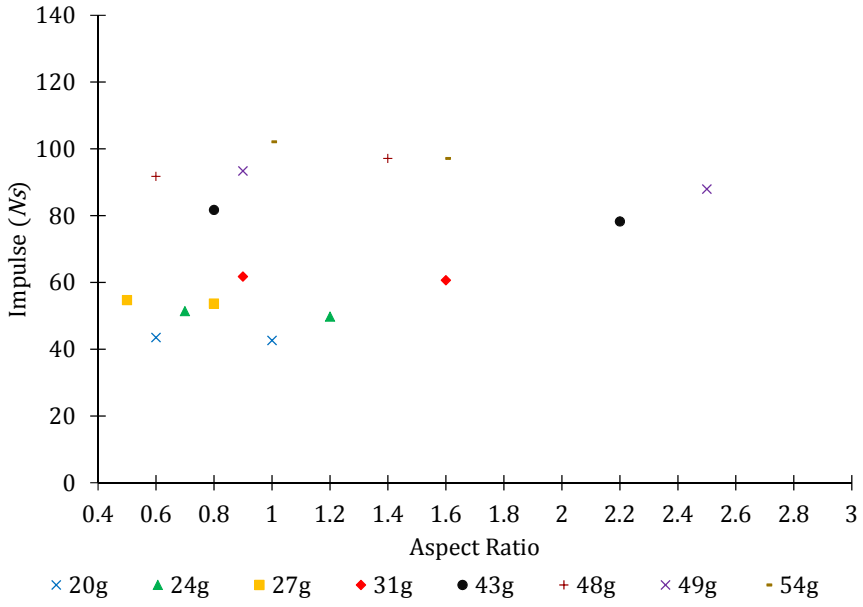

(b) Constant Mass

Figure 4.12: Graphs of Axial Impulse *vs* Aspect Ratio

Constant Diameter

It is observed from Figure 4.12(a) that the axial impulse is directly proportional to the aspect ratio, when the charge mass is kept constant, until it levels off at the end. Also, the rate at the which impulse changed, with respect to aspect ratio, increased as the diameter increased.

Constant Charge Mass, and Effective Charge Mass Effects

Figure 4.12(b) presents the effect of aspect ratio on the axial impulse where the mass is kept constant. Axial impulses from the shorter charges were greater than those obtained from the mass equivalent longer charges. This was because the shorter charge had higher axial effective charge masses than their mass equivalent longer charges. The axial effective charge mass and impulse colums of Table 4.2 confirms the fact that shorter charges had a greater effect on the axial impulse than the mass equivalent longer charge, because the shorter charge had a bigger diameter (this is further discussed in Chapter 7).

A graph of the axial impulse versus the axial effective charge mass is shown in Figure 4.13, where the diameter is kept constant. The axial impulse increased as the axial effective charge mass increased, and continued to increase while the axial effective charge mass remained constant (that is, the axial effective charge mass was a full cone, not a truncated cone).

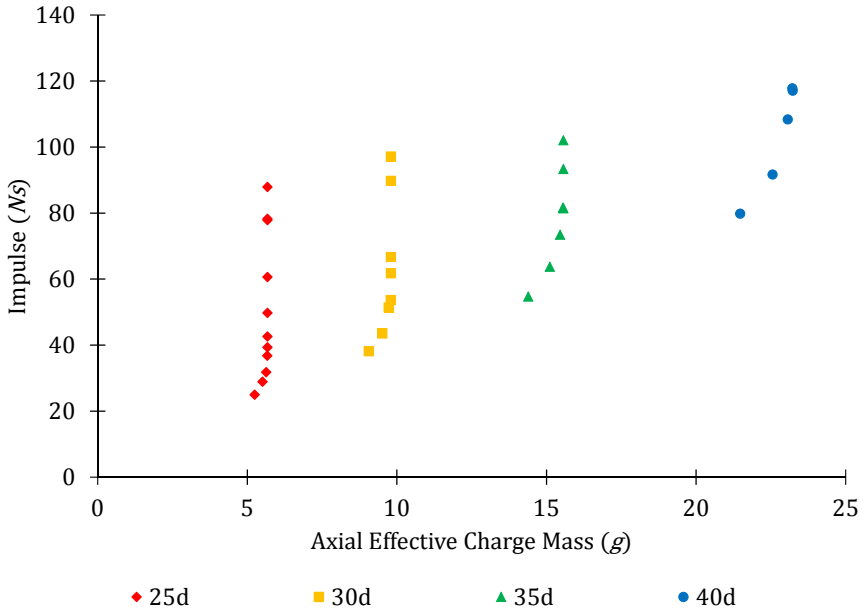

Figure 4.13: Proportionality of Axial Impulse to Axial Effective Charge Mass (Constant Diameter)

The plotted data, when used in conjunction with the plotted data of Figure 4.12(a), also shows that when the aspect ratio was above the aspect ratio of the Kennedy [13] criteria for flat plates, the partial confinement of a cylindrical charge played a bigger role in the axial impulse that was transferred to the ballistic pendulum. This meant that the accumulation and reaction of the detonation products with the remaining oxygen increased the gas pressure at the pendulum. These observations are depicted in Figure 4.14.

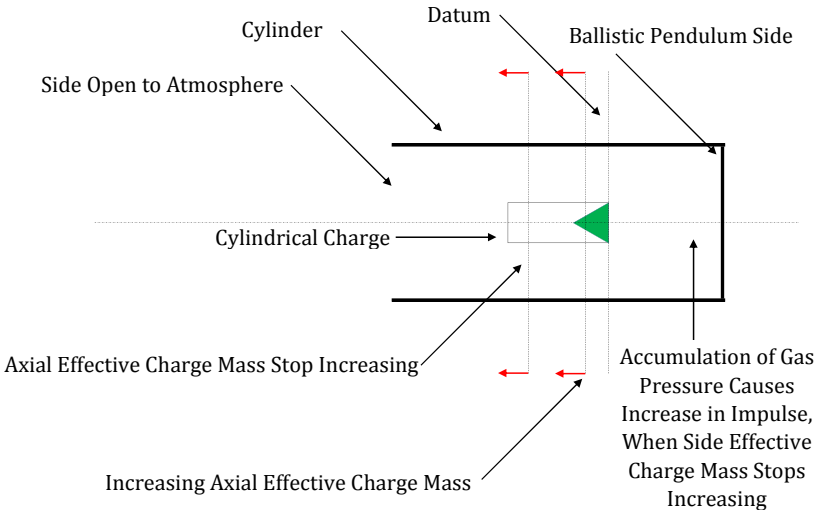

Figure 4.14: Effect of Increasing Axial Effective Charge Mass on the Impulse (Green Represents the Axial Effective Charge Mass)

4.4 Repeatability Tests

Repeatability tests were carried out to see if the experimental data set was reliable. Figure 4.15 depicts the original and repeat test cylinders that were loaded by the 10 g, 25 mm diameter, 0.5 aspect ratio (that is, 10g_25d_0.5) charges.

(a) Original (b) Repeat 1 (c) Repeat 2

Figure 4.15: Photographs of Original and Repeatability Test Cylinders (10g_25d_0.5)

The averages (μ) and standard deviations (σ) of the impulses, maximum diametric deflections, and axial shortenings were calculated using Equation 4.6.

$$\mu = \sum_{i=1}^{3} R_i \quad , \quad \sigma = \sqrt{\frac{\sum_{i=1}^{3} (R_i - \mu)^2}{3}} \tag{4.6}$$

where R_i is the i^{th} reading in the sample.

The standard error was calculated using Equation 4.7.

$$E_{std} = \frac{\sigma}{\sqrt{3}} \tag{4.7}$$

Table 4.3 presents the repeatability test results of the 10g_25d_0.5 charges. The standard errors of the maximum deflection and the axial shortening are less than 1 cylinder thickness, and the standard error of the axial impulse is less than 7% of the original test magnitude.

Table 4.3: Repeatability Test Results (10g_25d_0.5)

Charge	**Type**	**Impulse** (Ns)	**Max. Defl.** (mm)	**Short.** (mm)
10g_25d_0.5	Original	24.96	1.95	0.73
10g_25d_0.5	Repeat 1	30.10	1.81	0.21
10g_25d_0.5	Repeat 2	34.82	1.31	0.26
Average		29.96	1.69	0.40
Std Dev.		2.77	0.34	0.29
Std Error.		1.60	0.19	0.17

Figure 4.16 depicts the original and repeat test cylinders that were loaded by 17g_30d_0.5 charges.

(a) Original (b) Repeat 1 (c) Repeat 2

Figure 4.16: Photographs of Original and Repeatability Test Cylinders (17g_30d_0.5)

Table 4.4 presents the repeatability test results of the 17g_30d_0.5 charges. Similar to the 10g_25d_0.5 tests, the standard errors of the maximum deflection and the axial shortening are less than 1 cylinder thickness, and the standard error of the axial impulse is less than 7% of the original test magnitude. The data of both sets shows that the tests are repeatable.

Table 4.4: Repeatability Test Results (17g_30d_0.5)

Charge	**Type**	**Impulse** (Ns)	**Max. Defl.** (mm)	**Short.** (mm)
17g_30d_0.5	Original	38.11	5.42	1.05
17g_30d_0.5	Repeat 1	46.10	4.95	0.95
17g_30d_0.5	Repeat 2	39.24	5.41	0.97
Average		41.15	5.26	0.99
Std Dev.		4.32	0.27	0.05
Std Error.		2.50	0.16	0.03

4.5 Charge Geometry

Spherical charges were detonated and the structural response was compared to tests using mass equivalent cylindrical charges, all of which had an aspect ratio of 1. Table 4.5 presents the maximum diametric deflections and axial shortenings that were caused by the cylindrical and spherical charges. Note that the notation used to describe each spherical charge is: CHARGE MASS_CHARGE RADIUS_ASPECT RATIO.

Table 4.5: Comparison of Loading and Responses from Tests with Cylindrical (Aspect Ratio = 1) and Mass Equivalent Spherical Charges

Charge	**Imp.**	**Defl.**	**Short.**	**Charge**	**Imp.**	**Defl.**	**Short.**
Max. Diam. Defl. and Axial Short. Units in mm, Axial Impulse Units in Ns							
Cylindrical Charges				**Spherical Charges**			
20g_25d_1	42.63	9.22	2.08	20g_14.3d_1	41.60	4.58	0.93
34g_30d_1	66.71	21.59	4.55	34g_17.18d_1	71.25	13.43	0.97
54g_35d_1	102.07	44.24	15.05	54g_20.04d_1	94.83	26.68	8.27

Cylindrical charges caused greater deflections and higher quantities of axial shortening than their mass equivalent spherical charges. The axial impulses are similar to each other. Photographs of cylinders loaded with cylindrical and mass equivalent spherical charges are shown in Figure 4.17.

(a) 20g_25d_1 (b) 20g_14.39d_1 (c) 34g_30d_1 (d) 34g_17.18d_1

(e) 54g_35d_1 (f) 54g_20.04d_1

Figure 4.17: Photographs of Cylinders Loaded with Cylindrical and Mass Equivalent Spherical Charges ($R_{ld} = 1$)

The cylindrical charges caused much larger diametric deflections (almost twice that caused by the spherical charges) that were more localised to the charge location. Here it is important to remember that the cylindrical charges had their detonators placed at a depth of 5 mm, and the spherical charges had their detonators placed at centre depth. The charge shape was the most probable cause of the sharper primary bulges on the cylinders. Also, the cylindrical charges caused more axial shortening of their cylinders (more than twice that caused by the spherical charges). Meanwhile, the axial impulses differed by less than 10%.

4.6 Detonator Position

A preliminary investigation into the effect of detonation position was conducted to determine its effect on the deflection profile of a cylinder. A 34 g cylindrical charge was detonated at its geometric centre.

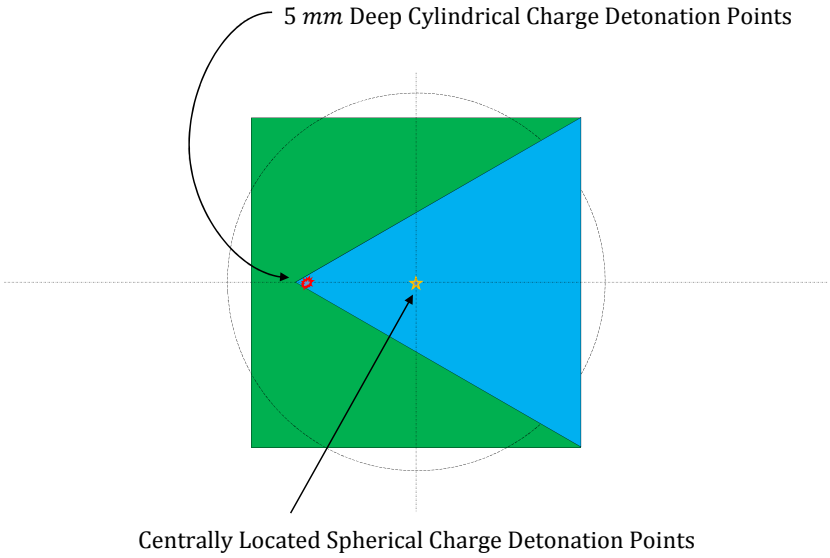

Figure 4.18: Superposed Schematics of 34 g Cylindrical and Spherical Charges ($R_{ld} = 1$)

Figure 4.19 depicts the cylinders that were affected by these charges, where the overall deformed shapes are similar. The primary bulge peak of the centre detonation cylinder was 15.26 mm further from the clamped region than the other cylinder.

(a) 5 mm Depth (b) Centre Det.

Figure 4.19: Cylinders Loaded by 34g_30d_1 Charges

Table 4.6 presents the maximum diametric deflections, the axial impulses, and the axial shortenings of the cylinders that were affected by the cylindrical charge that was detonated at a 5 mm depth and the centrally detonated cylindrical charge. The axial shortenings and maximum diametric deflections differ

by less than 1 and 2 cylinder thicknesses, respectively. Meanwhile, the impulses differ by less than 7% of the 34g_30d_1 test magnitude.

Table 4.6: Deflections, Impulses, and Shortenings of Cylindrical and Mass Equivalent Spherical Charges

Charge	**Impulse** (Ns)	**Max. Defl.** (mm)	**Axial Short.** (mm)
34g_30d_1	66.71	21.59	4.55
34g_30d_1 (Centre Det.)	73.51	24.30	5.14
Difference	6.80	2.71	0.59

The data in Table 4.6, when used in conjunction with Figure 4.19, shows that the detonator position had a small effect on the maximum diametric deflection, impulse, and axial shortening. Note that only one such test was run and that the result is only indicative of the fact that detonator position has an effect on the physical quantities in question.

5

Material Characterisation

Curved specimens were cut from a seamless 304 stainless steel cylinder. Vickers hardness and quasi-static tensile tests were performed on these specimens. The specifications for the tensile test pieces were: 2 mm gauge thickness, 12.5 mm gauge width, and 75 mm gauge length. The cross sectional area, along the gauge length, was 25 mm^2. Figure 5.1 depicts the dimensions of the curved specimens, all of which were compliant with the ASTM standard for tensile testing [37].

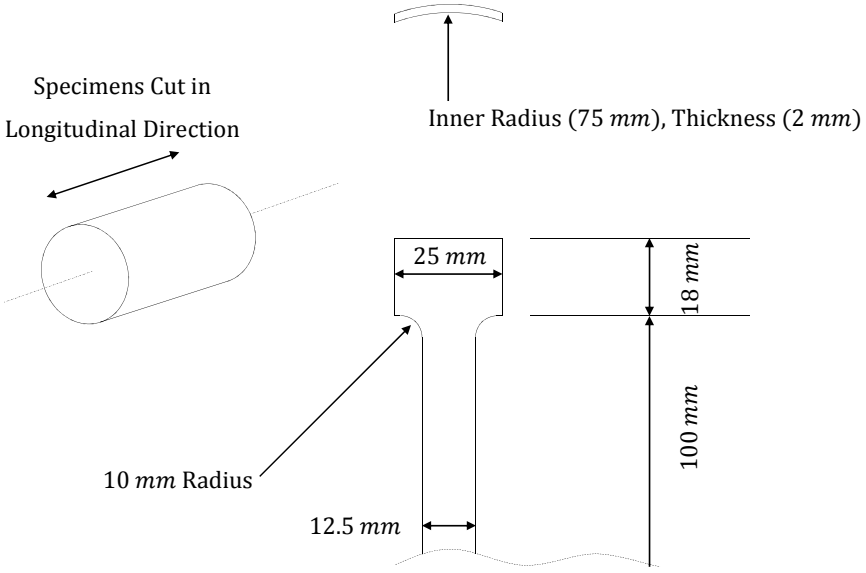

Figure 5.1: Dimensions of the Curved Specimen

The purpose of these specimens was to characterise the seamless 304 stainless steel in the as received (that is, curved) state to determine the Johnson-Cook material parameters for the simulated blast model.

5.1 Vickers Hardness Testing

5.1.1 Description

Vickers hardness testing was used to determine the resistance of 304 stainless steel to localised plastic deformation and to infer the ultimate tensile strength of the material. A square pyramidal diamond-shaped indenter was used to apply the force to initiate plastic deformation.

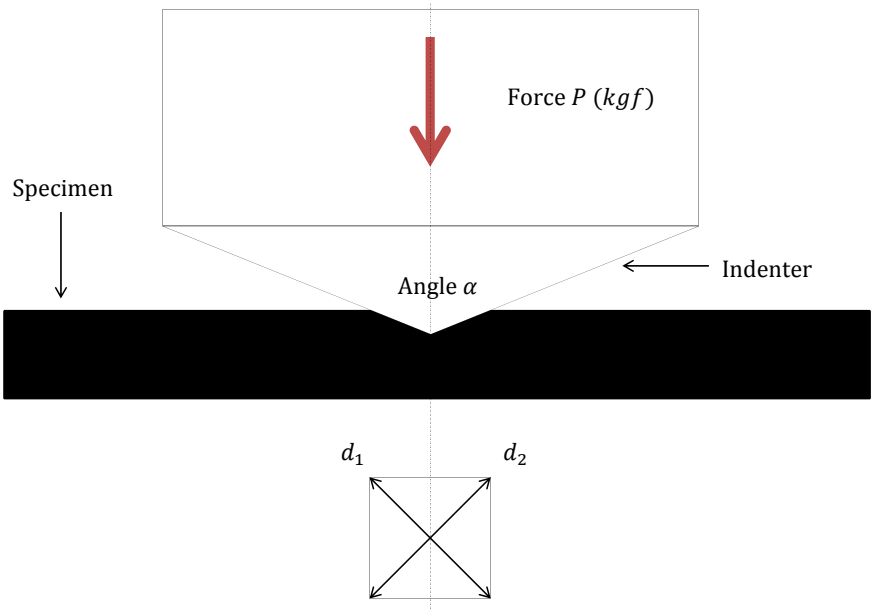

Figure 5.2: Vickers Hardness Test Schematic [24] (View of Indentation Also Shown)

The Vickers hardness was calculated using Equation 5.1.

$$HV = \frac{2Psin\left(\frac{\alpha}{2}\right)}{d^2} \tag{5.1}$$

Where P is the force of the indenter in kgf, α is the 136˚insert indenter angle, and d is the mean Vickers diagonal in μm, which was calculated using Equation 5.2.

$$d = \frac{d_1 + d_2}{2} \tag{5.2}$$

The centre to centre distance between each indentation was greater than 2.5 mean Vickers diagonals [24], to ensure that material properties of the surrounding material was not affected. To account for temperature related effects, the ASTM standard [24] recommended that testing be carried out in an area where the room temperature is between 10 and 35˚C. Vickers hardness tests were performed along the gauge lengths of six curved dog bone specimens, because it was along this length that the UTS of the material was determined after quasi-static tensile testing. Twelve indentations were made on each specimen (that is, six at 10 kgf, and six at 20 kgf).

5.1.2 Results

Table 5.1 presents the Vickers Hardness test results. For both test cases, the averages and medians of all physical quantities are very close, which means that the scattered data was very well distrubuted.

Table 5.1: Vickers Hardness Test Results (HV Units in kg/mm^2)

Test	$d1$ (μm)	$d2$ (μm)	HV	$d1$ (μm)	$d2$ (μm)	HV	$d1$ (μm)	$d2$ (μm)	HV
INDENTER SET AT 10 kgf FOR 10 s									
-	**Specimen 1**			**Specimen 2**			**Specimen 3**		
1	310.3	311.8	191.7	310.3	309.6	193.0	307.0	298.4	202.4
2	315.9	314.0	186.9	314.8	314.0	187.6	301.4	302.9	203.1
3	301.4	319.6	192.3	305.9	314.0	193.0	284.7	297.3	219.0
4	311.4	310.7	191.7	307.0	314.0	192.3	299.2	295.1	210.0
5	319.3	311.8	186.2	312.6	307.4	193.0	294.7	295.1	213.2
6	309.2	314.0	191.0	318.1	308.5	188.9	301.4	301.8	203.9
-	**Specimen 4**			**Specimen 5**			**Specimen 6**		
1	315.9	318.5	184.3	330.4	311.8	179.9	308.1	304.0	198.0
2	313.7	314.0	188.3	318.4	305.1	190.8	304.7	305.1	199.5
3	321.5	317.4	181.7	307.0	319.6	188.9	322.6	306.2	187.6
4	307.0	308.5	195.8	322.6	316.3	181.7	323.7	315.1	181.8
5	308.1	320.7	187.6	318.1	320.7	181.8	321.5	316.3	182.3
6	318.1	308.5	188.9	315.9	312.9	187.6	313.7	315.1	187.6
-	**Max.** $d1$		330.4	**Max.** $d2$		320.7	**Max.** HV		219.0
-	**Min.** d_1		284.7	**Min.** d_2		295.1	**Min.** HV		179.9
-	**Ave.** d_1		311.5	**Ave.** d_2		310.4	**Ave.** HV		192.0
-	**Med.** d_1		312.0	**Med.** d_2		311.8	**Med.** HV		189.9
-	**Std Dev.** d_1		9.1	**Std Dev.** d_2		7.1	**Std Dev.** HV		9.1
-	**Std Err.** d_1		1.5	**Std Err.** d_2		1.2	**Std Err. of** HV		1.5
INDENTER SET AT 20 kgf FOR 10 s									
-	**Specimen 1**			**Specimen 2**			**Specimen 3**		
1	457.7	443.2	182.8	433.1	429.8	199.2	447.6	447.7	185.1
2	442.0	443.2	189.3	444.3	435.4	191.7	455.4	449.9	181.0
3	446.5	435.4	190.7	439.8	436.5	193.2	452.1	448.8	182.8
4	445.4	442.1	188.3	438.7	439.9	192.2	440.9	449.9	186.9
5	443.2	441.0	189.8	439.8	429.8	196.2	447.6	458.8	180.6
6	440.9	448.8	187.4	427.5	425.4	203.9	452.1	435.4	188.3
-	**Specimen 4**			**Specimen 5**			**Specimen 6**		
1	433.1	438.8	195.1	451.0	455.5	180.5	452.1	455.5	180.1
2	443.2	427.6	195.6	452.1	456.6	179.7	454.3	461.0	177.1
3	435.3	434.3	196.2	454.3	456.6	178.8	459.9	454.3	177.5
4	437.6	425.4	199.2	451.0	459.9	178.8	464.4	459.9	173.6
5	429.8	439.9	196.1	458.8	462.1	174.9	448.7	462.1	178.8
6	435.3	431.0	197.7	462.1	448.9	178.8	459.9	451.0	178.8
-	**Max.** d_1		464.4	**Max.** d_2		462.1	**Max.** HV		203.9
-	**Min.** d_1		427.5	**Min.** d_2		425.4	**Min.** HV		173.6
-	**Ave.** d_1		446.6	**Ave.** d_2		445.0	**Ave.** HV		186.9
-	**Med.** d_1		447.1	**Med.** d_2		445.5	**Med.** HV		187.2
-	**Std Dev.** d_1		9.5	**Std Dev.** d_2		11.3	**Std Dev.** HV		8.1
-	**Std Err.** d_1		1.6	**Std Err.** d_2		1.9	**Std Err. of** HV		1.4

As expected, the average and median d_1 and d_2 magnitudes of the 20 kgf indenter setting were greater than those of the 10 kgf indenter setting. The standard deviations of the d_1 and d_2 magnitudes, for both indenter settings, were less than 3% of their averages and medians, which meant that both data sets were reliable.

The UTS magnitudes were inferred from the Böhler table [38] with linear interpolation. The average inferred UTS magnitude from the 10 kgf indenter setting was 616.67 MPa, and from the 20 kgf indenter setting was 599.75 MPa. The higher magnitude of the inferred UTS differed by 16.92 MPa (that is, less than 3%) from the lower magnitude.

5.2 Quasi-Static Tensile Testing

5.2.1 Curved Specimens and the Insert Design

Two options existed: the specimens could be flattened, in preparation for 'standard' quasi-static tensile testing, or the specimens could be tested in the as received (that is, curved) state. Flattening the curved specimens would have strain hardened the material, and this would have affected the final results after testing and data processing, which meant that the results would not have been representative of the cylinders material. Note that Ozinsky *et al.* [22, 23] flattened his curved specimens, before quasi-static tensile testing, to fit into the existing flat specimen inserts. To prevent the strain hardening problem, a new set of inserts were designed to test the material in the as received state. The inserts were designed to surround the grip length and shoulder of the specimen. Figure 5.3 is a schematic of the curved specimen between the inserts.

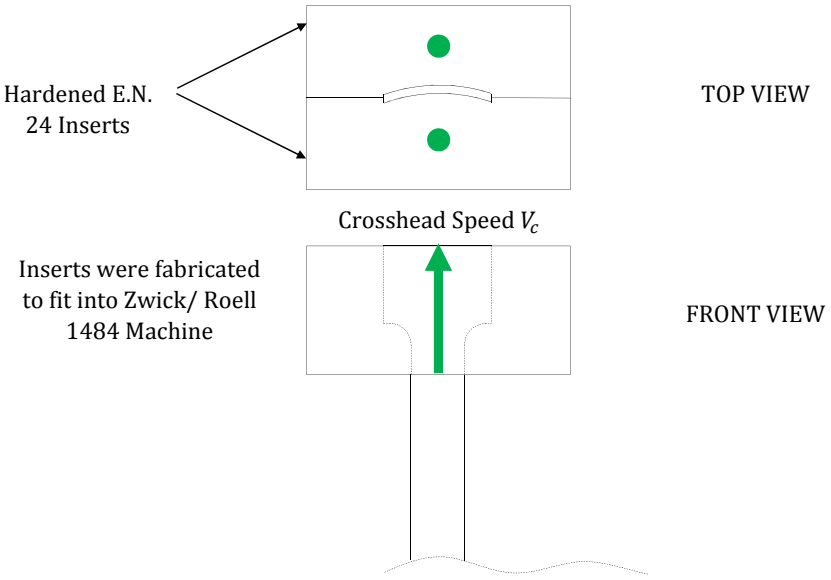

Figure 5.3: Schematic of the Curved Specimen Between the Inserts

The inserts were manufactured using EN24 (German standard 1,6582 [39]) billets. After machining, the inserts were heated to 860°C and kept at temperature for an hour. After heating, the inserts were quenched in oil at room temperature, allowed to cool, then cleaned with soap and water. After cleaning, the inserts were tempered at 540°C and kept at temperature for an hour [40]. After tempering, the inserts were removed from the furnace and cooled in air at room temperature.

5.2.2 Force-Travel Data Processing

Calculation of Strain Rate

A Zwick 1484 universal tensile/ compression machine was used to quasi-statically test the curved specimens. The strain rate was calculated using Equation 5.3.

$$\dot{\epsilon} = \frac{1}{L_{specimen}} \frac{V_{crosshead}}{60} = \frac{1}{75} \frac{4.5}{60} = 1e-3 \qquad s^{-1} \tag{5.3}$$

Where V_c is the crosshead speed (units in mm/min) and $L_{specimen}$ is the original gauge length of the specimen.

Removal of Machine Compliance

Four specimens were tested and their force-travel curves, shown in Figure 5.4, were generated.

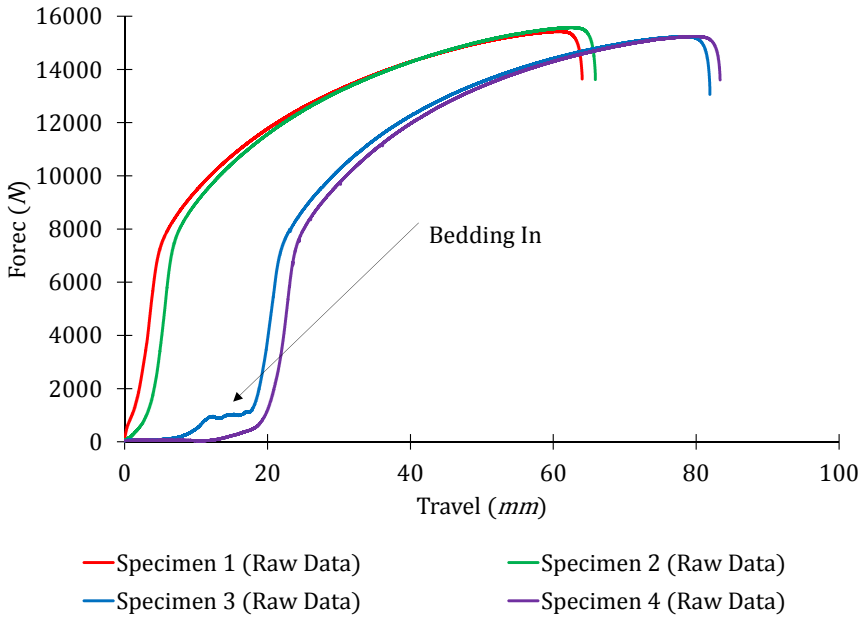

Figure 5.4: Raw Force-Displacment Curves

Finding the elongation of the specimen from rest required that machine compliance (that is, elastic deflection of the machine in the axial direction) be removed. The first step, to remove the machine compliance, involved truncating the bedding in behaviour on each curve. Truncation was done by generating a straight line that fit the linear region of each force-travel curve, where the straight line gradient, $k_{effective}$, included machine and specimen compliance. The modified (that is, raw data minus the bedding) data curves are depicted in Figure 5.5. Note the closeness of the $k_{effective}$ magnitudes to each other.

The specimen and machine were parallel springs, which meant that the machine stiffness was calculated using Equation 5.4.

$$k_{machine} = \left(\frac{1}{k_{effective}} - \frac{1}{k_{specimen}} \right)^{-1} \tag{5.4}$$

Where $k_{specimen}$ is the stiffness of the specimen that was calculated using Equation 5.5.

$$k_{specimen} = \frac{E_{specimen} A_{specimen}}{L_{specimen}} \tag{5.5}$$

Where $E_{specimen}$ is the Young's modulus of the specimen, and $A_{specimen}$ is the cross sectional area of the specimen before testing. Equation 5.6 was used to correct the modified data, as shown on Figure 5.6.

$$d_i^{corrected} = d_i^{modified} - \frac{F_i^{modified}}{k_{machine}} - d_{shift} \tag{5.6}$$

Where $F_i^{modified}$ is the raw data force minus the bedding in, $d_i^{modified}$ is the raw data travel minus the bedding in, and d_{shift} is the distance from zero standard travel to the standard travel intercept of the modified data curve.

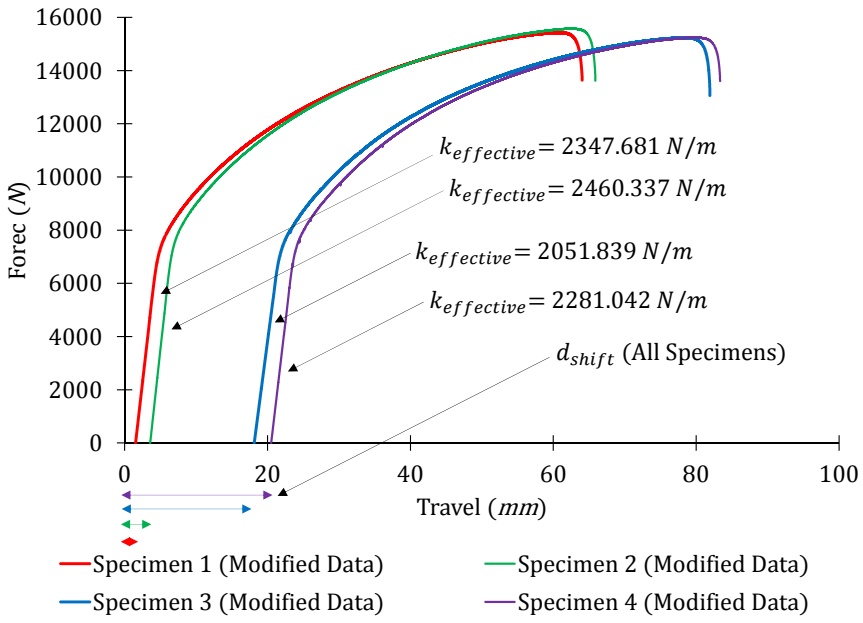

Figure 5.5: Modified Force-Displacment Curves

5.2.3 Stress-Strain Data Processing

Engineering Stress-Strain

After machine compliance removal, the engineering strain and stress was calculated using Equation 5.7.

$$\epsilon_i^{engineering} = \frac{d_i^{corrected}}{L_{specimen}} \quad , \quad \sigma_i^{engineering} = \frac{F_i^{corrected}}{A_{specimen}} \tag{5.7}$$

Where $F_i^{corrected}$ is the corrected standard force. Figure 5.7 depicts the engineering stress-engineeirng strain curves, where four specimens were tested at a crosshead speed of 4.5 mm/min. The gauge length was 75 mm, the thickness was 2 mm, the cross sectional area was 25 mm^2, and the Young's modulus was 200 GPa. Therefore, the strain rate, $\dot{\epsilon}_0$, was $0.001/s$.

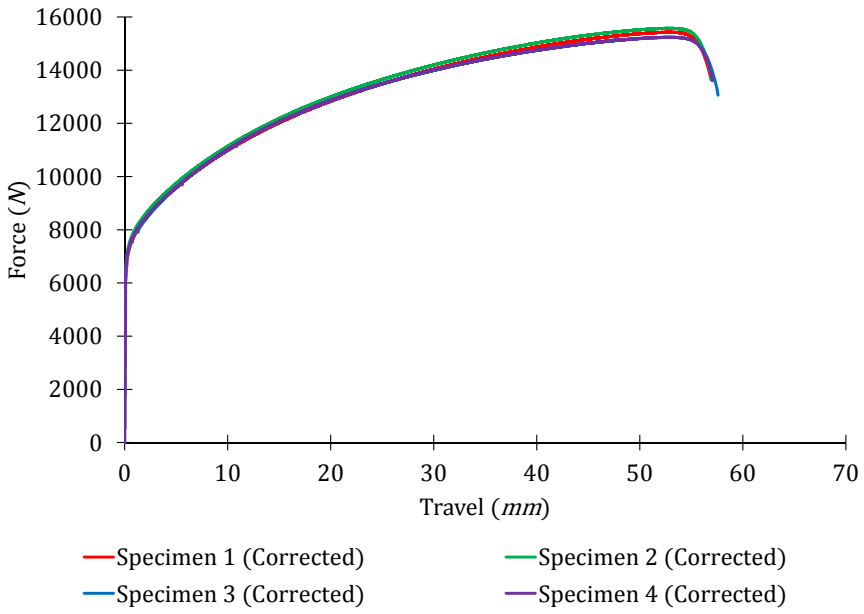

Figure 5.6: Corrected Force-Travel Curves

Figure 5.7 shows that the quasi-static tensile testing of the curved dogbone specimens was highly repeatable, because the behaviour of all four specimens was similar.

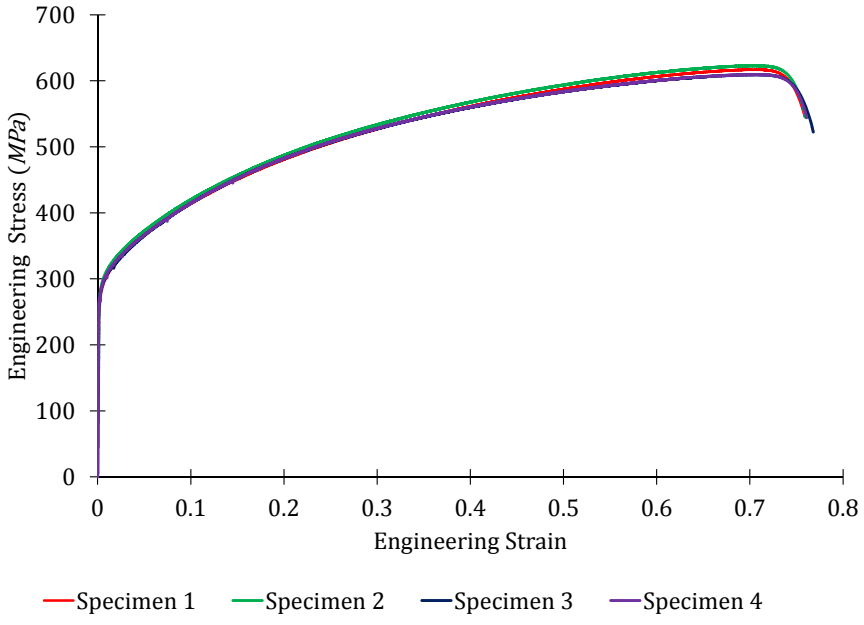

Figure 5.7: Engineering Stress-Engineering Strain Curves

Finding the 0.2% Proof Stress and the UTS

The 0.2% proof stress was determined by taking a line that was parallel to the elastic portion of the engineering stress-strain curve, making its engineering strain intercept equal to 0.002, and finding the point where the line and the engineering stress-strain curve intersected. The straight line that was used to find the intersection point on the engineering stress-engineering strain curves is given by Equation 5.8.

$$\sigma^{engineering} = E\epsilon^{engineering} - 0.002E \tag{5.8}$$

The UTS was the maximum value on each engineering stress-strain curve. Table 5.2 presents the 0.2% yield stress, UTS, and fracture strain magnitudes of all specimens.

Table 5.2: 0.2% Engineering Yield Stress, UTS, and Fracture Strains

Specimen	$A\ (MPa)$	ϵ_{yield}	$UTS\ (MPa)$	$\epsilon_{fracture}$
1	277.25	0.0034	617.01	0.76
2	284.33	0.0034	622.88	0.76
3	280.69	0.0034	609.30	0.77
4	281.66	0.0034	609.51	0.76
Average	280.98	0.0034	614.67	0.76
Standard Deviation	2.926	1.252e-05	6.539	0.004
Standard Error	1.463	6.151e-06	3.269	0.002

The 0.2% yield stress values were 9.6% lower than the the value used by Ozinsky *et al.* [22, 23] (that is, 310 MPa), which was expected because Ozinsky *et al.* [22, 23] strain hardened (that is, flattened) the curved specimens before testing. The UTS magnitudes from the tests were very close to the average inferred values of the Vickers hardness tests for the 10 and 20 kgf indenter settings (that is, 616.67 and 599.75 MPa, respectively), which meant that both Vickers hardness data sets were reliable.

Calculation of Plastic Strain and True Stress

The true strain was calculated using Equation 5.9.

$$\epsilon_i^{true} = \int_{L_{specimen}}^{L_{instantaneous}} \frac{dL}{L} = ln\left(\frac{L_{instantaneous}}{L_{specimen}}\right) = ln\left(\frac{L_{specimen} + d_i^{corrected}}{L_{specimen}}\right) = ln\left(1 + \epsilon_i^{engineering}\right) \tag{5.9}$$

Where $L_{instantaneous}$ is the instantaneous length of the specimen. The true strain, which is a combination of the elastic and plastic strains, was calculated using Equation 5.10.

$$\epsilon_i^{true} = \epsilon_i^{elastic} + \epsilon_i^{plastic} = \frac{\sigma_i^{engineering}}{E_{specimen}} + \epsilon_i^{plastic} \tag{5.10}$$

The plastic strain was calculated using Equation 5.11.

$$\epsilon_i^{plastic} = ln\left(1 + \epsilon_i^{engineering}\right) - \frac{\sigma_i^{engineering}}{E_{specimen}} \tag{5.11}$$

Before the true stress was calculated, Equation 5.12, which presents the conservation of volume, was derived.

$$A_{specimen}L_{specimen} = A_{instantaneous}L_{instantaneous} = A_{instantaneous}\left(L_{specimen} + d_i^{corrected}\right) \tag{5.12}$$

Where $A_{instantaneous}$ is the instantaneous cross sectional area of the specimen. Equation 5.7 and 5.12 was combined, and the true stress was calculated using Equation 5.13.

$$\sigma_i^{true} = \frac{F_i^{corrected}}{A_{instantaneous}} = \frac{F_i^{corrected}}{A_{instantaneous}}\frac{A_{specimen}}{A_{specimen}} = \sigma_i^{engineering}\left(\epsilon_i^{engineering} + 1\right) \tag{5.13}$$

The true stress-plastic strain data was valid between the 0.2% yield stress and the UTS. Equation 5.14 gives the lower and upper limits of the true stress.

$$\epsilon_1^{plastic} = ln\left(1 + \epsilon_{yield}^{engineering}\right) - \frac{\sigma_{yield}^{engineering}}{E_{specimen}} \quad , \quad \epsilon_N^{plastic} = ln\left(1 + \epsilon_{UTS}^{engineering}\right) - \frac{\sigma_{UTS}^{engineering}}{E_{specimen}} \tag{5.14}$$

Equation 5.15 gives the lower and upper limits of the plastic strain.

$$\sigma_1^{true} = \sigma_{yield}^{engineering}\left(\epsilon_{yield}^{engineering} + 1\right) \quad , \quad \sigma_N^{true} = \sigma_{UTS}^{engineering}\left(\epsilon_{UTS}^{engineering} + 1\right) \tag{5.15}$$

Figure 5.8 depicts the true stress-plastic strain curves. There was some variation between the true stress at maximum. The respective specimens true stresses (corresponding plastic strains in brackets) are 1071.14 ($\epsilon_{plastic} = 0.542$), 1071.14 ($\epsilon_{plastic} = 0.542$), 1049.46 ($\epsilon_{plastic} = 0.545$), and 1049.37 ($\epsilon_{plastic} = 0.545$) MPa.

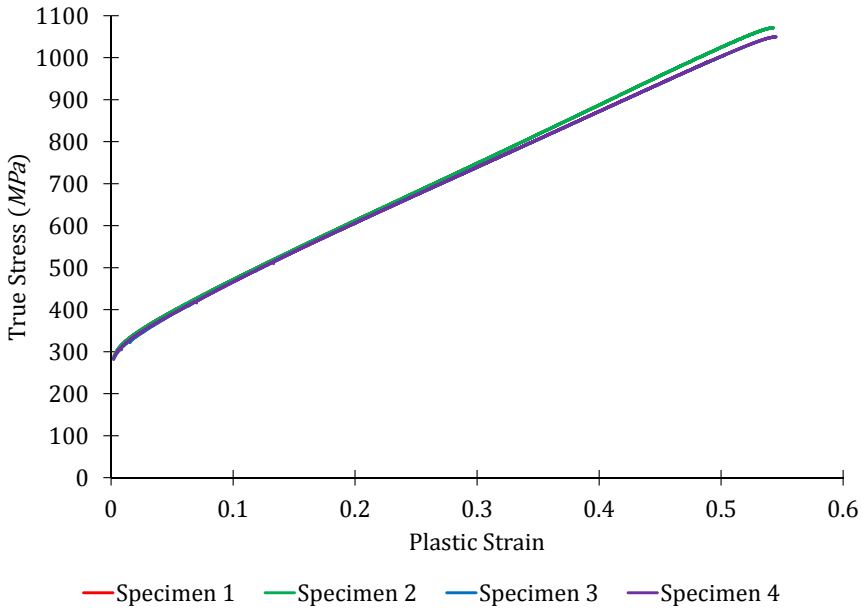

Figure 5.8: True Stress-Plastic Strain Curves

Fitting the Ludwik Equation to the True Stress-Plastic Strain Data

The Ludwik Equation is described by Equation 5.16.

$$\sigma_{ludwik} = A + B\epsilon^{n}_{plastic} \tag{5.16}$$

Where A is the yield stress that was found using the 0.2% offset strain method, B is the strength coefficient, and n is the strain hardening exponent. The Ludwik Equation was fit to the true stress-plastic strain data using Least Squares Regression. The residual sum of squares was calculated using Equation 5.17.

$$R_{ss} = \sum_{i=1}^{N} \left(\sigma_i^{ludwik} - \sigma_i^{true}\right)^2 \tag{5.17}$$

Where N is the total number of plot points on the graph. The correlation parameter was calculated using Equation 5.18.

$$R^2 = 1 - \frac{R_{ss}}{\sum_{i=1}^{N} \left(\sigma_i^{true} - \bar{\sigma}^{true}\right)^2} \tag{5.18}$$

Where $\bar{\sigma}^{true}$ is the mean true stress. To maximise the correlation parameter, B and n were regressed with the EXCEL solver tool. Table 5.3 presents the final Johnson-Cook parameters for all tensile test specimens.

Table 5.3: Final Johnson-Cook Parameters

Specimen	$A\ (MPa)$	$B\ (MPa)$	n	R^2
1	277.25	1339.09	0.85	0.998862709
2	284.33	1343.11	0.87	0.999218485
3	280.69	1298.96	0.86	0.999621931
4	281.66	1298.65	0.86	0.999574381
Average	280.98	1319.95	0.86	—
Standard Deviation	2.9263	24.4732	0.0074	—
Standard Error	1.4631	12.2366	0.0037	—

The closeness of the index strength and strain hardening exponents to each other reinforced the repeatability of the quasi-static tensile testing procedure of the curved dogbone specimens. The average strain hardening exponent is higher than the value that was used by authors Mori *et al.* [6] and Lee *et al.*[7] who characterised annealed 304 stainless steel. The average A, B, and n values were used in the Johnson-Cook material model of the simulated blast model.

6

Simulated Blast Model Development

In the experiments, transient physical quantities such as pressure and deflection could not be captured. Therefore, the experiments were simulated in LS DYNA, a commercial numerical modelling package that can perform coupled analyses. An example of coupling is the movement of PE4 in an air (that is, Eulerian) mesh, and its fluid-structure interaction with a cylinder (that is, Lagrangian) mesh. This kind of analysis was used in the mesh sensitivity study of the cylinder.

This chapter describes the development of the final LS DYNA input deck where mesh sensitivity studies of the air and cylinder meshes, and their results are presented. The default values of each key card were used, unless stated otherwise.

6.1 Air Mesh Sensitivity Study

6.1.1 General

Shell Elements with an ALE 2D Section

Figure 6.1 depicts a schematic of the arbitrary Lagrange Eulerian (ALE) domain that was used for the air mesh sensitivity test, where cylindrical charges were simulated axisymmetrically about the y axis. The ALE domain, which was 110 mm wide and 311 mm long, had a multi material formulation (ALEFORM = 11) and an axisymmetric area weighted element formulation (ELFORM = 14). Bilinear square elements of different sizes were used to mesh the ALE domain.

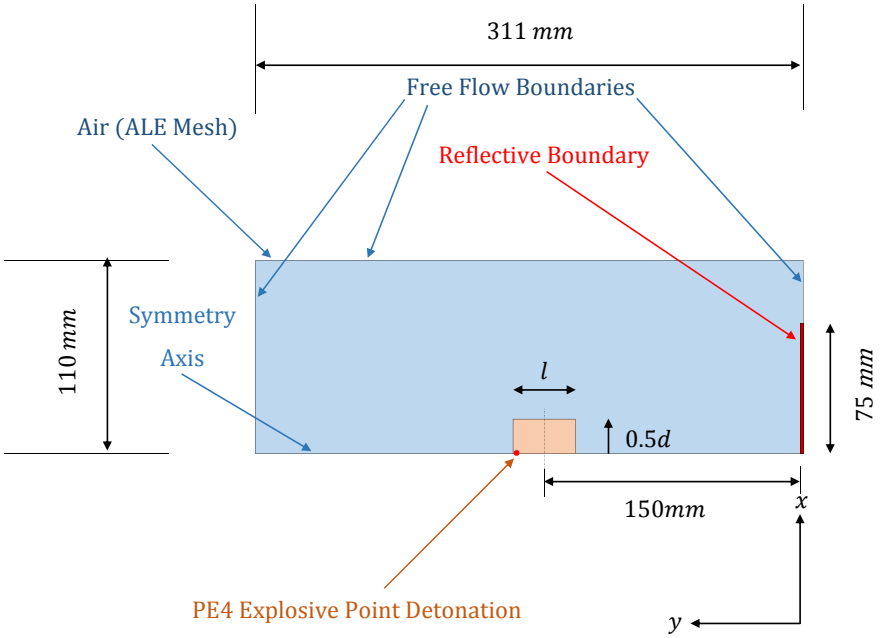

Figure 6.1: Schematic of the ALE Domain Used For the Air Mesh Sensitivity Test

Boundary Conditions (SPC Set)

A reflective boundary (shown in red in Figure 6.1) was defined to simulate the boss plate attached to the ballistic pendulum. This boundary condition was defined by constraining the boundary nodes in the y direction, and was 75 mm long. Three free flow boundaries were defined to allow the air/ PE4 mixture to leave the domain without expecting any return flow. No translational nor rotational constraints were applied to these boundaries or to the symmetry axis.

Control ALE

The global parameters were assigned with the Control ALE key card. The new algorithm (DCT = -1) was used as the default continuum treatment of the domain, because it was recommended for simulations with explosives [41]. The second order accurate Van Leer advection method with half index shift (METH = 2), excluding the monotonicity condition [41], was used. The magnitude of the reference pressure to

compute internal forces, P_{ref}, was set to 103.32 kPa (that is, the value at standard temperature and pressure).

Initial Detonation Point and Volume Fraction Geometry

The explosives detonation was defined with the Initial Detonation key card, the coordinates of which were: $(0, 150 + 0.5l - 5, 0)$.

A 64 g, 40 mm diameter cylindrical PE4 charge detonation (that is, 64g_40d_0.8) was simulated in the ALE mesh sensitivity test. To define the volume of the charge before detonation, the Initial Volume Fraction Geometry key card was used. The cylindrical geometry of the charge was defined using a cuboid/ rectangular container (CONTTYP = 5) with the head side of the container filled with PE4 (FILLOPT = 2). The dimensions of the charge were set by defining the minimum and maximum coordinates of the container, which are presented in Table 6.1.

Table 6.1: Cylindrical Charge Container Geometry Maxima and Minima

Symbol	x_{min}	y_{min}	z_{min}	x_{max}	y_{max}	z_{max}
Magnitude	0	150 - $l/2$	0	$d/2$	150 + $l/2$	0
Where l = charge length, and d = charge diameter						
150 = half the unclamped cylinder length						

To define the number of particles in each ALE element, the number of sampling points, N_{trace}, was defined. This meant that each ALE element was divided into $(2N_{trace} + 1)^2$ regions [1], each of which was filled with a sampling point of PE4. In the blast model, $N_{trace} = 50$, which meant that each ALE element was divided into 10201 regions (that is, has 10201 PE4 particles before detonation).

Hourglassing

Hourglass control was added to the ALE mesh to prevent spurious deformation of the ALE mesh. The standard viscous form of the hourglass control type (IHQ = 1) was used. The hourglass coefficient was set to a value that was appropriate for explosives (QM = 1e-6). The standard bulk viscosity type was set to propagate shockwaves (IBQ = 1). The quadratic bulk viscosity coefficient (Q1 = 1.5), the linear bulk viscosity coefficient (Q2 = 0.06), the hourglass coefficient for shell bending (QB/ VDC = 0.1), and the hourglass coefficient for shell warping (QW = 0.1) were left at their default values.

Energy Control

The controls for energy dissipation were provided using the control energy key card. Hourglass energy (HGEN = 2), and Stonewall energy dissipation were computed and included in the energy balance (RWEN = 2). Sliding interface energy dissipation (SLNTEN = 1), and Rayleigh energy dissipation were not computed nor included in the energy balance (RYLEN = 1).

Time Step Control and Simulated Time Definition (Termination Control)

LS DYNA was set to calculate the initial time step (DTINIT = 0), the scaling factor for the computed time step was set to a value lower than that recommended when simulating high explosives (TSSFAC =

[1] In the keyword manual [41], the exponent was 3, which assumed that a 3D domain was used. In this dissertation, a 2D domain was used.

0.5) [41] to further ensure the stability of the simulations that ran. The simulated time for all ALE mesh sensitivity simulations was 0.2 ms (ENDTIM = 0.2).

6.1.2 Simulated Air, Explosive and Boss

Explosive Material, Equation of State, and Detonation Velocity Variation Check

The behaviour of PE4 was simulated with the Jones Wilkins-Lee (JWL) Equation of State (EOS), as given by Equation 6.1 [42].

$$P = A\left(1 - \frac{\omega}{R_1 V_0}\right)e^{-R_1 V_0} + B\left(1 - \frac{\omega}{R_2 V_0}\right)e^{-R_2 V_0} + \frac{\omega E_0}{V_0} \tag{6.1}$$

Where P is the pressure, A and B are pressure constants, E_0 is the detonation energy per unit volume, R_1, R_2, and ω are unitless constants, and V_0 is the initial relative volume described by Equation 6.2 [42].

$$V_0 = v_{r0} = v_r|_{t=0} = \frac{\rho_0}{\rho|_{t=0}} \tag{6.2}$$

Where $\rho|_{t=0}$ is the density at the first timestep, and ρ_0 is the reference density.

Table 6.2 presents the magnitudes of the constants specific to PE4. The CJ state behaviour of the explosive was simulated with the Material High Explosive Burn key card, the magnitudes of which are also tabulated in Table 6.2.

Table 6.2: JWL EOS and CJ State Parameters Values [3]

—	**JWL EOS Parameters**							**CJ State Parameters**		
Symbol	A	B	E_0	V_0	R_1	R_2	ω	ρ_0	P_{CJ}	D
Units	GPa	GPa	GPa	—	—	—	—	kg/m^3	GPa	m/s
Magnitude	609.77	12.95	9	1	4.5	1.4	0.25	1601	28	8193

Equation 2.23 shows that the detonation velocity depends on the diameter of an explosive charge [12]. In the context of PE4, no ideal detonation velocity data was available at the time of writing this investigation. Table 6.3 presents the Jones-Wilkins-Lee Equation of State (that is, JWL EOS) parameters of the detonation velocities and compositions of PE4 and two other explosives.

Table 6.3: Comparison of Detonation Velocities with respect to RDX Percentage

Explosive Name	**Composition**	**Detonation Velocity (m/s)**
PE4	88% RDX, 12% Plasticiser [12]	8193 [3]
Cyclotol 77/ 23	77% RDX, 23% TNT [12]	8250 [3]
TNT	Chemically Pure [9]	4930 [3]

Cooper [12] reported that Cyclotol 77/23 was the closest explosive to PE4 in terms of RDX percentage. The detonation velocity of TNT was added for comparative purposes. No JWL EOS data available for RDX at the time of writing this dissertation. The detonation velocities of PE4 and Cyclotol only differ by 0.7%, which is insignificant. Thus, it was assumed that the difference in RDX percentage did not affect the detonation velocity.

Ideal detonation velocity data for Cyclotol 77/23 was not available when this investigation was conducted. Therefore, Cyclotol 75/25 (that is, 75% RDX, and 25% TNT) was chosen to approximate the ideal

detonation velocity behaviour of PE4 at the diameters of interest. Figure 6.2 presents the detonation velocity curve for Cyclotol 75/25, where the ideal detonation velocity (D_∞) is 8298 m/s and the constant (W) is 0.139 mm^2/s [12].

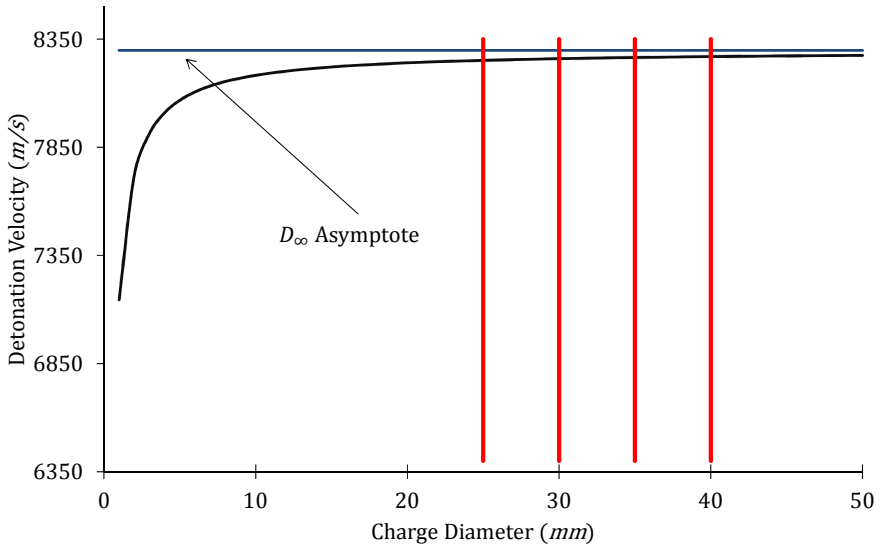

Figure 6.2: Detonation Velocity of Cyclotol 75/25 with Respect to Charge Diameter [12]

The red lines represent the charge diameters of interest (that is, 25, 30, 35, and 40 mm). The detonation velocities at 25 and 40mm are 8252 m/s, and 8269m/s, respectively. The 0.21% difference was insignificant so it is assumed that the detonation velocity of PE4 would not change. It was also assumed that failure to detonate would not occur at the charge diameters of interest, because the critical diameter of PE4 was between 3.81 and 5.08 mm [12].

Air Material and Equation of State

The linear polynomial EOS, which is given by Equation 6.3 [42], was used to simulate the air.

$$P = C_0 + C_1\mu + C_2 + \mu^2 + C_3\mu^3 + \left(C_4 + C_5\mu + C_6\mu^2\right) E_0 \tag{6.3}$$

Where P is the pressure, C_0 to C_6 are polynomial coefficients, E_0 is the initial internal energy per unit reference volume, and μ is a volumetric parameter. The volumetric parameter is related to the reciprocal of the relative volume by Equation 6.4 [42].

$$\mu = \frac{1}{v_r} - 1 = \frac{\rho}{\rho_0} - 1 \tag{6.4}$$

The gamma law EOS was used to model the air. Therefore: $C_0 = C_1 = C_2 = C_3 = C_4 = C_6 = 0$, and $C_4 = C_5 = \gamma - 1$. Where γ is the ratio of the isobaric specific heat to the isochoric specific heat. The linear polynomial EOS was simplified to Equation 6.5 [42].

$$P = (\gamma - 1)\,\frac{\rho}{\rho_0} E_0 \tag{6.5}$$

Where ρ is the instantaneous density of the air in the simulation. The Material Null key card was used to define the air material. The linear polynomial EOS and material constants are presented in Table 6.4.

Table 6.4: Parameters Used to Capture Air Behaviour [4]

—	**Linear Polynomial EOS**					**Material Null**
Symbol	γ	C_4	C_5	E_0	V_0	ρ_0
Units	—	—	—	bar	—	kg/m^3
Magnitude	1.4	0.4	0.4	2.5	1	1.293

6.1.3 Simulated Impulse Calculation Methodology

Pressure histories of the air elements that were adjacent to the reflective boundary were recorded and stored in an ELOUT file. A schematic of these elements is depicted in Figure 6.3.

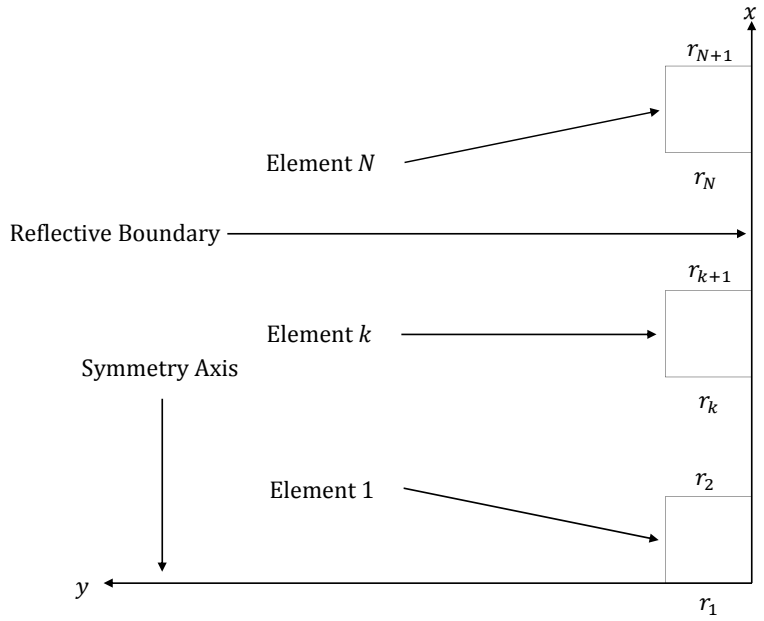

Figure 6.3: Schematic of Elements at the Reflective Boundary Used to Record Pressure Histories

The recording time step of the pressure histories for the elements was defined using the database ascii option key card (DEFAULT DT $= 4e-4$ for ELOUT). The simulated impulse with respect to time was calculated using the Trapezoidal Rule integration scheme. The pressure histories of each element (that is, Pressure in the ELOUT file) was organised into an MxN matrix. Where M is the total number of time based plots for each tracer point's pressure history, and N is the total number of tracer points, as depicted by the matrix of Equation 6.6.

$$\text{Pressure-time history} = \left(\begin{array}{c|ccccc} — & \text{El. } 1 & ... & \text{El. } k & ... & \text{El. } N \\ \hline t_1 & P_{1,1} & ... & P_{1,k} & ... & P_{1,N} \\ ... & ... & ... & ... & ... & ... \\ t_j & P_{1,j} & ... & P_{j,k} & ... & P_{j,N} \\ ... & ... & ... & ... & ... & ... \\ t_M & P_{M,1} & ... & P_{M,k} & ... & P_{M,N} \end{array}\right) \tag{6.6}$$

Where t_j is the j^{th} time step, and $P_{j,k}$ is the pressure in the k^{th} element at the j^{th} time step. A matrix of radii and areas, that corresponded to the elements of interest, was defined. Where $N+1$ radii values were defined and used to calculate N areas. The radii and areas are depicted in the matrix of Equation 6.7

$$\text{Element radii and areas} = \left(\begin{array}{c|ccccc} — & \text{El. } 1 & ... & \text{El. } k & ... & \text{El. } N \\ \hline \text{Inner Radius} & r_1 & ... & r_k & ... & r_N \\ \text{Outer Radius} & r_2 & ... & r_{k+1} & ... & r_{N+1} \\ \text{Area} & A_1 & ... & A_k & ... & A_N \end{array}\right) \tag{6.7}$$

The total force and averaged pressure on the reflective boundary with respect to time was calculated using Equation 6.8. The reference value, P_{ref} was subtracted because it was the pressure that applied no external force to the relective boundary.

$$(t_j, F_j) = \left(t_j, \sum_{k=1}^{N} F_{j,k}\right) = \left(t_j, \sum_{k=1}^{N} \left[P_{j,k} - P_{ref}\right] A_k\right) \quad , \quad (t_j, P_j) = \left(t_j, \frac{F_j}{\pi\left[r_{N+1}^2 - r_1^2\right]}\right) \tag{6.8}$$

The total impulse that was transferred to the reflective boundary with respect to time was calculated using the Trapezoidal integration scheme, as presented by Equation 6.9.

$$(t_j, I_j) = \left(t_j, \sum_{k=1}^{N} \frac{\left(F_{j,k} + F_{j-1,k}\right)\left(t_j - t_{j-1}\right)}{2}\right) \tag{6.9}$$

The force-time history was integrated to plot the cumulative impulse-time history. The value at the simulated time was taken to be the impulse that was transferred to the reflective boundary.

6.1.4 Richardson Extrapolation

As the element size decreased, the simulated impulse data converged to some asymptote. The Richardson Extrapolation technique, as presented by Roache [43], was used and a MATLAB code was written and implemented (refer to Appendix C.3). Three numerical solutions of the simulated impulses (that is, f_1, f_2, and f_3), and their respective element sizes (that is, h_3, h_2, and h_1), were entered into the code. The grid refinements were calculated using Equation 6.10.

$$r_{12} = \frac{h_2}{h_1} \qquad r_{23} = \frac{h_3}{h_2} \tag{6.10}$$

The differences in the numerical solutions were calculated using Equation 6.11.

$$\epsilon_{12} = f_2 - f_1 \qquad \epsilon_{23} = f_3 - f_2 \tag{6.11}$$

The extrapolated asymptotes were calculated using Equation 6.12.

$$f_{12}^{extrap.} = f_1 + \frac{(f_1 - f_2)}{(r_{12}^p - 1)} \qquad f_{23}^{extrap.} = f_2 + \frac{(f_2 - f_3)}{(r_{23}^p - 1)} \tag{6.12}$$

Where p is the converged order of accuracy, which was calculated using Equation 6.13. The first step value of p was equal to 2, because second order accuracy was assumed.

$$p_{12}(i+1) = \omega p_{12}(i) + (1-\omega)\frac{ln[\beta_{12}(i)]}{ln[r_{12}]} \qquad p_{23}(i+1) = \omega p_{23}(i) + (1-\omega)\frac{ln[\beta_{23}(i)]}{ln[r_{23}]} \tag{6.13}$$

Where $\beta(i)$ is a value that was calculated using Equation 6.14.

$$\beta_{12}(i) = \frac{\left(r_{12}^{p_{12}(i)} - 1\right)\epsilon_{23}}{\left(r_{23}^{p_{12}(i)} - 1\right)\epsilon_{12}} \quad \beta_{23}(i) = \frac{\left(r_{12}^{p_{23}(i)} - 1\right)\epsilon_{23}}{\left(r_{23}^{p_{23}(i)} - 1\right)\epsilon_{12}} \tag{6.14}$$

If the grid refinement ratios were identical, the extrapolated asymptotes were the same $f_{12}^{extrap.} = f_{23}^{extrap.}$. The extrapolated asymptotes were used as the benchmark against which the accuracies of the numerical solutions were measured.

6.1.5 Air Mesh Sensitivity Results

Table 6.5 presents the ALE mesh sensitivity results, the percentage accuracies of which are in brackets.

Table 6.5: ALE Mesh Sensitity Test Results

h (mm)	dt_{min} (ms)	**ALE Nodes**	**Time** (hr)	**Impulse** (Ns)
2	40e-5	15276	0.05	24.23 (85.59 % Accurate)
1	20e-5	60551	0.36	26.41 (93.29 % Accurate)
0.5	10e-5	241101	2.43	27.42 (96.88 % Accurate)
0	0	∞	—	28.31

The 2 mm impulse is within 15% of the extrapolated asymotote. Halving the 2 mm element size put the impulse to within 7% of the extrapolated asymptote, and increased the computation time from 3 min to 24 min. A further halving the of the element size to 0.5 mm put the impulse to within 4% of the extrapolated impulse, and increased the computation time from 24 min to more than 2 hours. For an ALE mesh domain of this size, the drop in error was not worth the extra computation cost, therefore, the 1 mm ALE element mesh was chosen.

6.2 Cylinder Mesh Sensitivity Study

6.2.1 General

Shell Elements with a Shell Section

A cylinder with bilinear square elements was added to the ALE mesh, as depicted in green in Figure 6.4. The cylinder had a shell section with an axisymmetric area weighted element formulation (ELFORM = 14) and a Lagrangian solid element type (SETYP = 1).

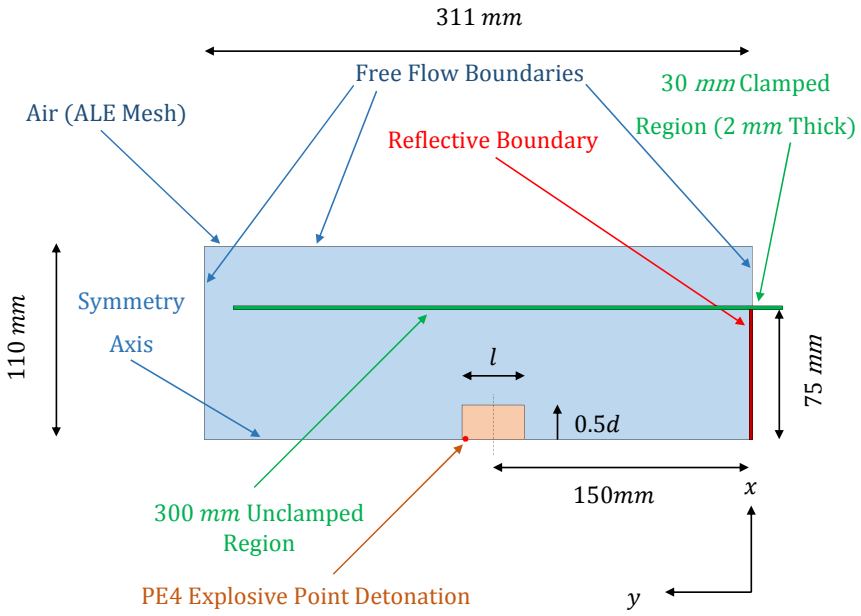

Figure 6.4: Schematic of the Simulated Blast Model Domain

The simulated material was assumed to be isotropic. To scale the transverse shear stresses, the recommended shear correction factor (SHRF = 0.8333333) for isotropic materials was used [42]. One through thickness integration point (NIP = 1) was used because the elements were two dimensional [41].

Boundary Condition (SPC Set)

The clamp was simulated with a 30 mm long part of the simulated cylinder. All nodes at the clamp were translationally constrained in the x direction. No constraints were applied to the unclamped region of the simulated cylinder.

6.2.2 Simulated Cylinder

Material Model

The material behaviour of the 304 stainless steel was captured with the Johnson-Cook material model, as described by Equation 6.15 [42].

$$\sigma_{flow} = \left[A + B\epsilon_{plastic}^{n}\right]\left[1 + c\,ln\left(\frac{\dot{\epsilon}}{\dot{\epsilon}_0}\right)\right]\left[1 - \left(\frac{T - T_r}{T_m - T_r}\right)^{m}\right] \tag{6.15}$$

Where A is the yield strength, B is the strength coefficient, n is the strain hardening exponent, c is a strain rate fitting parameter, $\dot{\epsilon}$ is the instantaneous strain rate in the simulation, $\dot{\epsilon}_0$ is the strain rate at which quasi-static tensile testing was done to characterise the stainless steel, T is the instantaneous temperature in the simulation, T_r is the initial reference/ room temperature, T_m is the melting temperature, and m is a thermal softening fitting parameter. Table 6.6 presents the Johnson-Cook parameters and other material properties.

Table 6.6: Johnson-Cook Parameters [5, 6, 7] and Other Material Properties

Symbol	ρ_0	G	E	ν	A	B
Units	kg/m^3	GPa	GPa	—	MPa	MPa
Magnitude	7900	77	200	0.3	280.98^a	1319.95^a
Symbol	n	T_m	T_r	$\dot{\epsilon}_0$	c, m	c_p
Units	—	K	K	$1/s$	—	$J/\left(kgK\right)$
Magnitude	0.86^a	1673	293	0.001^a	0.07, 0.9	440
^{a} Values for A, B, n, and $\dot{\epsilon}_0$ from Material Characterisation, Chapter 5						

Equation of State

Solid elements were used with the Johnson-Cook material model. In this case, LS DYNA requires that the cylinder material have an EOS [42] or the simulations would not run. The Grüneisen EOS, as described by Equation 6.16, was used to capture the state behaviour of the 304 stainless steel.

$$P = \frac{\rho_0 C^2 \mu\left[1 + \left(1 - \frac{\gamma_0}{2}\right)\mu - \frac{a\mu^2}{2}\right]}{\left[1 - \left(S_1 - 1\right)\mu - \frac{S_2\mu^2}{\mu+1} - \frac{S_3\mu^3}{(\mu+1)^2}\right]^2} + \left(\gamma_0 + a\mu\right)E \tag{6.16}$$

Where C is the intercept of the Grüneisen Hugoniot described by Equation 6.17 [5], and S_1 to S_3 are constants that describe the instantaneous rate of change in the same equation, and E is the initial internal energy.

$$v_s = C + S_1 v_p + S_2\left(\frac{v_p}{v_s}\right)v_p + S_3\left(\frac{v_p}{v_s}\right)^2 v_p \tag{6.17}$$

Where v_s and v_p are the particle and shock velocities, respectively. The initial Grüneisen gamma, γ_0, is used to calculate the instantaneous Grüneisen gamma described by Equation 6.18, and a is a first order correction to the instantaneous Grüneisen gamma [5].

$$\gamma = \frac{\gamma_0 + a\mu}{1 + \mu} \tag{6.18}$$

For expanding materials (that is, $\mu < 0$), Equation 6.19 applies [5, 42].

$$P = \rho_0 C^2 \mu + (\gamma_0 + a\mu)\, E \tag{6.19}$$

Table 6.7 presents the magnitudes of the constants that were used for the Grüneisen EOS.

Table 6.7: Grüneisen EOS Values [5]

Symbol	C	S_1	S_2	S_3	γ_0	a	E	V_0
Units	m/s	—	—	—	—	—	J	—
Magnitude	4570	1.49	0	0	1.93	0.5	0	1

Fluid Structure Interaction (Constrained Lagrange in Solid)

The constrained Lagrange in solid key card was used to simulate the fluid structure interaction of the air/ PE4 mixture with the cylinder. The Lagrange mesh was the appointed as a slave, and the air/ PE4 mixture was appointed as the master. A coupling point was placed over each Lagrangian element surface that faced the air/ PE4 mixture (NQUAD = 1) to prevent leakage and instabilities (caused by too many coupling points). Coupling was active in the normal direction with compression only (DIREC = 2), strong coupling leakage control (ILEAK = 2) was active, and the leakage control penalty factor was at the recommended minimum (PLEAK = 0.1) [41].

To further ensure that neither the air nor the PE4 leaked seperately, two such cards were created. The first key cards multi material option was the air multi material group, and the second key cards multi material option was the PE4 multi material group.

Diametric Deflection (Database Ascii Option and History Node Set) and Cylinder Profile

The nodes of the outer face of the cylinder were grouped as a node set, and imported into the History Node Set key card. The recording time step of the node histories was defined using the Dabatase Ascii Option key card (DEFAULT DT = $4e-4$ for NODOUT). Ozinsky *et al.* [22, 23] calculated the simulated radial midpoint deflection from an equilibrium point to the simulated time. This method was used by the author [22, 23] for one node per simulated cylinder. Finding the equilibrium point for all transient x and y displacements at each node, for this dissertation, would have been tedious. Therefore, another method was developed, written, and implemented in MATLAB (refer to Appendix C.2).

The transient coordinates (that is, X-Coord and Y-Coord in the NODOUT file) were simultaneously exported as a matrix, as depicted by Equation 6.20. Note that the x displacements were in the radial direction and the y displacements were in the axial direction.

$$\text{Displacement-time history} = \left(\begin{array}{c|cccccc|cccccc} — & x_1 & \dots & x_j & \dots & x_N & y_1 & \dots & y_j & \dots & y_N \\ \hline t_1 & x_{1,1} & \dots & x_{1,j} & \dots & x_{1,N} & y_{1,1} & \dots & y_{1,j} & \dots & y_{1,N} \\ \dots & \dots & \dots & \dots & \dots & \dots & \dots & \dots & \dots & \dots & \dots \\ t_i & x_{i,1} & \dots & x_{i,j} & \dots & x_{i,N} & y_{i,1} & \dots & y_{i,j} & \dots & y_{i,N} \\ \dots & \dots & \dots & \dots & \dots & \dots & \dots & \dots & \dots & \dots & \dots \\ t_M & x_{M,1} & \dots & x_{M,j} & \dots & x_{M,N} & y_{M,1} & \dots & y_{M,j} & \dots & y_{M,N} \end{array}\right) \tag{6.20}$$

Where M is the number of timesteps, N is the number of nodes, and $(x_{i,j}, y_{i,j})$ are the coordinates of the j^{th} node at the i^{th} timestep. A matrix, X, was initialised and populated with the transient x values of each node, and a matrix, Y, was initialised and populated with the transient y values of each node. An Nx2 matrix, A, was initialised, where the first column contained the averaged x values of each node, and the second column contained the averaged y values of each node. Each node coordinate was averaged from $0.5t_M \rightarrow t_M$, as described by Equation 6.21.

$$(x_j^{average}, y_j^{average}) = (A_{1,j}, A_{2,j}) = \left(\sum_{i=0.5M}^{M} X_{i,j}, \sum_{i=0.5M}^{M} X_{i,j} \right) \tag{6.21}$$

Figure 6.5 depicts a typical x and y coordinate history of a node at the outer face of the simulated cylinder. The x and y values from half the simulated time (that is, the thick black line) to the simulated time converged. Note that the increase in x displacment implies outward radial deflection, and the decrease in y displacement implies axial shortening.

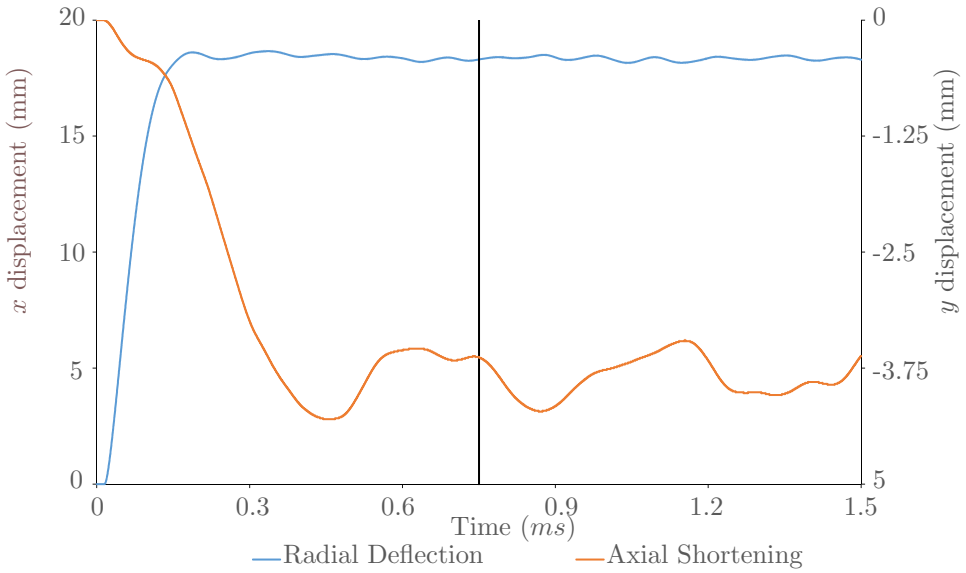

Figure 6.5: Typical Displacement-Time Graph of a Node on Outer Radius of the Cylinder

6.2.3 Cylinder Mesh Sensitivity Results

Table 6.8 presents the results of the Lagrangian mesh sensitivity test where a 1 mm ALE mesh was used. The deflection column presents the maximum diametric deflection of the simulated cylinder. Note that the simulated time was 2 ms. The accuracies of the deflections, relative to the extrapolated asymptote, are bracketed.

Table 6.8: ALE and Lagrangian Mesh Sensitivity Results

h (mm)	dt_{min} (ms)	**Lagrange Nodes**	**Time** (hr)	**Deflection** (mm)
1	20e-5	993	2.85	36.70 (96.22% Accurate)
0.5	10e-5	3305	3.83	37.42 (98.11% Accurate)
0.25	5e-5	11889	9.57	37.78 (99.06% Accurate)
0	0	∞	—	38.14

The error of the 1 mm mesh deflection is just under 4%. Halving the 1 mm Lagrange element increased the computation cost by about 34%, yet decreased the error of the deflection by about 1.89%. Decreasing the mesh to 0.5 mm caused a 2.5 fold increase to the computation cost, and an error drop of about 0.95%. The 1 and 0.5 mm Lagrange element meshes stood out in terms of computation cost and accuracy, however, the computation time of the finest mesh was still feasible. Thus, the 0.25 mm mesh was chosen.

7

Numerical Simulation Results

This chapter presents the results of the simulated experiments, a comparison of the simulated data and experimental data sets, and a discussion thereof.

7.1 Tabulated Data

Table 7.1 presents the simulated results. The "**Charge**" column presents the charge specifications, the "m" column groups the simulated charges by mass, the "d" column groups the simulated charges by diameter, the "**Imp.**" column presents the simulated axial impulses that were transferred to the reflective boundary, the "**Max. Defl.**" presents the maximum diametric deflections of each simulated cylinder, the "**Short.**" column presents the axial shortening of each simulated simulated cylinder, and the "P_{max}" column presents the simulated average peak pressure at the reflective boundary.

The ruptured cylinder tests were not simulated, therefore these charges were not discussed further.

Table 7.1: Tabulated Simulated Results

Charge	m	d	**Impulse** (Ns)	**Max. Defl.** (mm)	**Short.** (mm)	P_{max} (MPa)
m Markers: 20 (♣), 24 (✿), 27 (➲) 31 (❣), 34 (✜), 43 (✄), 48 (▼), 49 (✌), 54 (✖) g Charges						
d Markers: 25 (ȣ), 30 (✷—), 35 (△), and 40 (**T**) mm Diameter Charges						
10g_25d_0.5		ȣ	23.71	1.22	0.37	19.29
12g_25d_0.6		ȣ	26.73	1.99	0.44	20.10
14g_25d_0.7		ȣ	31.30	3.18	0.26	22.31
16g_25d_0.8		ȣ	34.28	4.75	0.62	24.00
18g_25d_0.9		ȣ	38.74	6.86	0.88	25.40
20g_25d_1	♣	ȣ	42.04	9.10	1.45	27.94
24g_25d_1.2	✿	ȣ	49.95	13.06	2.06	32.19
31g_25d_1.6	❣	ȣ	65.21	21.75	4.31	32.99
43g_25d_2.2	✄	ȣ	86.06	35.76	8.95	36.21
49g_25d_2.5	✌	ȣ	97.67	41.13	10.31	40.64
59g_25d_3		ȣ	Ruptured Tube Not Simulated			
17g_30d_0.5		✷—	37.52	3.08	0.37	37.98
20g_30d_0.6	♣	✷—	44.31	5.92	1.02	41.22
24g_30d_0.7	✿	✷—	51.01	9.18	1.54	47.05
27g_30d_0.8	➲	✷—	57.92	12.56	2.23	47.78
31g_30d_0.9	❣	✷—	64.33	16.13	3.18	53.64
34g_30d_1	✜	✷—	70.74	20.35	4.28	58.66
48g_30d_1.4	▼	✷—	96.68	34.89	8.70	65.60
54g_30d_1.6	✖	✷—	109.30	42.83	12.88	66.11
27g_35d_0.5	➲	△	60.74	8.80	1.71	71.13
32g_35d_0.6		△	69.35	12.34	2.44	79.49
38g_35d_0.7		△	81.20	19.16	4.68	85.33
43g_35d_0.8	✄	△	90.22	24.47	6.25	87.00
49g_35d_0.9	✌	△	101.84	30.89	8.59	94.11
54g_35d_1	✖	△	110.01	34.72	9.57	101.41
59g_35d_1.1		△	121.58	41.36	13.20	104.24
65g_35d_1.2		△	Ruptured Tube Not Simulated			
40g_40d_0.5		**T**	86.50	15.10	3.81	114.34
48g_40d_0.6	▼	**T**	102.38	22.64	6.54	123.11
56g_40d_0.7		**T**	117.81	30.45	10.09	129.13
64g_40d_0.8		**T**	134.07	37.78	13.89	139.77
72g_40d_0.9		**T**	Ruptured Tube Not Simulated			

7.2 Cylinder Profile

7.2.1 Node Plots

The deflection profiles obtained from the simulations are shown in Figures 7.1 to 7.4 for the 25, 30, 35, and 40 mm diameter charges, respectively. The node plots show that the deformation is highly localised at the charge location (that is, the primary bulge).

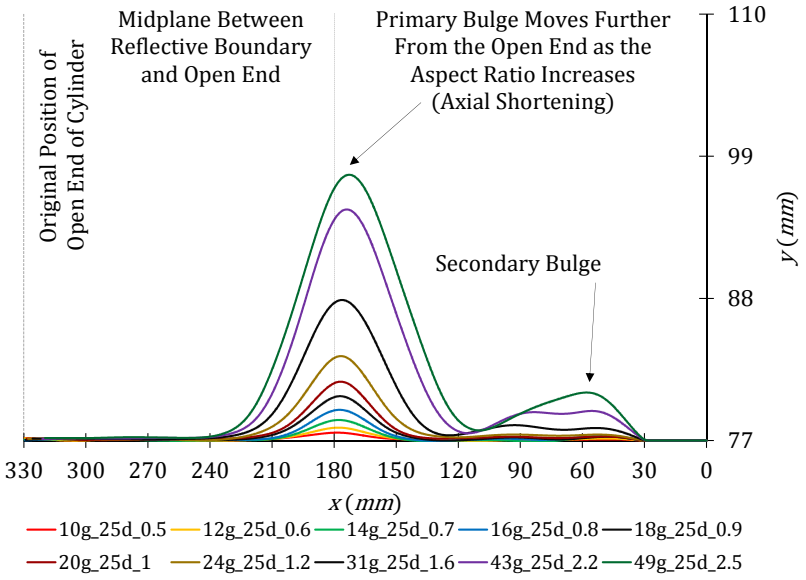

Figure 7.1: Simulated Profiles of Cylinders Loaded by 25 mm Diameter Charges

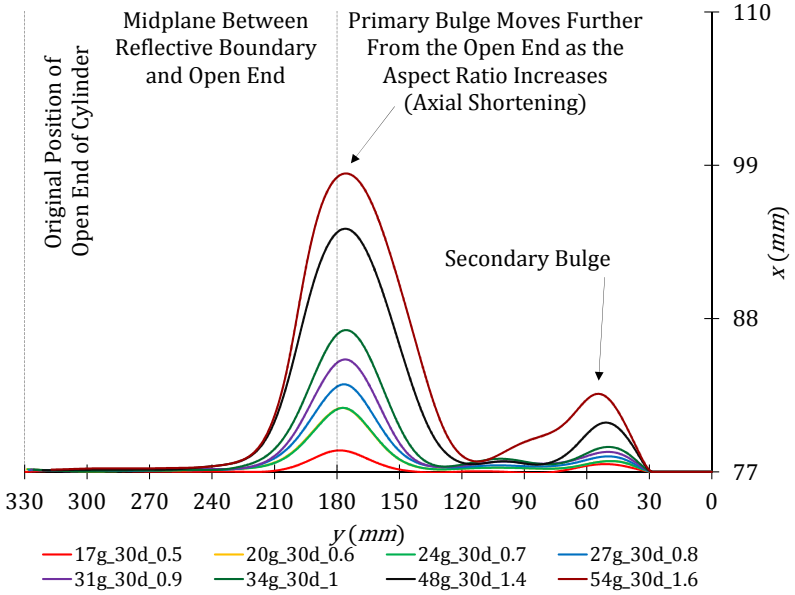

Figure 7.2: Simulated Profiles of Cylinders Loaded by 30 mm Diameter Charges

The node plots also show that as the aspect ratio of the charges increases, the primary bulge peaks move further from the midplane between the reflective boundary and open end. This correlates with a higher maximum diametric deflection leading to a greater quantity of axial shortening. As the aspect ratio increases, the deformation becomes localised at the clamped region (that is, the secondary bulge).

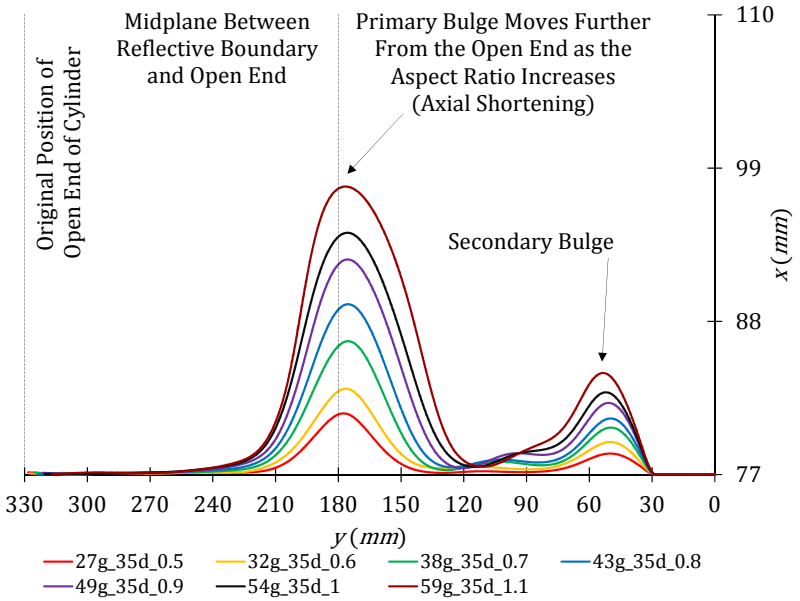

Figure 7.3: Simulated Profiles of Cylinders Loaded by 35 mm Diameter Charges

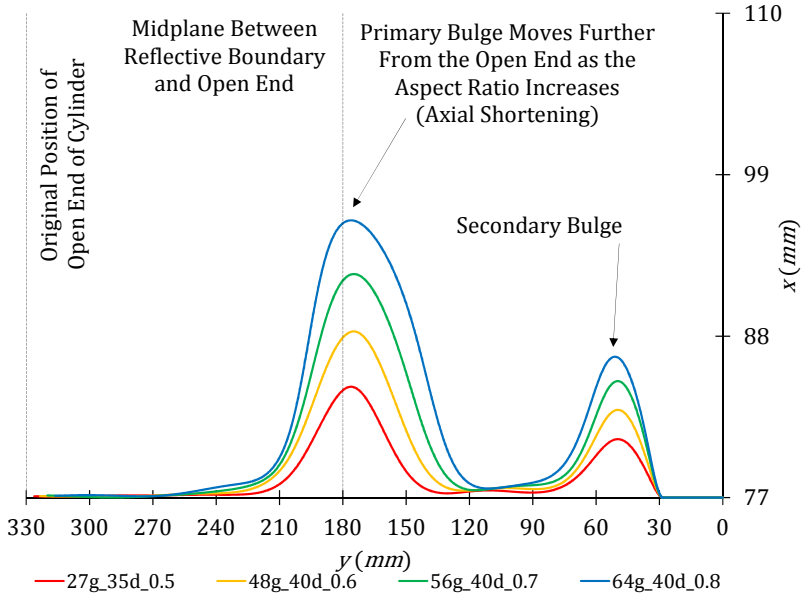

Figure 7.4: Simulated Profiles of Cylinders Loaded by 40 mm Diameter Charges

7.2.2 Maximum Diametric Deflection

Figure 7.5 depicts the simulated maximum diametric deflections with respect to aspect ratio, where the diameter and mass were kept constant. The experimental maximum diametric deflections were plotted on the same graphs for comparitive purposes.

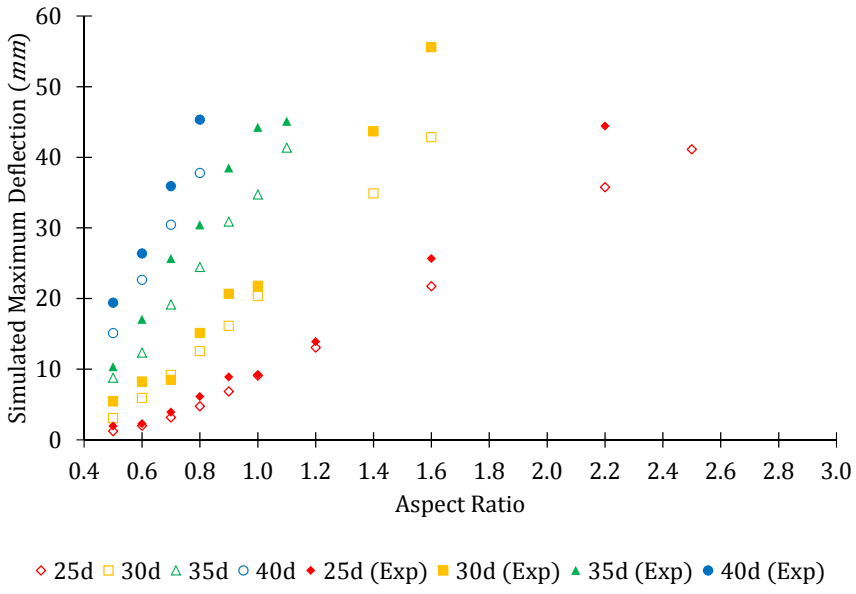

(a) Constant Diameter

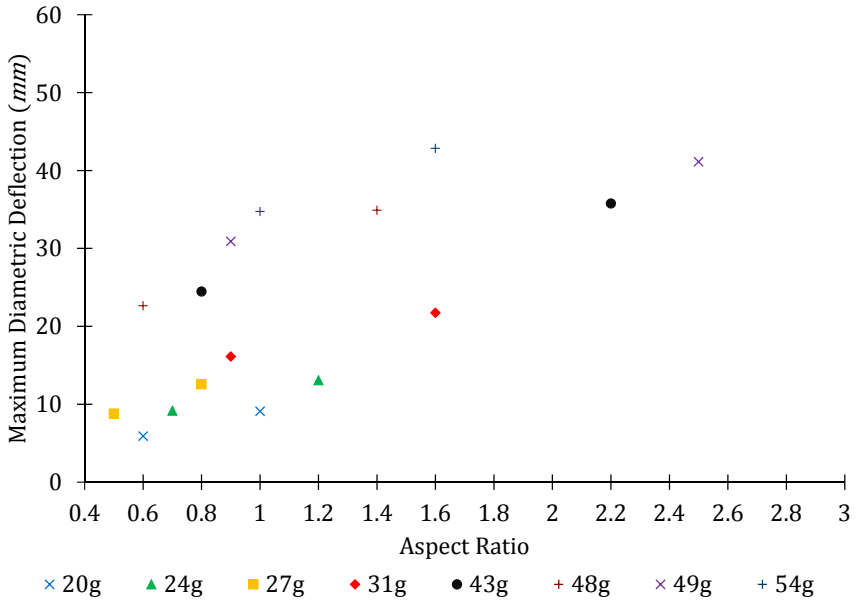

(b) Constant Mass

Figure 7.5: Maximum Diametric Deflections (Simulated)

Constant Diameter Trends and Correlation

Figure 7.5(a) depicts the effect of aspect ratio on the simulated maximum deflection, where the diameter was kept constant. For each diameter, the simulated maximum diametric deflection is directly proportional to the aspect ratio, which corresponds to the primary bulges that are depicted on the simulated cylinder profiles of Figure 7.1, 7.2, 7.3, and 7.4.

Table 7.2 presents a comparison of the experimental and simulated maximum diametric deflections. The "**Exp.**" column presents the experimental magnitude, the "**Sim.**" column presents the simulated magnitude, and the ("**Diff.**" column) presents the difference between the two in mm and cylinder wall thicknesses.

Table 7.2: Comparison of Simulated and Experimental Maximum Diametric Deflections

Charge	m	d	m_{eff}^{side} (g)	**Exp.** (mm)	**Sim.** (mm)	**Diff.** (mm)	**Diff. (Thk.)**
m Markers: 20 (♣), 24 (✿), 27 (➲) 31 (❣), 34 (✜), 43 (✂), 48 (▼), 49 (✌), 54 (✖) g Charges							
d Markers: 25 (ȣ), 30 (✷—), 35 (△), and 40 (**T**) mm Diameter Charges							
10g_25d_0.5		ȣ	4.757	1.95	1.22	0.73	0.37
12g_25d_0.6		ȣ	6.493	2.30	1.99	0.31	0.15
14g_25d_0.7		ȣ	8.368	3.93	3.18	0.75	0.38
16g_25d_0.8		ȣ	10.331	6.11	4.75	1.36	0.68
18g_25d_0.9		ȣ	12.328	8.91	6.86	2.04	1.02
20g_25d_1	♣	ȣ	14.328	9.22	9.10	0.12	0.06
24g_25d_1.2	✿	ȣ	18.328	13.89	13.06	0.83	0.41
31g_25d_1.6	❣	ȣ	25.328	25.67	21.75	3.92	1.96
43g_25d_2.2	✂	ȣ	37.328	44.41	35.76	8.65	4.32
49g_25d_2.5	✌	ȣ	43.328	53.59	41.13	12.46	6.23
17g_30d_0.5		✷—	7.939	5.42	3.08	2.34	1.17
20g_30d_0.6	♣	✷—	10.483	8.26	5.92	2.34	1.17
24g_30d_0.7	✿	✷—	14.268	8.48	9.18	-0.70	-0.35
27g_30d_0.8	➲	✷—	17.204	15.11	12.56	2.55	1.28
31g_30d_0.9	❣	✷—	21.199	20.65	16.13	4.52	2.26
34g_30d_1	✜	✷—	24.199	21.80	20.35	1.45	0.73
48g_30d_1.4	▼	✷—	38.199	43.66	34.89	8.77	4.38
54g_30d_1.6	✖	✷—	44.199	55.58	42.83	12.75	6.38
27g_35d_0.5	➲	△	12.612	10.34	8.80	1.54	0.77
32g_35d_0.6		△	16.888	17.05	12.34	4.70	2.35
38g_35d_0.7		△	22.547	25.66	19.16	6.50	3.25
43g_35d_0.8	✂	△	27.444	30.44	24.47	5.97	2.99
49g_35d_0.9	✌	△	33.437	38.48	30.89	7.59	3.79
54g_35d_1	✖	△	38.437	44.24	34.72	9.51	4.76
59g_35d_1.1		△	43.437	45.08	41.36	3.73	1.86
40g_40d_0.5		**T**	18.523	19.41	15.10	4.30	2.15
48g_40d_0.6	▼	**T**	25.442	26.38	22.64	3.73	1.87
56g_40d_0.7		**T**	32.933	35.91	30.45	5.46	2.73
64g_40d_0.8		**T**	40.779	45.33	37.78	7.55	3.78

It was found that the simulated deflections which correlated to 90% repeatability are within ± 1 thickness for plates [10, 25, 44], and ± 2 thicknesses for the diametric deflections of cylinders [22, 23].

Generally, the simulations underpredicted the maximum diametric deflections, more so when it came to the heavier charges. The model predicted 55% of the deflections to within the acceptable 2 cylinder

thicknesses, and 45% of the magnitudes did not correlate. The disparities in the deflections could have been caused by uncertainties in the calibration of the Johnson-Cook material model (especially the strain rate and thermal softening fitting parameters).

Constant Mass Trends, and Side Effective Charge Mass Effects

Similar to Figure 4.5(b), Figure 7.5(b) shows that long charges produced greater diametrical deflections than their mass equivalent shorter charges. The long charges had higher side effective charge masses than the shorter charges, which is observed from the simulation results. The blast wave profiles of two 43 g charges at different time steps, are shown in Figure 7.6, and a legend of pressure for ease of reference.

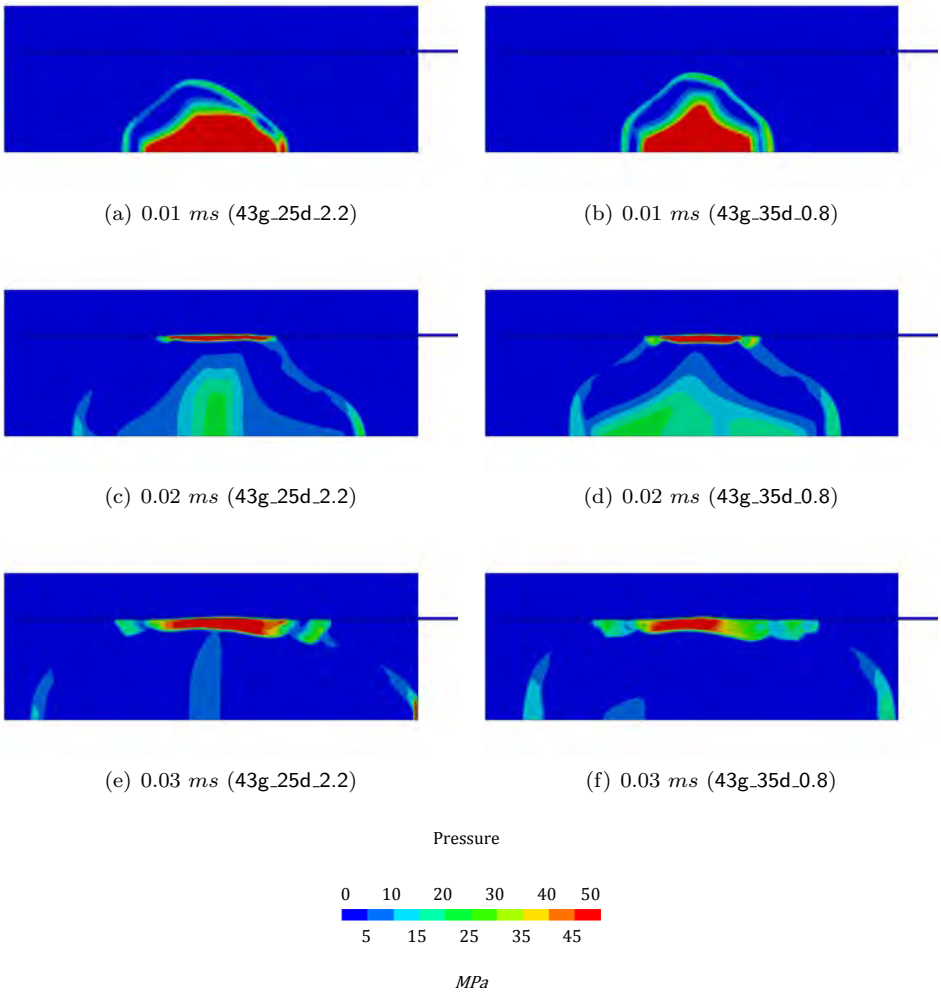

(a) 0.01 ms (43g_25d_2.2) (b) 0.01 ms (43g_35d_0.8)

(c) 0.02 ms (43g_25d_2.2) (d) 0.02 ms (43g_35d_0.8)

(e) 0.03 ms (43g_25d_2.2) (f) 0.03 ms (43g_35d_0.8)

Figure 7.6: Blast Wave Propagation Comparison (43 g Charges)

At 0.01 ms, the blast waves of both charges propagated outward before the cylinder side wall. At 0.02 ms, both blast waves impinged on the cylinder wall, and formed their respective boundary layers. The high pressure zone ($P \geq 50\ MPa$) of the long 43g_25d_2.2 charge covered a greater area than that of the

shorter (43g_35d_0.8) charge. At 0.03 ms, the high pressure zone of the long charge acted over a larger area for a longer period of time and it formed a thicker boundary layer next to the wall.

The plotted data of Figure 7.5(b), like that of Figure 4.5(b), also shows that a lighter charge that is long can cause larger diametric deflections than a heavier charge that is short. Figure 7.7 depicts the blast wave propagation of three charges at different time steps, where the heaviest of these charges caused the least diametric deflection of its simulated cylinder.

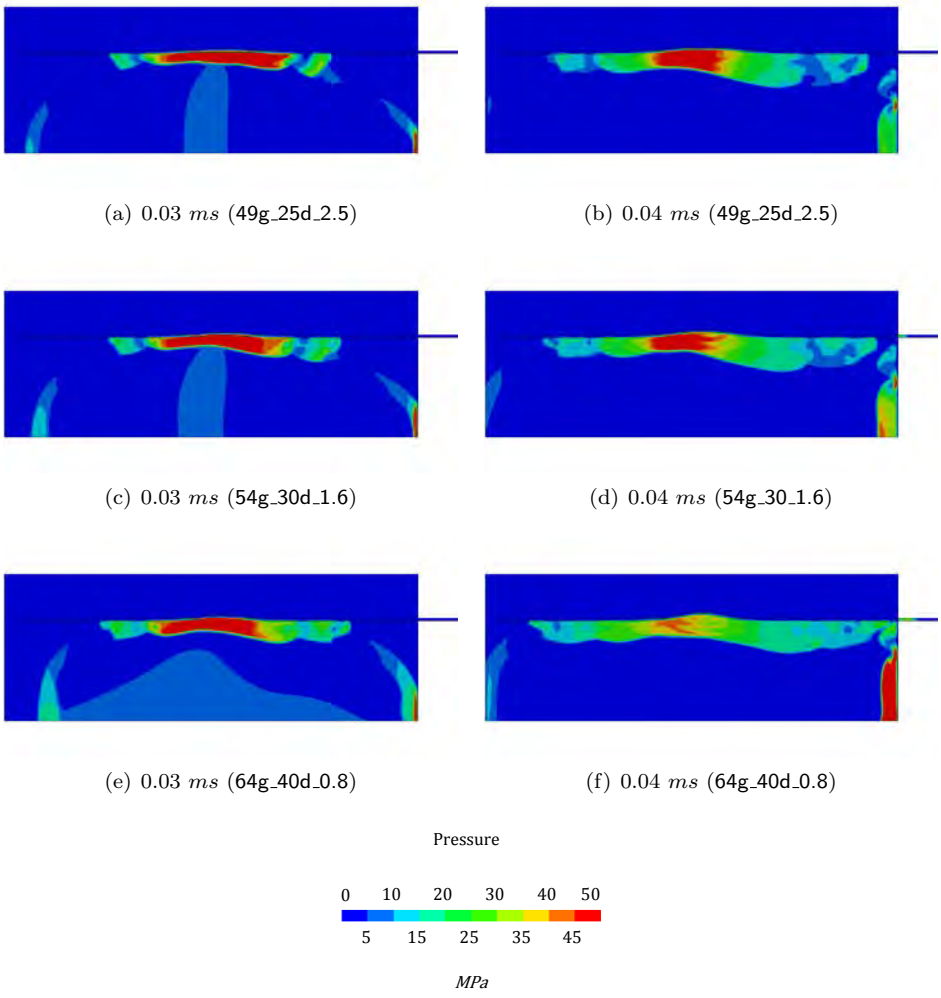

(a) 0.03 ms (49g_25d_2.5) (b) 0.04 ms (49g_25d_2.5)

(c) 0.03 ms (54g_30d_1.6) (d) 0.04 ms (54g_30_1.6)

(e) 0.03 ms (64g_40d_0.8) (f) 0.04 ms (64g_40d_0.8)

Figure 7.7: Blast Wave Propagation (49g, 54g, and 64g Charges)

The high pressure zone of the 64g_40d_0.8 charge at the wall charge did not act over a greater area, nor did it last as long as that of the other charges, because the thickness of the high pressure zone shrank after 0.03 ms. Hence, less impulse was transferred to the wall from its side effective charge mass, so the wall deflected less than the ligher charges. This also applied to the other cases, such as the pairs: 27g_35d_0.5 and 24g_25d_1.2, 48g_40d_0.6 and 43g_35d_0.8.

7.2.3 Axial Shortening and Secondary Bulge Formation

The 64 g, 40 mm diameter charge is used herein as an example of axial shortening and secondary bulge formation, as shown in Figure 7.8.

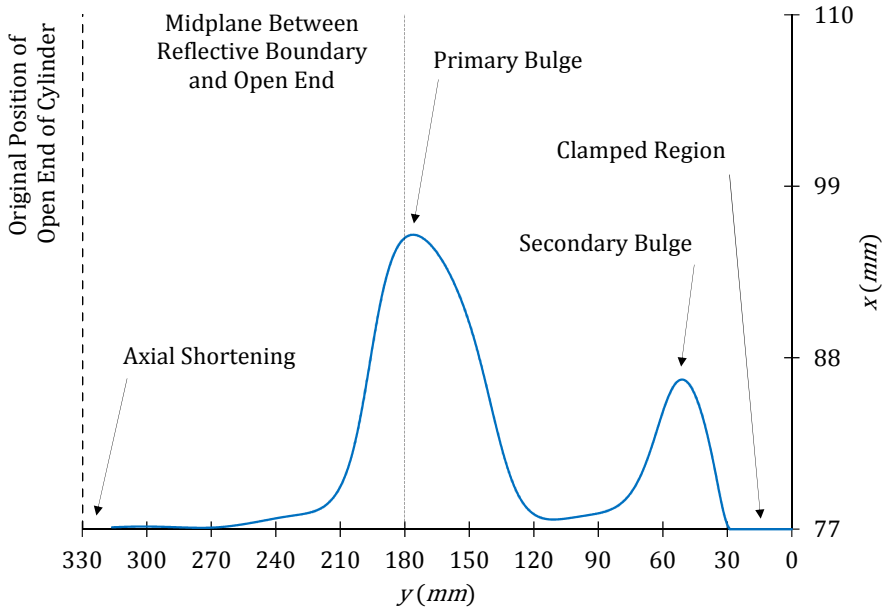

Figure 7.8: Simulated Axial Shortening and Secondary Bulge Formation (64g_40d_0.8 Simulation)

Figure 7.9 depicts the blast wave propagation in the 64g_40d_0.8 simulation. These pressure contour plots continue from Figure 7.7(e) and 7.7(f).

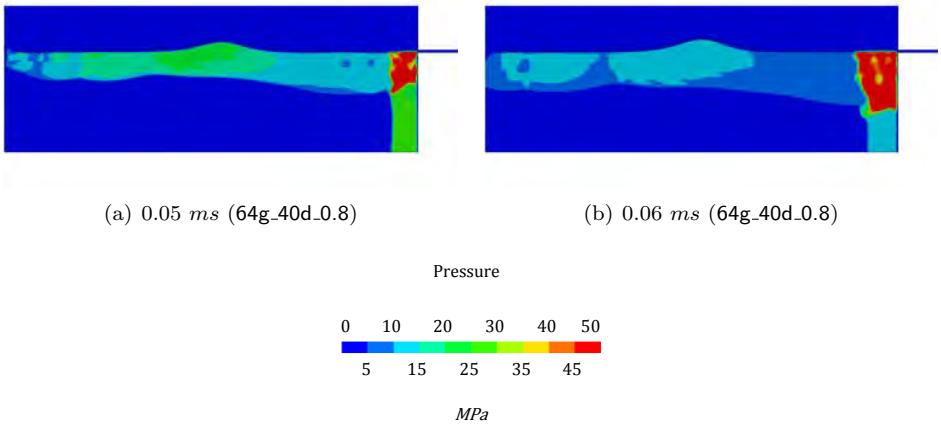

(a) 0.05 ms (64g_40d_0.8) (b) 0.06 ms (64g_40d_0.8)

Figure 7.9: Blast Wave Superposition at the Clamped Region Causing Secondary Bulge Formation

The blast wave pressure impinged on the wall and the reflective boundary at different times. The wave at the wall and reflective boundary changed direction, travelled to the clamped region, and collided. During the collision, the sub-waves superimposed on each other and caused the wall adjacent to the clamp to

move sideways. Figure 7.10 depicts the volume fraction history of the PE4 movement in the cylinder. Note that red represents PE4 and blue represents air.

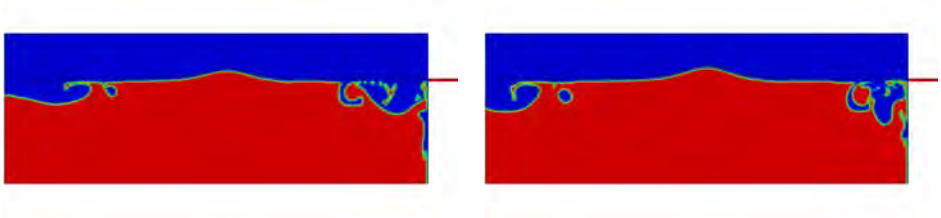

(a) 0.05 ms (64g_40d_0.8) (b) 0.06 ms (64g_40d_0.8)

Figure 7.10: PE4 Propagation During Secondary Bulge Formation

Figure 7.10, when used in conjunction with Figure 7.9, shows that the air/ PE4 interface impinged the reflective boundary and changed direction, while the sub-waves collided and superimposed on each other. Between 0.05 and 0.06 ms, the density of the air/ PE4 interface increased and further contributed to the formation of the secondary bulge. This phenomenon is similar to that observed by Neal *et al.* [36].

Table 7.3 presents a comparison of the simulated and experimental axial shortenings, and the differences between the two in mm and cylinder thicknesses. The model predicted 83% of the axial shortenings to within the acceptable 2 cylinder thicknesses.

Table 7.3: Comparison of Simulated and Experimental Axial Shortenings

Charge	**Exp.**	**Sim.**	**Diff.**		**Charge**	**Exp.**	**Sim.**	**Diff.**	
Axial Shortening Units in mm, Differences in mm and Cylinder Thicknesses									
10g_25d_0.5	0.73	0.20	0.53	0.26	34g_30d_1	4.55	2.26	2.29	1.14
12g_25d_0.6	0.63	0.24	0.39	0.20	48g_30d_1.4	12.92	5.31	7.61	3.80
14g_25d_0.7	0.41	0.36	0.05	0.03	54g_30d_1.6	18.25	5.76	12.49	6.25
16g_25d_0.8	0.68	0.55	0.13	0.07	27g_35d_0.5	1.84	1.25	0.59	0.30
18g_25d_0.9	1.26	0.98	0.28	0.14	32g_35d_0.6	3.49	1.32	2.17	1.08
20g_25d_1	2.08	1.29	0.79	0.39	38g_35d_0.7	6.20	2.73	3.47	1.73
24g_25d_1.2	2.80	1.64	1.16	0.58	43g_35d_0.8	8.72	2.76	5.96	2.98
31g_25d_1.6	5.76	3.23	2.53	1.26	49g_35d_0.9	11.87	4.58	7.29	3.64
43g_25d_2.2	11.70	4.58	7.12	3.56	54g_35d_1	15.05	5.18	9.87	4.93
49g_25d_2.5	16.05	6.35	9.70	4.85	59g_35d_1.1	15.52	2.54	12.98	6.49
17g_30d_0.5	1.05	0.33	0.72	0.36	40g_40d_0.5	5.38	2.37	3.01	1.50
20g_30d_0.6	1.20	0.74	0.46	0.23	48g_40d_0.6	8.55	3.41	5.14	2.57
24g_30d_0.7	2.18	1.32	0.86	0.43	56g_40d_0.7	13.14	4.27	8.87	4.44
27g_30d_0.8	2.77	1.49	1.28	0.64	64g_40d_0.8	18.79	5.93	12.86	6.43
31g_30d_0.9	4.73	1.72	3.01	1.51					

When the diameter was kept constant, the axial shortening increased as the aspect ratio increased. Figure 7.1, 7.2, 7.3, and 7.4, used in conjunction with the tabulated data shows why the axial shortenings increased: the final position of the open end and of the primary bulge peak was closer to the reflective boundary, as the aspect ratio of the charge increased.

7.2.4 Profile Comparison

Figure 7.11 presents graphs that show the simulated and experimental profiles of cylinders that were loaded by 31g_25d_1.6 and 48g_40d_0.6 detonations. These cases were selected because the physical deformation of each cylinder was very close to symmetric, and the maximum deflections and axial shortenings were within the acceptable ± 2 cylinder thicknesses.

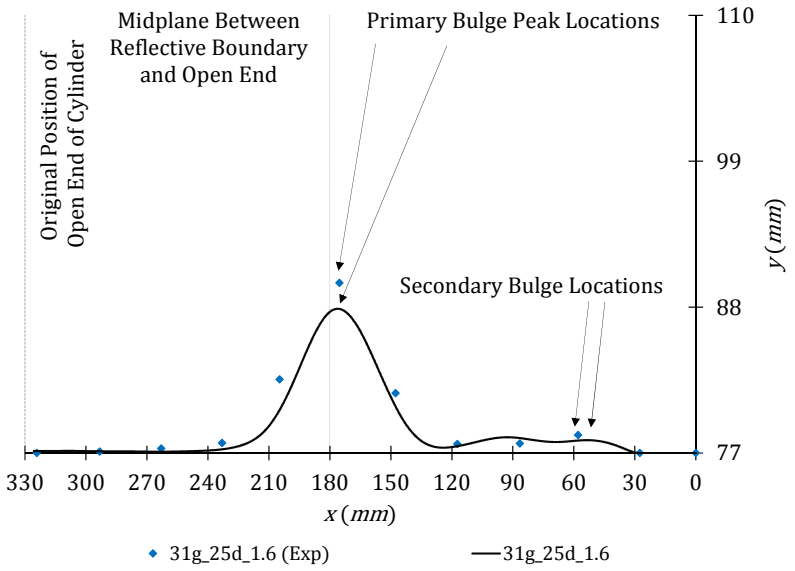

(a) 31g_25d_1.6

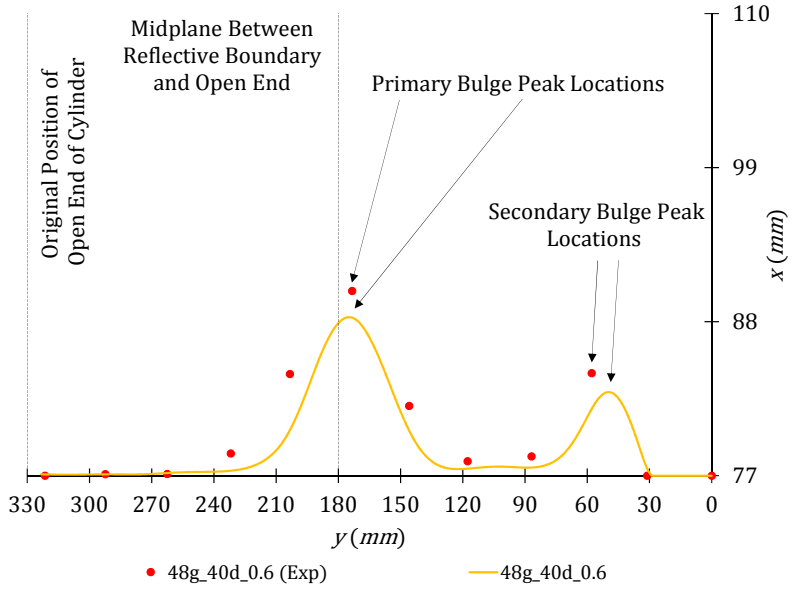

(b) 48g_40d_0.6

Figure 7.11: Graphs Showing the Comparison Between Simulated and Experimental Profiles

The simulated and experimental deflections were highly localised at the charge location, with localised deflections adjacent to the clamped region. The simulated profiles, of both cases, had good agreement

with the experimental measurements in terms of primary and secondary bulge peak position. In the axial direction of both cases, the model generally underpredicted the radial deflections, which could be attributed to the uncertainty in the thermal softening parameter of the Johnson-Cook material model.

7.3 Axial Impulses

7.3.1 Plotted Data

Figure 7.12 depicts the simulated axial impulses (open symbols) with respect to aspect ratio, where the diameter and mass are kept constant. The experimental impulses were added for comparitive purposes.

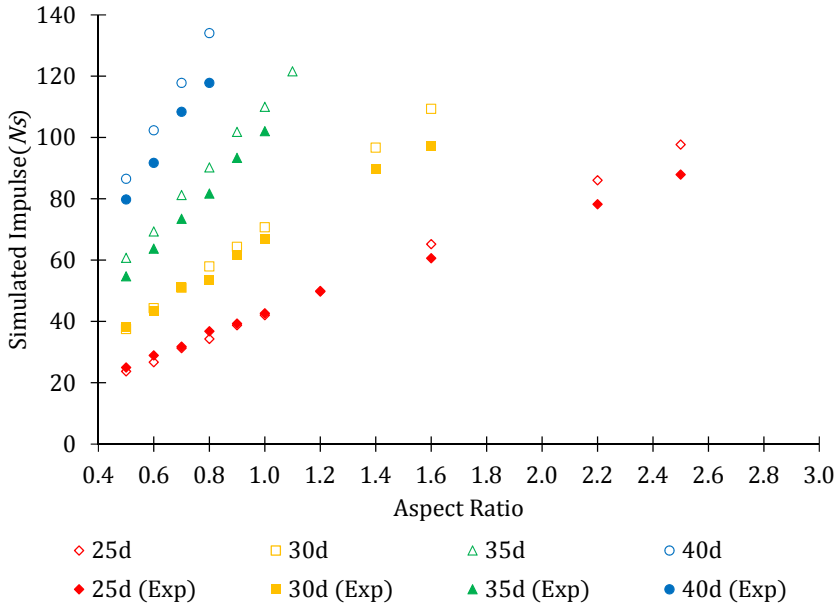

(a) Constant Diameter

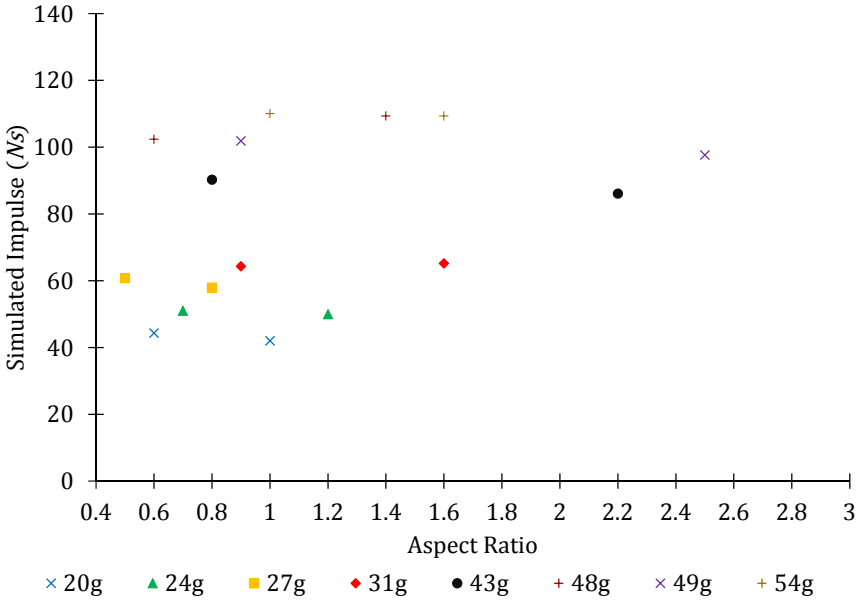

(b) Constant Mass

Figure 7.12: Axial Impulses (Simulated)

Constant Diameter, and Correlation

Figure 7.12(a) depicts the effect of aspect ratio (or charge mass) on the axial impulse, where the charge diameter is kept constant. Similar to Figure 4.12(a), the simulated axial impulse is directly proportional to aspect ratio.

Table 7.4 presents a comparison of the simulated and experimental axial impulses. The "m_{eff}^{axial}" column presents the axial effective charge masses of the simulated charges. Generally, the model overpredicted the axial impulses, which correlates with the models underprediction of the deflections. In terms of correlation, 72% of the impulses are within 10 % of the experimental magnitudes, and 28% are outside these boundaries. This indicated that the detonation physics of the PE4 explosive had some uncertainty.

Table 7.4: Comparison Simulated and Experimental Impulses

Charge	m	m_{eff}^{axial}	**Exp.**	**Sim.**	**Charge**	m	m_{eff}^{axial}	**Exp.**	**Sim.**
Units of Impulse in Ns, and Units of Axial Effective Charge Mass in g									
m Markers: 20 (♣), 24 (✿), 27 (➲) 31 (❣), 34 (✜), 43 (✄), 48 (▼), 49 (✌), 54 (✖) g Charges									
10g_25d_0.5		5.243	24.96	23.71	34g_30d_1	✜	9.801	66.71	70.74
12g_25d_0.6		5.507	28.90	26.73	48g_30d_1.4	▼	9.801	89.74	96.68
14g_25d_0.7		5.632	31.81	31.30	54g_30d_1.6	✖	9.801	97.11	109.30
16g_25d_0.8		5.669	36.79	34.28	27g_35d_0.5	➲	14.388	54.70	60.74
18g_25d_0.9		5.672	39.32	38.74	32g_35d_0.6		15.112	63.74	69.35
20g_25d_1	♣	5.672	42.63	42.04	38g_35d_0.7		15.453	73.44	81.20
24g_25d_1.2	✿	5.672	49.75	49.95	43g_35d_0.8	✄	15.556	81.67	90.22
31g_25d_1.6	❣	5.672	60.63	65.21	49g_35d_0.9	✌	15.563	93.36	101.84
43g_25d_2.2	✄	5.672	78.26	86.06	54g_35d_1	✖	15.563	102.07	110.01
49g_25d_2.5	✌	5.672	87.93	97.67	59g_35d_1.1		15.563	81.45	121.58
17g_30d_0.5		9.061	38.11	37.52	40g_40d_0.5		21.477	79.80	86.50
20g_30d_0.6	♣	9.517	43.48	44.31	48g_40d_0.6	▼	22.558	91.71	102.38
24g_30d_0.7	✿	9.517	51.38	51.01	56g_40d_0.7		23.067	108.36	117.81
27g_30d_0.8	➲	9.796	53.64	57.92	64g_40d_0.8		23.221	117.81	134.07
31g_30d_0.9	❣	9.796	61.77	64.33					

Constant Mass, and Axial Effective Charge Mass Effects

Figure 7.12(b) depicts the effect of aspect ratio on the impulse, where the mass is kept constant. The short charges transferred more axial impulse to the reflective boundary than their mass equivalent long charges. Figure 7.13 depicts pressure contour plots of the 43 g charges pressure histories at 0.04 ms, which continues from the pressure contour plots that are shown on Figure 7.6.

Figure 7.12(b) show that the axial impulse that was transferred to the reflective boundary from the 43g_35d_0.8 was greater, because its high pressure zone acted over a larger area and its boundary layer thickness was greater than that from the 43g_25d_2.2 charge. The short charges higher axial impulse was caused by its diameter, which made up for its lack of length. The larger diameter lead to a bigger fraction of the charge contributing directly to the axial impulse.

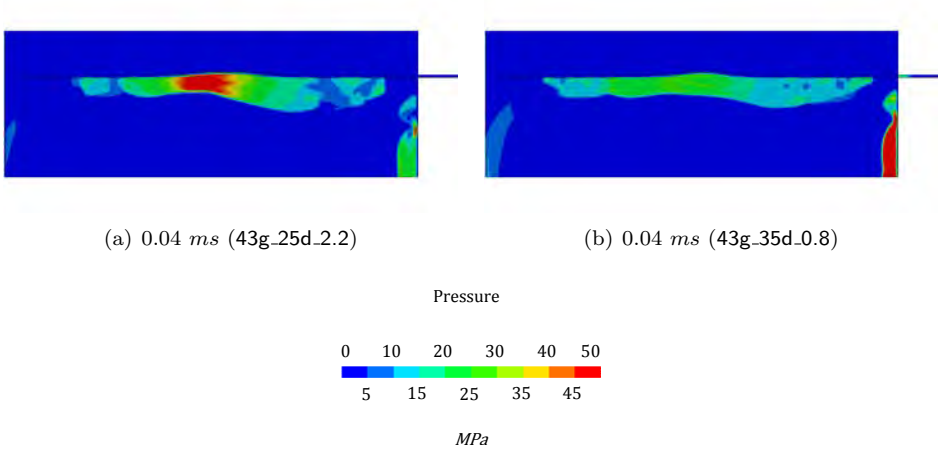

(a) 0.04 ms (43g_25d_2.2) (b) 0.04 ms (43g_35d_0.8)

Figure 7.13: Pressure Contour Plots Comparison of Simulated Pressure (43 g Charges)

7.3.2 Averaged Peak Pressure

Effect of Peak and Gas Pressure on Axial Impulse at the Reflective Boundary

A graph of simulated peak pressure *vs* aspect ratio is shown in Figure 7.14. The averaged pressure with respect to time was calculated with Equation 6.8 and the peak pressure was extracted and plotted herein.

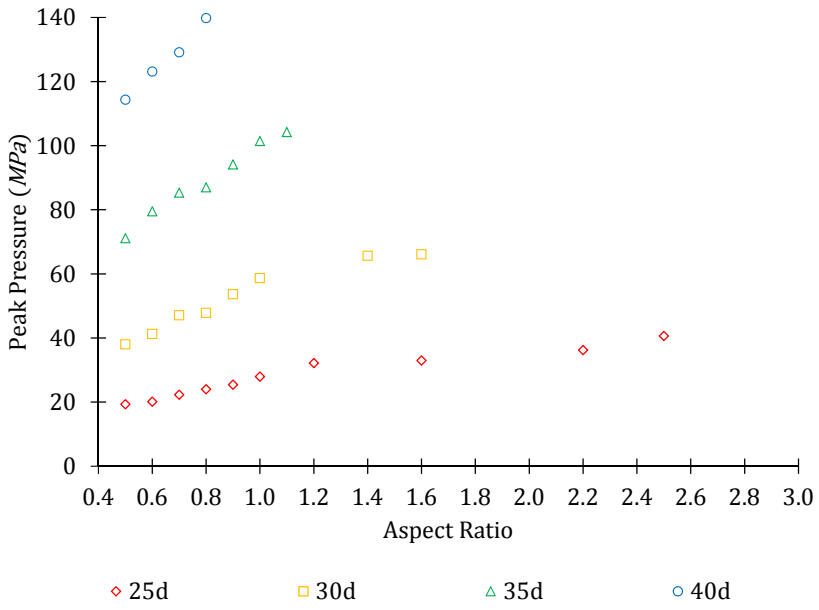

Figure 7.14: Simulated Peak Pressure (Constant Diameter)

The averaged peak pressure at the reflective boundary increased as the aspect ratio increased, when the diameter was kept constant. At higher aspect ratios, for all diameter cases, the averaged peak pressures rate of change decreased. The simulated impulse with respect to aspect ratio, of Figure 7.12(a), increased

at a constant rate, yet the slope of the peak pressure with respect to aspect ratio eventually decreased. This meant that the gas pressure, which accumulated in the cylinder, had more of a role in transferring axial impulse to the reflective boundary, especially at high aspect ratios (refer to Figure 7.9). It is noted that the magnitude and duration of gas pressure depend on the geometry, volume, and degree at which the structure confines a charge [14].

Peak Pressure Histories

Figure 7.15, 7.16, 7.17, and 7.18 depict the averaged pressure histories of the simulated 25, 30, 35, and 40 diameter mm charges, respectively.

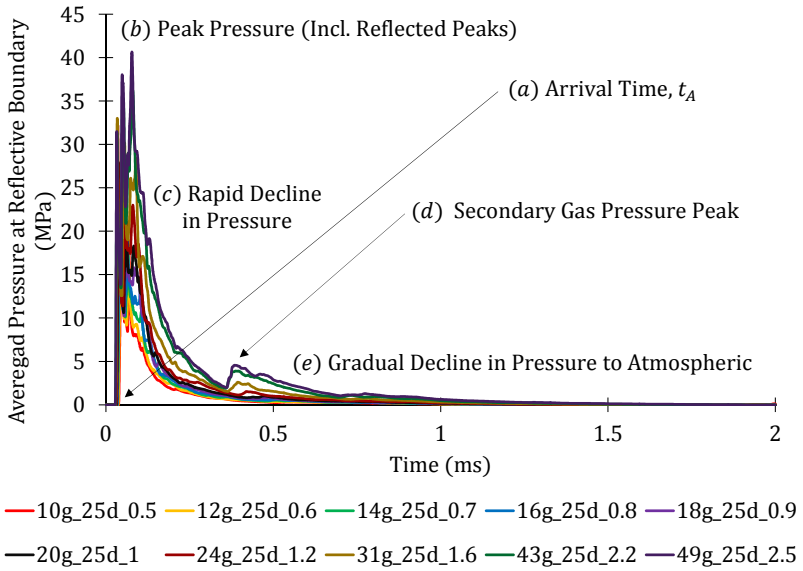

Figure 7.15: Averaged Peak Pressure Histories Obtained Using LS DYNA (25 mm Charges)

The simulated pressure histories show similar characteristics:

- From 0 — (a): Before blast wave impinged on the reflective boundary (that is, $t < t_A$), the gauge pressure was zero (absolute $P = P_{ref}$).
- From (a) — (b): At the arrival time the blast wave impinged on the reflective boundary and the averaged pressure increased rapidly.
- From (b) — (c): After the peak pressure was reached, the pressure decreased exponentially.
- From (c) — (d): During the rapid decline, a small and sudden rise in the pressure occured after approximately 0.4 ms. This was caused by the accumulation of gas pressure in the cylinder. The gas pressure transferred additional axial impulse to, and prolonged the duration of the pressure against the reflective boundary.
- From (d) — (e): After the gas pressure spike, the pressure gradually decreased to atmospheric.

The points (a) to (e) are labelled on the pressure-time histories. Similarly shaped histories were obtained for all charge diameters. As charge mass and diameter increased, peak pressure increased.

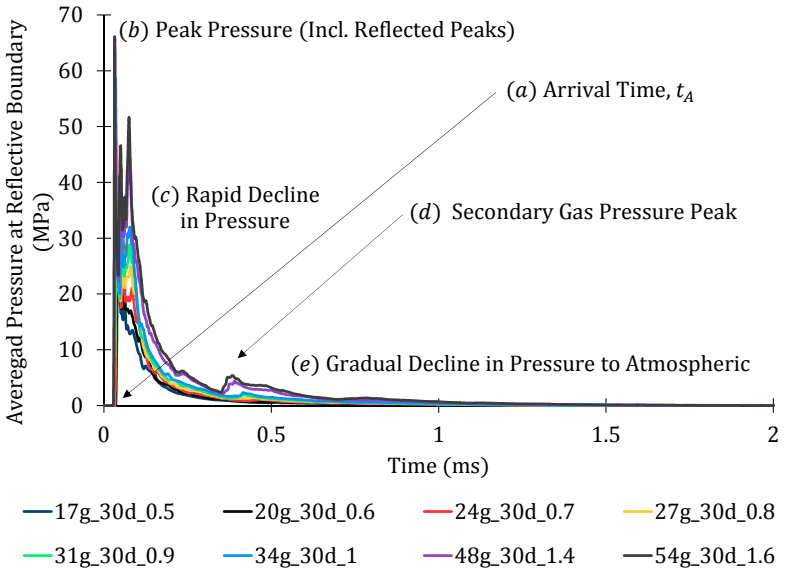

Figure 7.16: Averaged Peak Pressure Histories Obtained Using LS DYNA (30 mm Charges)

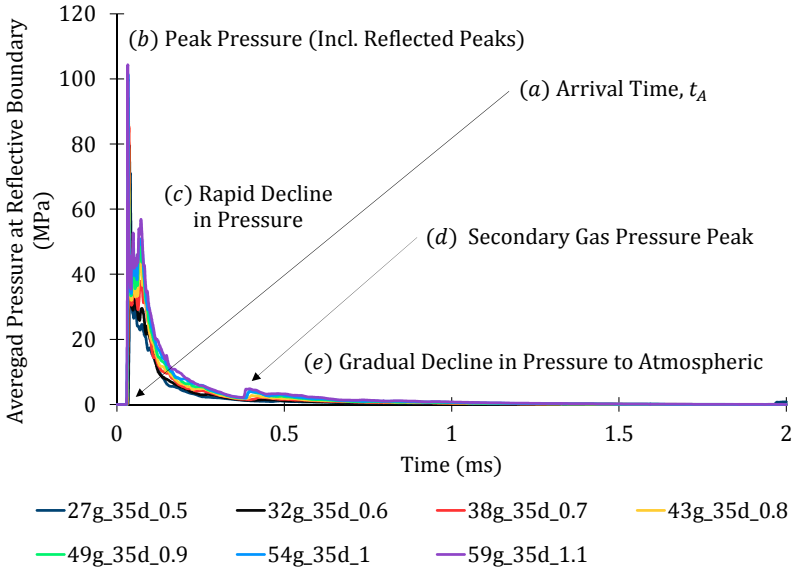

Figure 7.17: Averaged Peak Pressure Histories Obtained Using LS DYNA (35 mm Charges)

Force and Impulse History Example

Figure 7.19 presents an example of the total force-time, and impulse-time graphs. In all tests, the impulse rose rapidly after the arrival time, then levelled off as the total force died down to zero (or when the averaged pressure approached atmospheric). In some cases, gas pressure accumulated in the cylinder and caused a sudden rise in the impulse.

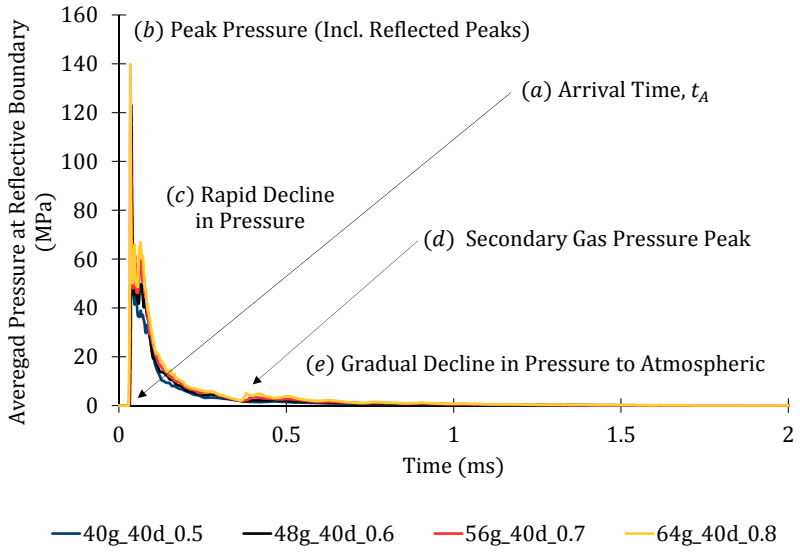

Figure 7.18: Averaged Peak Pressure Histories Obtained Using LS DYNA (40 mm Charges)

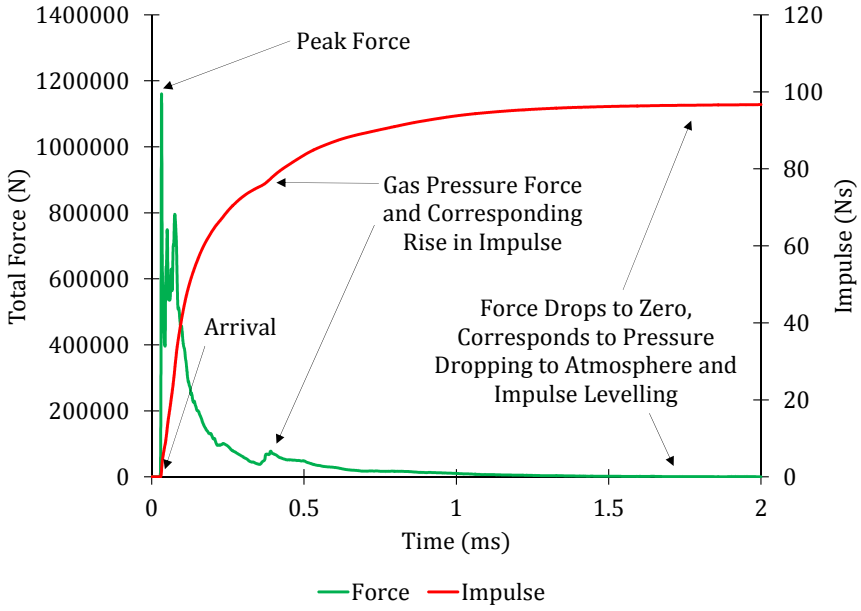

Figure 7.19: Example of Force and Impulse Histories at Reflective Boundary (48g_30d_1.4)

7.4 Charge Geometry

Figure 7.20, 7.21, and 7.22 depicts the simulated cylinder profiles resulting from cylindrical and mass equivalent spherical charge detonations, all of which had an aspect ratio of 1.
The cylindrical charges produced larger diametric deflections than their mass equivalent spherical charges. The primary bulges caused by the spherical charge detonations were spread over a larger area than those

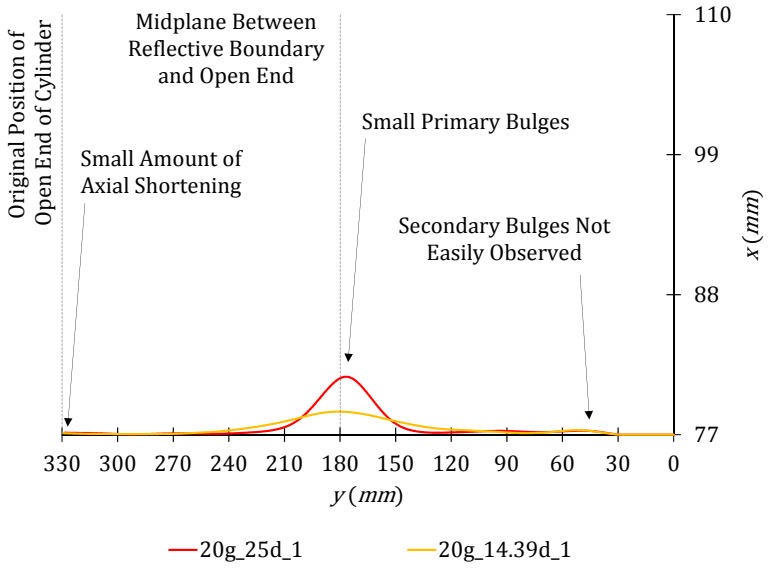

Figure 7.20: Simulated Profiles of Cylinders Loaded by Detonations of 20 g Cylindrical and Spherical Charges

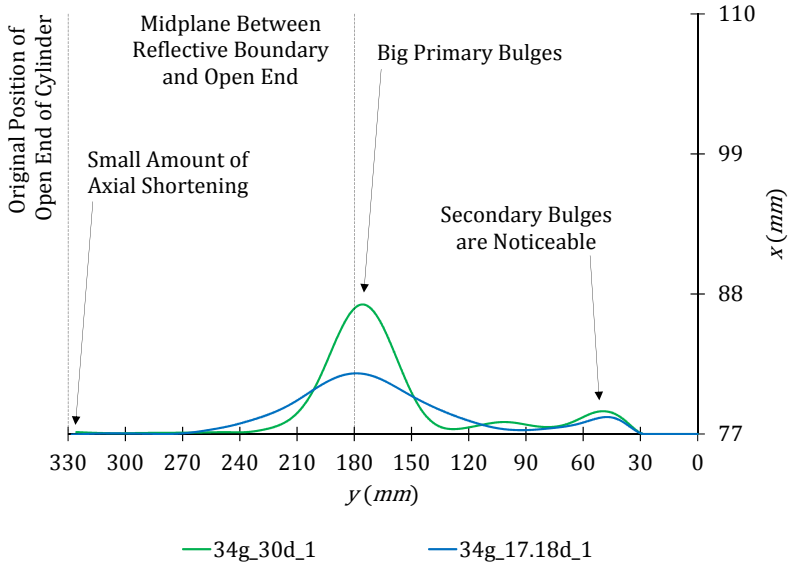

Figure 7.21: Simulated Profiles of Cylinders Loaded by Detonations of 34 g Cylindrical and Spherical Charges

caused by the cylindrical charges. This same was true experimentally (as shown, for example in Figure 4.17). Figure 7.23 depicts the initial blast wave propagation of the cylindrical and spherical 20 g charges before impinging on the walls. The blast wave from the spherical charge (Figure 7.23(b)) propagated spherically, which the blast wave propagation from the cylindrical charge (Figure7.23(a)) was highly directional. The same was true for the 34 and 54 g charges.

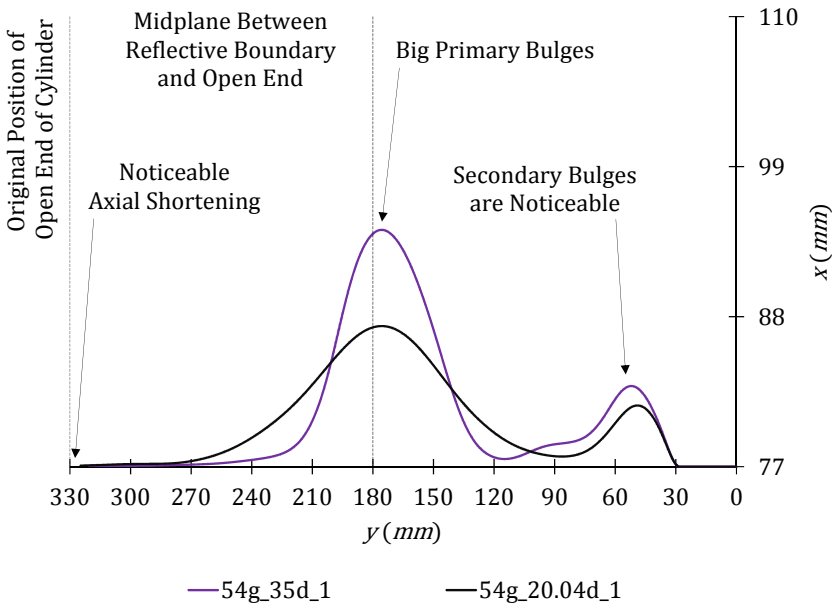

Figure 7.22: Simulated Profiles of Cylinders Loaded by Detonations of 54 g Cylindrical and Spherical Charges

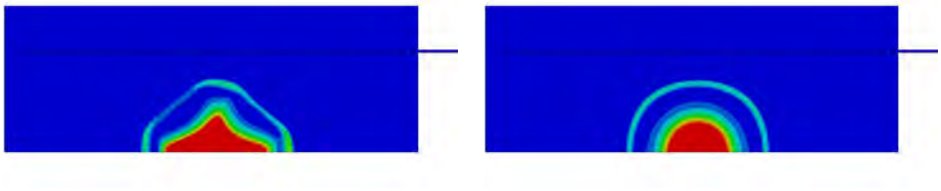

(a) 20 g Cylindrical Charge, 25 mm Diam.

(b) 20 g Spherical Charge

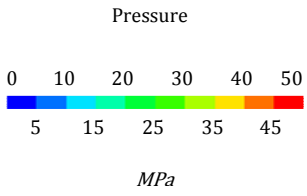

(c) Pressure Colour Bar (MPa)

Figure 7.23: Simulated Blast Wave Propagation Shape After 0.01 ms

Table 7.5 presents a comparison of the simulated and experimental data of the 20, 34, and 54 g cylindrical and spherical charges, all of which had an aspect ratio of 1. With respect to the spherical charges, the model predicted 67% of the maximum diametric deflections within the acceptable 2 cylinder thicknesses, predicted all of the axial shortenings to within the acceptable 2 mm cylinder thicknesses, and predicted 67% of the impulses to within 10%. The simulated cylindrical charges caused more maximum diametric deflection and axial shortening (almost twice those caused by their mass equivalent spherical charges).

Table 7.5: Comparison of Simulated and Experimental Data (Spherical and Cylindrical Charges, $R_{ld} = 1$)

—	**Experimental**			**Simulated**		
Max. Defl. and Axial Short. Units in mm, Axial Impulse Units in Ns						
Charge	**Imp.**	**Defl.**	**Short.**	**Imp.**	**Defl.**	**Short.**
20g_25d_1	42.63	9.22	2.08	42.04	9.10	1.45
20g_14.39d_1	41.60	4.58	0.93	41.91	3.62	0.76
34g_30d_1	66.71	21.80	4.55	70.74	20.35	4.28
34g_17.18d_1	71.25	13.43	0.97	70.13	9.52	1.90
54g_35d_1	102.07	44.24	15.05	110.01	34.72	9.57
54g_20.04d_1	94.83	26.68	8.27	107.12	20.62	5.31

7.5 Detonator Position

A preliminary investigation into the effect of detonator location in a cylindrical charge was conducted. Figure 7.24 depicts the profiles of the simulated cylinders that were affected by 34 g charges ($R_{ld} = 1$). An additional charge was simulated: 34g_30d_1 (Centre Detonation), and its simulated profile and data were compared to that of the 34g_30d_1 charge that was detonated at a 5 mm depth.

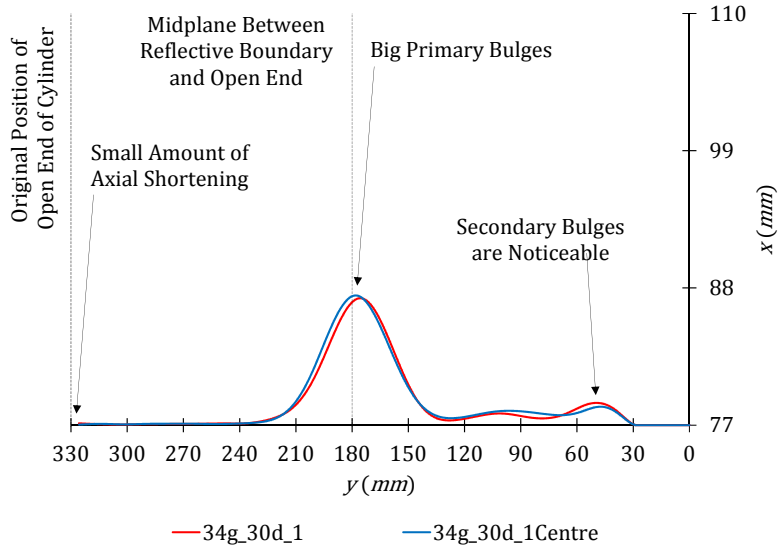

Figure 7.24: Simulated Profiles of Cylinders Affected by 34g_30d_1 Charges (Different Detonator Positions)

The simulated profiles of the 34g_30d_1 and 34g_30d_1 (Centre Detonation) profiles are similar in that their maximum diametric deflections look similar and their primary bulges are localised at the charge location, compared to that caused by the 34g_17.18d_1 charge. The primary bulge peak of the cylinder that was affected by the centrally detonated charge was further from its clamped end than the other cylinder, which correlated with the experimental trend. This is attributed to the highly localised radial propagation of the pressure blast after detonation, as depicted in Figure 7.25. There is a small offset in the position of maximum diametric deflection indicated in the deflection profile shown in Figure 7.24, due to the difference in the detonation position within the charge.

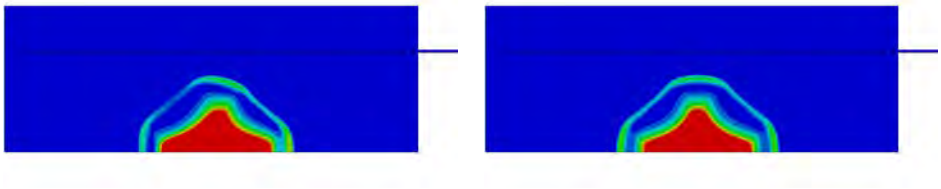

(a) 0.01 ms (34g_34d_1) (b) 0.01 ms (34g_30d_1, Center Detonation)

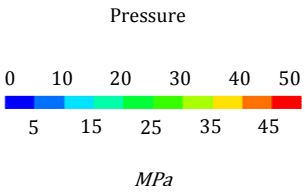

(c) Pressure Colour Bar (MPa)

Figure 7.25: Pressure Wave Profile Shape of Cylindrical and Mass Equivalent Spherical Charge

Table 7.6 presents a comparison of the simulated and experimental data, for the 34g_30d_1 charges that were detonated at different depths. The simulated blast model gave good agreement with the experimental maximum diametric deflections, axial shortenings, and impulses.

Table 7.6: Comparison of Simulated and Experimental Data of 34g_30d_1 Charges (Different Det. Pos.)

-	**Experimental**			**Simulated**		
Max. Defl. and Axial Short. Units in mm, Axial Impulse Units in Ns						
Charge	**Impulse**	**Defl**	**Short**	**Impulse**	**Defl**	**Short**
34g_30d_1	66.71	21.80	4.55	70.74	20.35	4.28
34g_30d_1 (Cent. Det.)	73.51	24.30	5.14	70.97	20.79	4.35

There was little discernable difference in the magnitudes of the maximum diametric deflections, axial shortenings, and axial impulses. Suggesting that the detonator position had little effect on the response of the cylinders. There was a small shift in the location of the primary bulge peak due to the different axial position of the detonator in the cylinder.

8

Conclusions

This Chapter presents the conclusions of the investigation, and compares them to the objectives in the introduction (refer to Chapter 1).

- Objective 1: Investigate the effect of cylindrical charges, with different aspect ratios, on the structural response right circular cylinders.
  - The maximum diametric deflection is directly proportional to the aspect ratio, or charge mass, when the diameter is kept constant. The rate at which the maximum diametric deflection changed, with respect to aspect ratio, increased as the diameter increased.
  - After blast loading, every cylinder axially shortened. The axial shortening increased linearly with increasing aspect ratio and maximum diametric deflection.
  - Some charges caused a secondary bulge to form at the closed end of some cylinders. The secondary bulge size increased as the aspect ratio increased, when the charge diameter was kept constant.
  - The impulse is directly proportional to the aspect ratio, or charge mass, when the charge diameter is kept constant. The rate at which the impulse changed, with respect to aspect ratio, increased as the charge diameter increased.
  - "Long" charges caused greater diametric deflections than their mass equivalent shorter charges, because the long charges had higher side effective charge mass that contributed directly to the deformation. Large deformations were also observed for longer charges that were lower in mass when the aspect ratio was high.
  - The maximum diametric deflection was directly proportional to the side effective charge mass.
  - Shorter charges transferred more axial impulse to the ballistic pendulum than the mass equivalent longer charges, as the shorter charges had larger diameters. The larger diameter charges had larger axial effective charge masses that contributed directly to the axial impulse.
  - The axial impulse increased as the axial effective charge mass increased, but continued to increase when the axial effective charge mass reached its theoretical maximum.
  - Three cylinders exhibit rupture failure at high charge mass.
- Objective 2: Compare the effects of spherical and mass equivalent cylindrical charges, both with an aspect ratio of 1, on the structural response of right circular cylinders.
  - The cylindrical charges resulted in greater diametric deflection and more axial shortening than the mass equivalent spherical charges.
  - There was little discernable effect on the axial impulse that was transferred to the ballistic pendulum.
  - The primary bulges caused by the cylindrical charge detonations were larger and more localised than those resulting from the spherical charge detonations.
  - The deflection profiles of both cylinders were similar, with a slight shift in the axial position of the primary bulge peak due to the change in the detonator position.
  - Magnitudes of the maximum diametric deflection, axial shortening, and impulse were similar in the 34 g cylinder tests with different detonator positions.
- Objective 3: Characterise seamless 304 stainless steel in the as received (that is, curved) state, and use the material properties in the simulated blast model.

- The similarity of the engineering stress-strain curves shows that the quasi-static tensile tests are highly repeatable.
- The inferred UTS values from the Vickers hardness tests are similar to those of the quasi-static tensile tests, which means that both data sets were reliable.
- The Johnson-Cook parameters were $A = 280.98\ MPa$, $B = 1319.95\ MPa$, and $n = 0.86$, which were obtained from tensile testing.

- Objective 4: Simulate the experiments with a Finite Element Analysis package to gain insight into phenomena that cannot be captured experimentally. Compare the simulated and experimental data sets. Use the simulated data in conjunction with the experimental data to explain how charge geometry and detonator position in a charge affects the structural response of right circular cylinders.
  - The simulated maximum diametric deflections followed the experimental trends, when the diameter and mass were kept constant.
  - The long charges caused more diametric deflections than their mass equivalent short charges, because their blast waves formed a high pressure ($P \geq 50MPa$) zone at cylinder wall that covered a larger area, was thicker, and lasted longer.
  - The simulated averaged peak pressure increased with increasing aspect ratio, however its rate of change eventually decreased.
  - The deflections caused by the cylindrical charges were more localised at the charge location than that of the mass equivalent spherical charges. This is caused by the directional propagation blast waves from the cylindrical charges, and the spherical propagation of blast waves from the spherical charges.
  - The effect of axial position of a detonator in the cylindrical `34g_30d_1` charge did not have much of an effect on the maximum diametric deflection, axial shortening, or axial impulse. A small offset in the primary bulge peaks of both cylindrical charges was observed, which was caused by the more localised radial propagation of the blast wave from the centrally detonated cylindrical charge.

9

Recommendations

- Extend this research to detonating fully confined cylindrical and spherical charges in seamless 304 stainless steel cylinders, and investigate the structural response.
- Investigate the effect of detonator position on the structural response of a right circular cylinder to internal air blasting. Use cylindrical charges with different diameters and aspect ratios, and spherical charges.
- Find the strain rate and thermal softening parameters of the Johnson-Cook material model for the seamless 304 stainless steel, for future simulations, by designing and implementing a methodology to characterise curved 304 stainless steel specimens in a split Hopkinson bar apparatus.
- Repeat some of the experiments with a pressure sensor on the boss of the ballistic pendulum, and use the data to validate the simulated average pressure histories which were captured in LS DYNA.

References

[1] J. Akhavan. *The Chemistry of Explosives*. Royal Society of Chemistry, 2 edition, 2004.

[2] T. Duffey, D. Mitchell. Containment of explosions in cylindrical shells. *International Journal of Mechanical Science*, 15:237–249, 1973.

[3] B.M. Dobratz, P.C. Crawford. *LLNL Explosives Handbook - Properties of Chemical Explosives and Explosive Simulants*. Lawrence Livermore National Laboratory, 1985.

[4] A. Alia, M. Souli. High explosive simulation using multi-material formulations. *Applied Thermal Engineering*, 26:1032–1042, 2005.

[5] D.J. Steinberg. *Equations of State and Strength Properties of Selected Materials*. Lawrence Livermore National Laboratory, 1996.

[6] L.F. Mori, S. Lee, Z.Y. Xue, A. Vaziri, D.T. Queheillalt, K.P. Dharmasena, H.N.G. Wadley, J.W. Hutchinson, H.D. Espinosa. Deformation and fracture modes of sandwich structures subjected to underwater impulsive loads. *Journal of Mechanics of Materials and Structures*, 2007.

[7] S. Lee, F. Barthelat, J.W. Hutchinson, H.D. Espinosa. Dynamic failure of metallic pyramidal truss core materials – experiments and modeling. *International Journal of Plasticity*, 2006.

[8] P.D. Smith, J.G. Hetherington. *Blast and Ballistic Loading of Structures*. Butterworth Heinemann, 1994.

[9] G.F. Kinney. *Explosive Shocks in Air*. Springer Science and Business Media, 1985.

[10] Salie Mahoi. *Influence of Shape of Solid Explosives on the Deformation of Circular Steel Plates-Experimental and Numerical Investigations*. PhD thesis, University of Cape Town, 2006.

[11] W.E. Baker. *Explosions in Air*. University of Texas Press, 1973.

[12] P.W. Cooper. *Explosives Engineering*. Wiley-VCH, 1996.

[13] J.E. Kennedy. Explosive output for driving metal. In *Proceedings of the* 12^{th} *Annual Symposium of the New Mexico Section of the ASME*, March 1972.

[14] U.S. Army Corp of Engineers, Naval Facilities Engineering Command, Air Force Civil Engineering Support Agency. *UFC 3-340-02*, volume Chapter 2 - Blast, Fragment and Shock Loads. United States Department of Defense, 2014.

[15] I. Edri, Z. Savir, V.R. Feldgun, Y.S. Karinski, D.Z. Yankelevsky. On blast pressure analysis due to a partially confined explosion: I. experimental studies. *International Journal of Protective Structures*, 2(1), 2011.

[16] V.R. Feldgun, Y.S. Karinski, I. Edri, D.Tsemakh, D.Z. Yankelevsky. On blast pressure analysis due to a partially confined explosion: Ii. numerical studies. *International Journal of Protective Structures*, 3(1), 2012.

[17] I. Edri, V.R. Feldgun, Y.S. Karinski, D.Z. Yankelevsky. On blast pressure analysis due to a partially confined explosion: Iii. afterburning effect. *International Journal of Protective Structures*, 3(3), 2012.

[18] W.R. Wise, J.F. Proctor. *Explosion containment laws for nuclear reactor vessels.* United States Naval Ordinance Laboratory, 1965.

[19] R.A. Benham, T.A. Duffey. Experimental-theoretical correlation on the containment of explosions in closed cylindrical vessels. *International Journal of Mechanical Science*, 16:549–558, 1974.

[20] N. Rushton, G.K. Schleyer, A.M. Clayton, S. Thompson. Internal explosive loading of steel pipes. *Thin-Walled Structures*, 46:870–877, April 2008.

[21] G.K. Schleyer, N.J. Rushton. Experimental investigation of large plastic deformation and fracture in explosively loaded open-ended steel cylinders. *International Journal of Safety and Security*, 1(1):1–16, 2013.

[22] A. Ozinsky. The response of partially-confined right-circular cylinders of internal blast loading. Master's thesis, University of Cape Town, 2012.

[23] G.S. Langdon, A. Ozinsky, S.C.K. Yuen. The response of partially confined right circular stainless steel cylinders to internal air-blast loading. *International Journal of Impact Engineering*, 73:1–14, 2014.

[24] E384-11. Standard test method for knoop and vickers hardness of materials.

[25] C. Geretto. *The Effects of Different Degrees of Confinement on the Deformation of Square Plates Subjected to Blast Loading.* PhD thesis, University of Cape Town, 2012.

[26] M. Silvestrini, B. Genova, F.J. Leon Trujillo. Energy concentration factor. a simple concept for the prediction of blast propagation in partially confined geometries. *Journal of Loss Prevention in the Process Industries*, 22:449–454, 2009.

[27] C. Geretto, S. Chung Kim Yuen, G.N. Nurick. An experimental study of the effects of degrees of confinement on the response of square mild steel plates subjected to blast loading. *International Journal of Impact Engineering*, 79:32–44, 2015.

[28] D. Leibovici, O. Gofrit, M.Stein, S.C. Shapira, Y. Noga, R.J. Heruti, J. Shemer. Blast injuries: Bus versus open air bombings - a comparative study of injuries in survivors of open-air versus confined space explosions. *Trauma: Injury, Infection, and Critical Care*, 41(6):1030–1035, 1996.

[29] W. Ficket, W.C. Davis. *Detonation Theory and Equipment.* Dover Publications, 1979.

[30] C.A. Mills. The design of concrete structure to resist explosions and weapon effects. *Conference on concrete for hazard protections*, 1987.

[31] S.E. Rigby, P.W. Sielicki. An investigation of tnt equivalence of hemispherical pe4 charges. *Engineering Transactions*, 62(4):423–435, 2014.

[32] P.W. Cooper, S.R. Kurowski. *Introduction to the Technology of Explosives*. Wiley-VCH, 1996.

[33] S. Weckert, C. Anderson. A preliminary comparison between tnt and pe4 landmines. Technical report, Weapons Systems Division, DSTO Defence Science, Technology Organisation, 2006.

[34] United States Counterterrorism Center. Tnt equivalents for various explosives and fuel-air mixtures. http://www.nctc.gov/site/technical/tnt.html, March 2015.

[35] W.A. Keenan, J.E. Tancreto. Blast environment from fully and partially vented explosions in cubicles. Technical report, Department of the Army, 1975.

[36] T.A. Duffey, R.R. Karpp, T.R. Neal. *Response of Containment Vessels to Blast Loading*. Los Alamos Scientific Laboratory, 1982.

[37] E8/E8M-15a. Standard test methods for tension testing of metallic materials.

[38] Böhler Edelstahl GmbH. *Conversion Table for Vickers Hardness, Brinell Hardness, Rockwell Hardness and Tensile Strength*.

[39] J. Magg Love Special Steels. *Manual*.

[40] Böhler Stocklist. *Manual*.

[41] Livermore Software Technology Corporation. *LS-DYNA KEYWORD USER'S MANUAL, VOLUME I*, 5471 edition, May 2014.

[42] Livermore Software Technology Corporation. *LS-DYNA KEYWORD USER'S MANUAL, VOLUME II, Material Models*, 5442 edition, May 2014.

[43] P.J. Roache. Quantification of uncertainty in computational fluid dynamics. *Fluid Mechanics*, 29(123-160), 1997.

[44] G.N. Nurick. An emperical solution for predicting maximum central deflections of impulsive loaded plates. *Mechanical Properties at High Strain Rates*, pages 457–464, 1989.

[45] John O. Hallquist. *LS-DYNA Theory Manual*. Livermore Software Technology Corporation, March 2006.

[46] R. Merrifield R.K. Wharton, S.A. Formby,. Airblast tnt equivalence for a range of commercial blasting explosives. *Journal of Hazardous Materials*, A79:31–39, 2000.

Appendix A

Ballistic Pendulum Impulse Inference

This Appendix presents the derivation of the formulae used to infer the experimental impulse, that was transferred to the ballistic pendulum [25]. Two calculation methodologies are also presented.

A.1 Derivations

A.1.1 The Homogeneous Differential Equation

The equation of motion for a pendulum is given by Equation A.1.

$$M\ddot{x} + C\dot{x} + Kx = 0 \tag{A.1}$$

Where M is the mass of the pendulum, which includes the counterweights, the I-beam, and the test rig; C is the damping coefficient of the system; and K is the stiffness of the system.

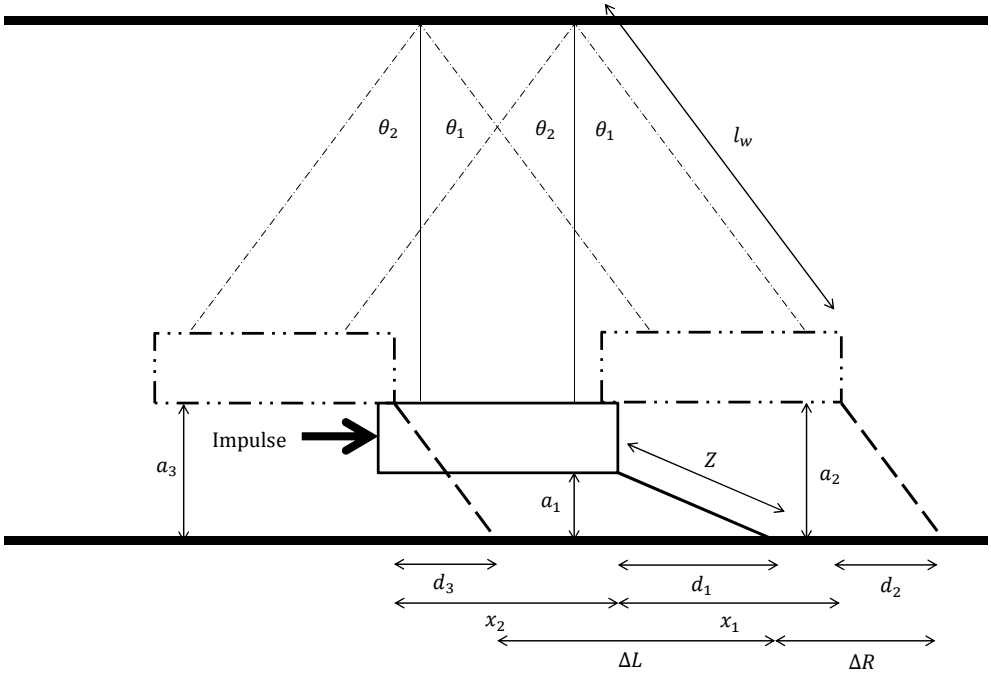

Figure A.1: Schematic drawing of the Ballistic Pendulum Oscillation [25]

Dividing throughout by M, Equation A.2 is derived.

$$\ddot{x} + \frac{C}{M}\dot{x} + \frac{K}{M}x = 0 \tag{A.2}$$

A.1.2 General Solution

By inspection the eigenvalues are calculated using Equation A.3.

$$\lambda_{1,2} = \frac{-\frac{C}{M} \pm \sqrt{\left(\frac{C}{M}\right)^2 - 4\left(\frac{K}{M}\right)}}{2} = -\frac{C}{2M} \pm \frac{1}{2}\sqrt{\left(\frac{C}{M}\right)^2 - 4\left(\frac{K}{M}\right)} = -\frac{C}{2M} \pm \sqrt{\left(\frac{C}{2M}\right)^2 - \left(\frac{K}{M}\right)} \tag{A.3}$$

When the system is critically damped, the difference under the square root sign will be equal to zero. The critical damping is calculated using Equation A.4.

$$C_c = 2\sqrt{KM} \tag{A.4}$$

The damping ratio is defined as the quotient of the system's current damping to its critical damping, which is calculated using Equation A.5.

$$\zeta = \frac{C}{C_c} = \frac{C}{2\sqrt{KM}} \tag{A.5}$$

Remembering that the stiffness of a system relative to the undamped natural frequency and its mass is calculated using Equation A.6.

$$K = \omega_0^2 M \tag{A.6}$$

Substituting K into Equation A.5, Equation A.7 is derived.

$$\zeta = \frac{C}{2\sqrt{\omega_0^2 M^2}} = \frac{C}{2\omega_0 M} \tag{A.7}$$

A new constant is defined by Equation A.8.

$$\beta = \zeta\omega_0 = \frac{C}{2M} \tag{A.8}$$

Substituting β into Equation A.3, Equation A.9 is derived.

$$\lambda_{1,2} = -\beta \pm \sqrt{\zeta^2\omega_0^2 - \omega_0^2} = -\beta \pm \omega_0\sqrt{\zeta^2 - 1} \tag{A.9}$$

Table A.1 presents the different cases for damping, and its corresponding ζ value.

Table A.1: The Effect of Damping on ζ

Under Damped	ζ<1
Critically Damped	$\zeta = 0$
Over Damped	$\zeta \geq 1$

For the under damped case, the motion will be exponentially decaying yet harmonic. For the critically damped case, the motion is non harmonic, and decays exponentially, while it asymptotically approaches zero. For the over damped case, the motion is also non harmonic, decays exponentially, yet takes longer to asymptotically approach zero relative to the critically damped case.

For the general solution, the horizontal displacement is calculated using Equation A.10.

$$x = Ae^{\lambda_1 t} + Be^{\lambda_2 t} \tag{A.10}$$

The horizontal velocity is calculated using Equation A.11.

$$\dot{x} = \lambda_1 Ae^{\lambda_1 t} + \lambda_2 Be^{\lambda_2 t} \tag{A.11}$$

The horizontal acceleration is calculated using Equation A.12

$$\ddot{x} = \lambda_1^2 Ae^{\lambda_1 t} + \lambda_2^2 Be^{\lambda_2 t} \tag{A.12}$$

Where A and B are constants that are calculated based on the initial conditions.

Figure A.2 depicts the transient behaviour of an objects motion, after being exposed to the different damping regimes. The initial displacements and velocities are the same for all cases.

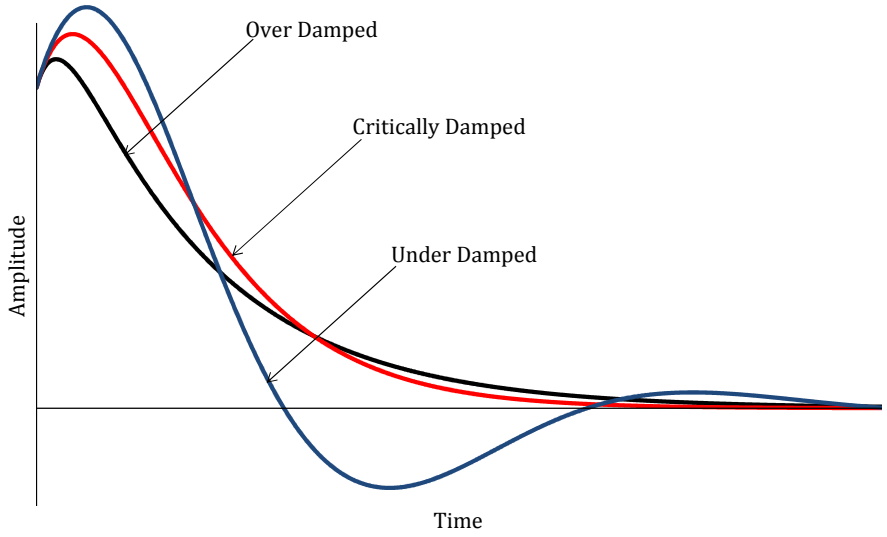

Figure A.2: Damping Curves with respect to Time for the Same Initial Amplitude and Velocity

A.1.3 Under Damped Case Solution

In practice, systems either have Coulomb (for example, wind resistance, kinetic friction, etcetera) or viscous damping (for example, vehicle shocks). Here it is assumed that the ballistic pendulum has Coulomb damping only. The damped frequency of the system is calculated using equation A.13.

$$\omega_d = \omega_0 \sqrt{1 - \zeta^2} \tag{A.13}$$

For the case where ζ<1, a complex component (that is, $i = \sqrt{-1}$) is introduced, the eigenvalues are calculated using Equation A.14.

$$\lambda_{1,2} = -\beta \pm \omega_0 \sqrt{-(1 - \zeta^2)} = -\beta \pm i\omega_0 \sqrt{1 - \zeta^2} = -\beta \pm i\omega_d \tag{A.14}$$

The horizontal displacement is calculated using Equation A.15.

$$x = Ae^{-\beta t + i\omega_d t} + Be^{-\beta t - i\omega_d t} = Ae^{-\beta t}e^{i\omega_d t} + Be^{-\beta t}e^{-i\omega_d t} \tag{A.15}$$

Using Euler's formula, the horizontal displacement is calculated using Equation A.16.

$$x = Ae^{-\beta t}\left[cos(\omega_d t) + isin(\omega_d t)\right] + Be^{-\beta t}\left[cos(-\omega_d t) + isin(-\omega_d t)\right] \tag{A.16}$$

Factorising $e^{-\beta t}$, A, and B, Equation A.17 is derived.

$$x = (A - B)e^{-\beta t}\left[cos(\omega_d t) + isin(\omega_d t)\right] = e^{-\beta t}\left[\Gamma cos(\omega_d t) + \Psi sin(\omega_d t)\right] \tag{A.17}$$

Where Γ real component of $(A - B)$, and Ψ is the complex part of $(A - B)i$. At $t = 0$, $x = 0$, therefore $\Gamma = 0$.

The horizontal velocity is calculated using Equation A.18.

$$\dot{x} = -\beta e^{-\beta t}\Psi sin\left(\omega_d t\right) + e^{\beta t}\Psi\omega_d sin\left(\omega_d t\right) \tag{A.18}$$

At $t = 0$, $\dot{x} = \dot{x_0}$, therefore $\Psi = \frac{\dot{x_0}}{\omega_d}$. The final solution of the horizontal displacement is calculated using Equation A.19.

$$x = \frac{e^{-\beta t}\dot{x_0}sin(\omega_d t)}{\omega_d} \tag{A.19}$$

The undamped natural frequency is also defined as $\omega_0 = \frac{2\pi}{T_0}$; where T_0 is the undamped natural period of the pendulum. The damped frequency is of concern in the remaining equations, thus, $\omega_d = \frac{2\pi}{T_d}$; T_d is the damped natural period of the pendulum. Table A.2 presents the horizontal distances travelled during the cycle immediately after the blast load is applied.

Table A.2: Horizontal Position of the Pendulum with respect to Time (1^{st} Cycle)

Time with respect to T_d	**x Position**	**Description**
$0T_d$	0	Pendulum is at rest
$0.25T_d$	x_1	Pendulum moves fully to the right
$0.5T_d$	0	Half the first cycle is done
$0.75T_d$	x_2	Pendulum moves fully to the left
T_d	0	The first cycle ends

Substituting $t = 0.25T_d$ into Equation A.19, x_1 is calculated using Equation A.20.

$$x_1 = \frac{e^{-0.25\beta T_d}\dot{x_0}sin(0.25\omega_d T_d)}{\omega_d} = \frac{e^{-0.25\beta T_d}\dot{x_0}}{\omega_d} = \frac{e^{-0.25\beta T_d}\dot{x_0}T_d}{2\pi} \tag{A.20}$$

The initial velocity of the pendulum is calculated using Equation A.21.

$$\dot{x_0} = \frac{2\pi x_1 e^{0.25\beta T_d}}{T_d} \tag{A.21}$$

Similarly, substituting $t = 0.75T_d$ into Equation A.19, x_2 is calculated using Equation A.22.

$$x_2 = \frac{e^{-0.75\beta T_d}\dot{x_0}T_d}{2\pi} \tag{A.22}$$

The ratio of x_1 to x_2 is calculated using Equation A.23.

$$\frac{x_1}{x_2} = e^{0.5\beta T_d} \tag{A.23}$$

Therefore, β is calculated using Equation A.24.

$$\beta = \frac{2}{T_d} ln\left(\frac{x_1}{x_2}\right) \tag{A.24}$$

β can be substituted into Equation A.21, and the impulse can be calculated using Equation A.25.

$$I = M\dot{x}_0 \tag{A.25}$$

A.2 Impulse Calculation Methodology

A.2.1 The Oscilloscope Method

Table A.3 presents the ballistic pendulum data, where the test numbers follow Table 3.2. Note that the mass of the pendulum was gradually increased, depending on the charge mass, to lessen its axial movement and prevent it from striking the oscilloscope sensor (see Figure 3.1).

Table A.3: Ballistic Pendulum Constants

Physical Quantity	**Magnitude**	**Units**
a	223	mm
Z	384	mm
l_w	2900	mm
T_d	3.45	s
β	-0.13 – 0.06	s^{-1}
Pendulum Mass	115.22	kg
Test Rig Mass	62.06	kg
Counterweight Mass	61.54	kg

The pendulum masses, including damping weights, is presented on Table A.5. Figure A.3 depicts a voltage history which was converted to a displacement history, and processed to calculate the impulse.

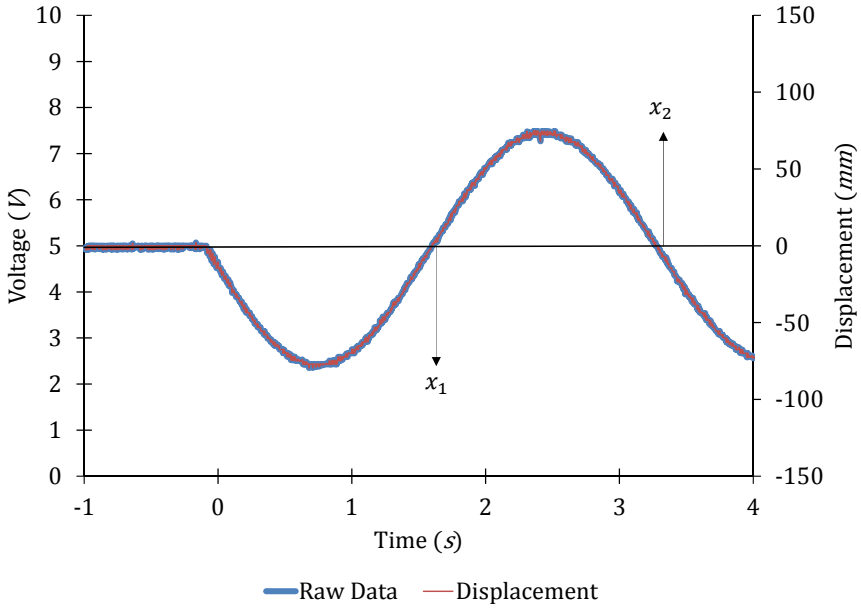

Figure A.3: Conversion of Voltage History to Displacement History (An Example)

Note that 5 V corresponded to a 150 mm distance of the pendulum end to the wall, and 10 V corresponded to the pendulum end striking the laser sensor (that is, clipping of the voltage history). The following steps, the method of which was coded in MATLAB (Refer to Appendix C.4), were followed to calculate the impulse using the voltage history which was recorded on the oscilloscope:

- the raw data was converted to a displacement history using Equation A.26.

$$d = 30V - 150 \qquad \text{units in } mm \tag{A.26}$$

- the damped period of the pendulum was calculated after the wire length was measured and substituted into Equation A.27, which is the formula of the period using the small angle approximation.

$$T_d = 2\pi\sqrt{\frac{l_w}{g}} \tag{A.27}$$

- x_1 and x_2, which were the respective minimum and maximum values in the displacment history, were substituted into Equation A.24 to calculate β.
- β, T_d, and x_1 were substituted into Equation A.21 to calculate the pendulums initial velocity.
- Equation A.25 was used to calculate the Impulse.

Figure A.4 depicts the voltage histories of the 72g_40d_0.9 and 72g_40d_0.8 tests that clipped, where the clipping implies that the end of the ballistic pendulum hit the laser sensor.

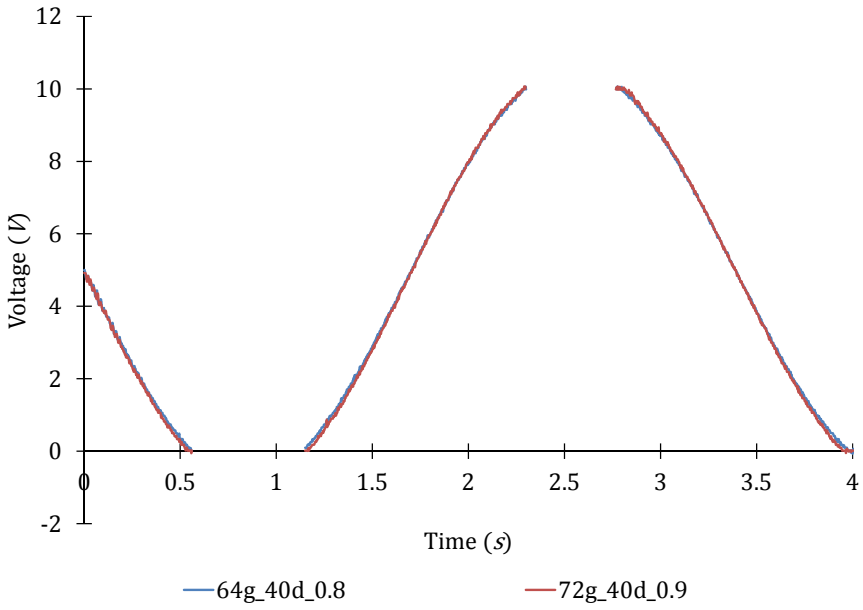

Figure A.4: Graph Showing Voltage Histories 72g_40d_0.9 and 64g_40d_0.8 Tests (Minus Clipped Data)

The clipping of the voltage, which affected the displacement history, was caused by the lack of damping weights to lessen the movement of the pendulum. The clipped data points were removed and a sixth

order polynomial was fit to the remaining data points. The x_1 and x_2 magnitudes were extrapolated to determine the maximum and minimum values. Table A.4 presents the parameters used to fit the polynomial to the data, and the correlation parameter.

Table A.4: Sixth Order Polynomial Fit Parameters for Clipped Displacement Histories

—	72g_40d_0.9	64g_40d_0.8
A	-3.6322	-3.5704
B	58.238	57.845
C	-320.64	-320.39
D	684.3	685.3
E	-356.49	-353.32
F	-227.49	-235.25
G	5.8403	6.222
R^2	0.997	0.997

Figure A.6 depicts the displacement histories with their respective fits.

Figure A.5: Parameters Used to Fit Polynomial to Displacement History

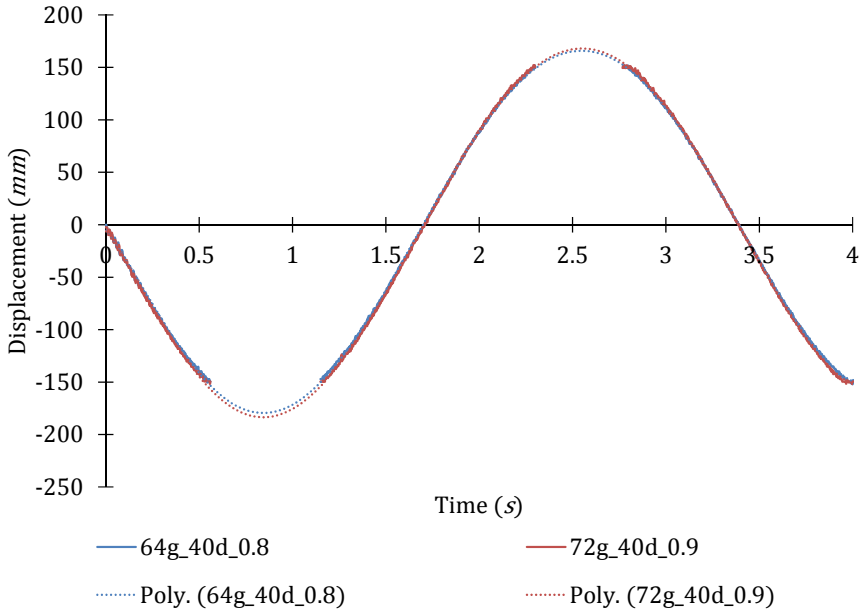

Figure A.6: Curve Fitting of Sixth Order Polynomial to Test 16 and 17 Displacement Histories

From the polynomials, $x_1 = 168\ mm$ and $x_2 = 184\ mm$ for the 72g_40d_0.9 test, $x_1 = 166\ mm$ and $x_2 = 179\ mm$ for the 64g_40d_0.8 test. The impulses of each test are presented on Table A.5.

A.2.2 The Pen Method

When the ballistic pendulum moves, the lines of length ΔR and ΔL, which are drawn on the tracing page, will not be of the same length as x_1 and x_2. Figure A.1 shows the relevant information for the calculations. When the pendulum is at rest the horizontal distance of the pens tip from the end of the pendulum is calculated using Equation A.28.

$$d_1 = \sqrt{Z^2 - a_1^2} \tag{A.28}$$

When the pendulum moves fully to the right, its base rises by $(a_2 - a_1)$ units.

$$a_2 = a_1 + l_w\,(1 - cos\theta_1) \tag{A.29}$$

The distance of the pens tip from the end of the pendulum is calculated using Equation A.30.

$$d_2 = \sqrt{Z^2 - a_2^2} = \sqrt{Z^2 - [a_1 + l_w\,(1 - cos\theta_1)]^2} \tag{A.30}$$

The x coordinate of the bottom rightmost line on the pendulum is calculated using Equation A.31.

$$x_1 = l_w sin\theta_1 \tag{A.31}$$

By inspection, an expression for d_1 can be found in terms of x_1, d_2, and ΔR. Making ΔR the subject of the formula, Equation A.32 is derived.

$$\Delta R = x_1 - d_1 + d_2 = l_w sin\theta_1 - \sqrt{Z^2 - a_1^2} + \sqrt{Z^2 - [a_1 + l_w\,(1 - cos\theta_1)]^2} \tag{A.32}$$

When the pendulum moves fully to the left, it's base rises by $(a_3 - a_1)$ units.

$$a_3 = a_1 + l_w\,(1 - cos\theta_2) \tag{A.33}$$

The distance of the pens tip from the end of the pendulum is calculated using Equation A.34.

$$d_3 = \sqrt{Z^2 - a_3^2} = \sqrt{Z^2 - [a_1 + l_w\,(1 - cos\theta_2)]^2} \tag{A.34}$$

The x coordinate of the bottom leftmost line on the pendulum is calculated using Equation A.35.

$$x_2 = l_w sin\theta_2 \tag{A.35}$$

By inspection, an expression for d_1 can be found in terms of ΔL, x_2, and d_3. Making ΔL the subject of the formula, Equation A.36 is derived.

$$\Delta L = d_1 - d_3 + x_2 = \sqrt{Z^2 - a_1^2} - \sqrt{Z^2 - [a_1 + l_w\,(1 - cos\theta_2)]^2} + l_w sin\theta_2 \tag{A.36}$$

The pen method was added as a redundancy, to calculate the impulse using the lengths of the lines drawn on the tracing paper, where the following steps were followed:

- the damped period of the pendulum was using Equation A.27.
- the solver in EXCEL was used to solve θ_1 and θ_2 from by setting ΔR (Equation A.32) and ΔL (Equation A.36) equal to their respective line lengths.
- θ_1 and θ_2 were substituted into Equations A.35 and A.31 to calculate x_1 and x_2 and solved, respectively.
- the magnitudes of x_1 and x_2 were substituted into Equation A.24 to calculate β.

- β, T_d, and x_1 were substituted into Equation A.21 to calculate the pendulums initial velocity.
- Equation A.25 was used to calculate the Impulse.

A.2.3 Correlation of Pen and Oscilloscope Method Impulses

Table A.5 presents the ΔR, ΔL, x_1, x_2, and impulse magnitudes, which were determined using the pen and oscilloscope methods.

Table A.5: Impulse Data Comparison (Pen and Oscilloscope Methods)

—		Pen Method					Oscilloscope Method		
Charge	M (kg)	ΔR (m)	ΔL (m)	x_1 (m)	x_2 (m)	I (Ns)	x_1 (m)	x_2 (m)	I (Ns)
10g_25d_0.5	238.82	0.059	0.06	0.059	0.060	25.78	0.059	0.063	24.96
12g_25d_0.6	238.82	0.065	0.075	0.066	0.074	26.72	0.068	0.072	28.90
14g_25d_0.7	238.82	0.076	0.077	0.077	0.076	33.41	0.075	0.080	31.81
16g_25d_0.8	238.82	0.083	0.083			36.79			
18g_25d_0.9	238.82	0.09	0.093			39.32			
20g_25d_1	317.86	0.072	0.078	0.073	0.077	40.72	0.075	0.079	42.63
24g_25d_1.2	317.86	0.084	0.09	0.085	0.089	47.91	0.086	0.089	49.75
31g_25d_1.6	317.86	0.105	0.106	0.106	0.105	62.00	0.105	0.109	60.63
43g_25d_2.2	408.5	0.108	0.117	0.109	0.110	81.04	0.108	0.116	78.26
49g_25d_2.5	408.5						0.120	0.126	87.93
59g_25d_3	408.5	0.101	0.122	0.102	0.120	70.08	0.113	0.133	77.89
17g_30d_0.5	238.82	0.082	0.089	0.083	0.088	34.90	0.089	0.094	38.11
20g_30d_0.6	238.82	0.1	0.1	0.101	0.099	44.51	0.101	0.106	43.48
24g_30d_0.7	317.86	0.087	0.091	0.088	0.090	50.25	0.089	0.092	51.38
27g_30d_0.8	317.86	0.096	0.097	0.097	0.096	56.53	0.094	0.099	53.64
31g_30d_0.9	317.86	0.108	0.108	0.109	0.107	64.12	0.108	0.113	61.77
34g_30d_1	408.5	0.091	0.098	0.092	0.097	66.65	0.092	0.098	66.71
48g_30d_1.4	408.5	0.121	0.131	0.123	0.129	89.07	0.122	0.128	89.74
54g_30d_1.6	343.28						0.15	0.153	97.11
27g_35d_0.5	408.5	0.078	0.082	0.079	0.081	57.62	0.076	0.083	54.70
32g_35d_0.6	408.5	0.087	0.092	0.088	0.091	64.23	0.088	0.095	63.74
38g_35d_0.7	408.5	0.102	0.111	0.103	0.110	74.53	0.101	0.107	73.44
43g_35d_0.8	408.5	0.111	0.119	0.113	0.117	81.89	0.113	0.121	81.67
49g_35d_0.9	408.5	0.125	0.138	0.127	0.136	91.23	0.127	0.133	93.36
54g_35d_1	408.5						0.140	0.150	102.07
59g_35d_1.1	408.5						0.121	0.151	81.45
65g_35d_1.2	408.5						0.151	0.152	113.44
40g_40d_0.5	408.5	0.107	0.118	0.108	0.116	77.77	0.109	0.113	79.80
48g_40d_0.6	408.5	0.123	0.136	0.125	0.134	89.65	0.125	0.132	91.71
56g_40d_0.7	408.5	0.141	0.159	0.144	0.156	102.27	0.147	0.152	108.36
64g_40d_0.8	408.5						0.166	0.179	118.78
72g_40d_0.9	408.5						0.168	0.184	119.28
20g_14.39d_1	408.5	0.058	0.066	0.058	0.065	40.99	0.058	0.065	41.60
34g_17.18d_1	408.5						0.115	0.119	71.25
54g_20.04d_1	408.5						0.151	0.153	94.83
10g_25d_0.5[a]	343.28						0.047	0.047	30.10
10g_25d_0.5[a]	343.28						0.052	0.047	34.82
17g_30d_0.5[a]	343.28						0.074	0.076	46.10
17g_30d_0.5[a]	343.28						0.062	0.061	39.24
34g_30d_1[b]	343.28						0.117	0.119	73.51

[a] Repeat tests

[b] Cylindrical charge that was detonated at its centre

The x_1 and x_2 magnitudes of both methods do not differ significantly. The same is true of the corresponding impulses, which, upon close inspection, reveals that the disparity between the values, of all tests, is less than 13%. Further inspection of the corresponding impulses reveals that the disparities between the values from most tests are less than 6.5%. These findings prove that, relative to the oscilloscope method, the pen method is a reliable way to determine the axial impulse that is transferred to a ballistic pendulum, despite the possibility of experimental variation in the ΔR and ΔL measurements.

Figure A.7 depicts the data impulses on a parity graph, where the 6.5% and 13% boundaries are included. Impulses that were not inferred using the oscilloscope method are not plotted here.

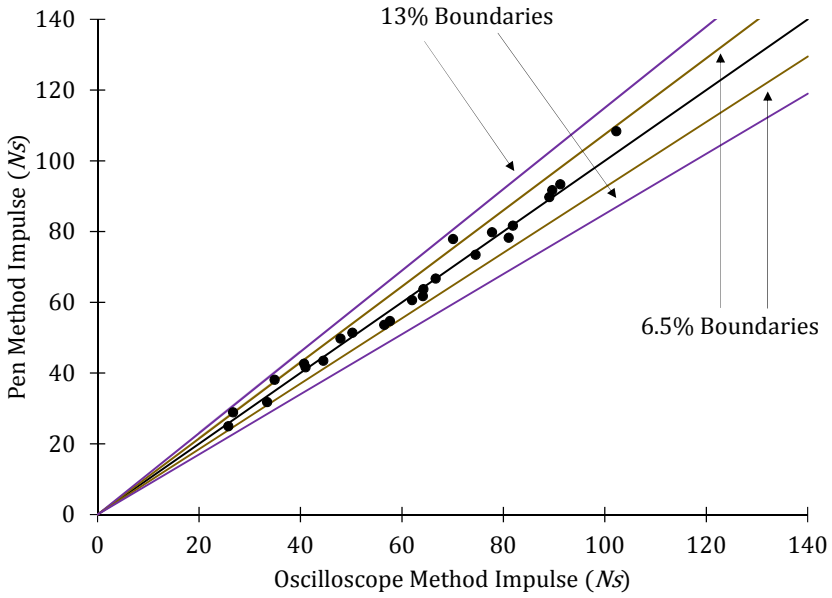

Figure A.7: Parity Graph of the Correlation of the Pen and Oscilloscope Impulses

Appendix B

Raw Data

B.1 Maximum Diametric Deflection

Table B.1 presents the maximum diametric deflection measurements. These measurements were taken with a micromenter that had an accuracy of 0.01 *mm*. Note that the outer diameter of the cylinder, before testing, was 154 *mm*. Therefore, these values were arrived at by taking the measurements and: removing 4 *mm* when the 150 *mm* spindle was used, adding 21 *mm* when the 175 *mm* spindle was used, and adding 46 *mm* when the 200 *mm* spindle was used. Measurements of the ruptured tubes were excluded here.

Table B.1: Maximum Diametric Deflection Measurements

Charge	Concatenated Measurements	Average	Std Dev.	Std Error.
10g_25d_0.5	1.69_1.93_2.9_2.18_1.94_1.66_1.37_1.92	1.95	0.45	0.06
12g_25d_0.6	3.28_2.85_2.78_2.3_1.67_1.29_1.3_2.92	2.30	0.78	0.10
14g_25d_0.7	4.5_4.14_4.03_3.86_3.6_3.74_3.75_3.8	3.93	0.29	0.04
16g_25d_0.8	6.67_6.55_6.2_6.34_6.41_5.88_5.26_5.6	6.11	0.49	0.06
18g_25d_0.9	9.55_8.92_9.26_8.82_8.14_8.23_8.87_9.45	8.91	0.52	0.06
20g_25d_1	9.61_9.88_10.06_7.89_8.18_9.22_9.73_	9.22	0.86	0.11
24g_25d_1.2	14.75_14.22_12.58_12.18_13.71_14.67_14.52_14.5	13.89	0.99	0.12
31g_25d_1.6	25.45_26.6_27.26_26.52_25.7_24.67_24.46_24.67	25.67	1.04	0.13
43g_25d_2.2	42.63_43_44.66_45.86_46.17_45.74_44.35_42.85	44.41	1.45	0.18
49g_25d_2.5	54.25_53.39_53.22_52.94_53.08_53.1_54.24_54.46	53.59	0.62	0.08
17g_30d_0.5	5.11_5.31_5.33_5.5_5.7_5.78_5.4_5.21	5.42	0.23	0.03
20g_30d_0.6	7.49_7.94_8.48_8.44_8.52_8.53_8.55_8.09	8.26	0.38	0.05
24g_30d_0.7	6.04_7_8.67_9.55_10.33_10.36_8.95_6.93	8.48	1.64	0.21
27g_30d_0.8	15.85_15.74_15.28_15.05_14.7_14.48_14.71_15.1	15.11	0.49	0.06
31g_30d_0.9	20.71_20.81_21.15_20.89_20.34_20.19_20.53_20.55	20.65	0.31	0.04
34g_30d_1	21.57_21.39_21.71_22.59_22.45_21.26_21.85_21.58	21.80	0.48	0.06
48g_30d_1.4	44.82_45.02_42.45_42.53_42.81_44.19_44.62_42.83	43.66	1.11	0.14
54g_30d_1.6	55.65_55.88_56.69_55.51_55.8_55.48_54.3_55.35	55.58	0.66	0.08
27g_35d_0.5	10.15_10.56_10.87_10.09_10.25_10.85_10.06_9.85	10.34	0.38	0.05
32g_35d_0.6	15.9_15.87_16.34_16.74_17.28_17.68_18.13_18.44	17.05	0.99	0.12
38g_35d_0.7	26.19_25.98_25.36_24.93_25.21_25.79_26.19_	25.66	0.50	0.06
43g_35d_0.8	29.97_30.34_31.15_31.28_30.37_30.11_30.16_30.11	30.44	0.50	0.06
49g_35d_0.9	38.79_38.27_38.84_39.05_39_38.02_37.74_38.14	38.48	0.50	0.06
54g_35d_1	43.09_42.71_44.43_45.04_44.92_44.89_45.06_43.74	44.24	0.94	0.12
59g_35d_1.1	42.34_43.29_43.9_46.29_48.07_45.29_43.42_48.07	45.08	2.21	0.28
40g_40d_0.5	19.32_19.47_18.73_18.87_19.8_19.99_19.71_19.37	19.41	0.44	0.05
48g_40d_0.6	26.02_26.03_26.44_26.18_26.59_27.04_26.61_26.09	26.38	0.36	0.05
56g_40d_0.7	36.44_36.55_35.84_36.31_34.43_34.48_36.42_36.83	35.91	0.94	0.12
64g_40d_0.8	43.79_45.43_46.33_47.81_46.27_43.75_43.91_	45.33	1.58	0.20
20g_14.39d_1	3.19_5.19_5.72_4.31_5.15_4.52_4.35_4.2	4.58	0.77	0.10
34g_17.18d_1	13.96_14.52_15.55_14.16_12.89_12.34_12.03_12.02	13.43	1.31	0.16
54g_20.04d_1	26.43_25.77_25.63_26.59_26.87_27.04_27.56_27.54	26.68	0.73	0.09
10g_25d_0.5[a]	1.51_2.26_2.18_1.57_1.38_1.36_1.96_2.29	1.81	0.40	0.05
10g_25d_0.5[a]	1.36_1.26_1.05_1.39_1.21_1.5_1.03_1.65	1.31	0.21	0.03
17g_30d_0.5[a]	5.56_4.98_4.28_4.57_4.9_4.47_5.28_5.58	4.95	0.49	0.06
17g_30d_0.5[a]	5.03_5.44_5.03_4.9_5.03_6.18_6.74_4.92	5.41	0.69	0.09
34g_30d_1[b]	24.24_23.71_23.5_24.03_24.5_24.86_25.11_24.43	24.30	0.55	0.07
[a] Repeatability tests				
[b] Cylindrical charge that was detonated at its centre				

B.2 Axial Shortening

Table B.2 presents the axial shortening measurements of each cylinder. These measurements were taken with a height gauge that had an accuracy of 0.01 mm. The original height of the cylinder (that is, 330 mm) was set as the datum. Note that the "**Error**" column presents the standard error of the averaged axial shortening of each cylinder. Measurements of the ruptured tubes were excluded here.

Table B.2: Axial Shortening Measurements

Charge	Concatenated Measurements	Average	Std Dev.	Error
All Axial Shortening Units in mm				
18g_25d_0.9	1.35_1.13_0.81_1.34_1.51_1.55_1.33_1.05	1.26	0.25	0.03
16g_25d_0.8	0.65_0.97_0.8_0.64_0.79_0.6_0.54_0.48	0.68	0.16	0.02
14g_25d_0.7	0.54_0.45_0.44_0.45_0.35_0.25_0.31_0.52	0.41	0.10	0.01
12g_25d_0.6	0.69_0.82_0.79_0.62_0.45_0.49_0.56_0.64	0.63	0.13	0.02
10g_25d_0.5	0.65_0.6_0.6_0.72_0.72_0.82_0.86_0.86	0.73	0.11	0.01
31g_30d_0.9	4.81_4.56_4.74_5_4.89_4.5_4.52_4.84	4.73	0.19	0.02
27g_30d_0.8	2.87_2.42_2.73_2.84_2.68_2.6_2.89_3.13	2.77	0.21	0.03
24g_30d_0.7	2.24_2.27_2.04_2_2.34_2.48_2.07_1.96	2.18	0.19	0.02
20g_30d_0.6	1.15_1.02_1.13_1.37_1.41_1.22_1.12_1.16	1.20	0.13	0.02
17g_30d_0.5	1.16_1.17_1.38_1.3_0.89_0.64_0.75_1.11	1.05	0.26	0.03
49g_35d_0.9	12.31_11.86_10.95_11.5_12.07_12.07_12.01_12.17	11.87	0.44	0.06
43g_35d_0.8	9.02_9.61_9.17_8.64_8.75_8.7_7.96_7.93	8.72	0.57	0.07
38g_35d_0.7	6.44_6.1_6.25_6.68_6.47_5.57_5.75_6.32	6.20	0.38	0.05
32g_35d_0.6	4.08_4.08_3.46_2.82_3.06_3.09_3.38_3.92	3.49	0.49	0.06
27g_35d_0.5	2.55_2.3_1.62_1.31_1.22_1.58_1.8_2.35	1.84	0.50	0.06
64g_40d_0.8	19.57_19.03_17.48_18.72_19.58_17.21_19.48_19.21	18.79	0.94	0.12
56g_40d_0.7	12.05_12.43_13.26_13.44_13.13_13.51_13.98_13.35	13.14	0.62	0.08
48g_40d_0.6	8.29_8.23_8.53_9.57_9.62_8.39_7.57_8.23	8.55	0.70	0.09
40g_40d_0.5	6.04_5.26_4.97_5.3_5.16_4.95_5.31_6.01	5.38	0.42	0.05
20g_14.39d_1	0.99_1.15_0.88_0.66_0.68_1.01_1.18_0.85	0.93	0.19	0.02
43g_25d_2.2	11.48_12.33_12.24_12.64_12.43_11.38_10.48_10.58	11.70	0.85	0.11
54g_35d_1	14.82_13.87_13.9_15.32_15.89_15.54_15.51_15.51	15.05	0.78	0.10
49g_25d_2.5	16.02_16.82_17.34_16.68_15.42_14.98_15.31_15.82	16.05	0.83	0.10
31g_25d_1.6	6.11_5.92_6.09_5.86_5.34_5.12_5.52_6.1	5.76	0.38	0.05
24g_25d_1.2	2.43_2.53_2.89_3.16_2.88_2.84_3.02_2.64	2.80	0.25	0.03
20g_25d_1	1.67_1.83_2.08_2.36_2.57_2.43_1.99_1.67	2.08	0.35	0.04
34g_30d_1	4.81_4.15_4.49_4.61_4.25_4.13_4.71_5.22	4.55	0.37	0.05
59g_35d_1.1	14.97_15.68_15.83_15.49_15.57_16_15.78_14.83	15.52	0.41	0.05
48g_30d_1.4	13.76_13.68_13.11_13.04_12.82_12.27_11.83_12.81	12.92	0.65	0.08
34g_17.18d_1	0.71_0.74_0.84_0.96_1.26_1.3_1.11_0.86	0.97	0.23	0.03
10g_25d_0.5[a]	0.22_0.23_0.33_0.21_0.2_0.19_0.14_0.16	0.21	0.06	0.01
10g_25d_0.5[a]	0.37_0.18_0.03_0.06_0.13_0.06_0.15_0.33	0.16	0.13	0.02
34g_30d_1[b]	5.96_5.26_4.62_4.78_4.72_4.84_5.35_5.62	5.14	0.48	0.06
54g_20.04d_1	8.28_7.79_8.24_8.52_7.85_7.83_8.54_9.11	8.27	0.45	0.06
17g_30d_0.5[a]	1.02_1.13_1.05_0.85_0.83_1_0.91_0.84	0.95	0.11	0.01
17g_30d_0.5[a]	0.71_0.74_0.84_0.96_1.26_1.3_1.11_0.86	0.97	0.23	0.03
54g_30d_1.6	17.41_17.89_18.16_18.94_19.54_19.12_17.97_16.99	18.25	0.88	0.11
[a] Repeatability tests				
[b] Cylindrical charge that was detonated at its centre				

Appendix C

Code

Reduced versions of the LS DYNA blast and quasi-static tensile test input decks are presented here. MATLAB codes of the averaged cylinder profile, the Richardson Extrapolation, and the simulated impulse calculator are presented in full.

C.1 LS DYNA Blast Keyword File (Base Units: g, mm, ms, and K)

The air (that is, ALE) mesh was defined as a four noded shell, where its corner coordinates (in clockwise order) were $(0, -1, 0)$, $(110, -1, 0)$, $(110, 310, 0)$, and $(0, 310, 0)$, where the element size was 1 mm. The cylinder (that is, Lagrangian) mesh was defined as a four noded shell, where its corner coordinates (also in clockwise order) were $(75, -30, 0)$, $(77, -30, 0)$, $(77, 300, 0)$, and $(75, 300, 0)$, where the element size was 0.25 mm. Note that node numbers of every element, coordinates of each node, element sets, and node sets were excluded to save paper. The keyfile was set up so that the user only needs to change the values in the "`PARAMETER`" key card. Where '`Val 1`' is the y coordinate of the initial detonation point, '`Val 2`' is the charge radius, and '`Val 3`' is the y coordinate of the lower charge face, and '`Val 4`' is the y coordinate of the upper charge face.

```
$# LS-DYNA Keyword file created by LS-PrePost(R) V4.3 (Beta) - 25May2015(09:00)
$# Created on Dec-23-2015 (14:18:44)
*KEYWORD MEMORY=134217728 NCPU=-1
*PARAMETER
$#   prmr1       val1     prmr2       val2     prmr3       val3     prmr4       val4
R     detp    161.000    R diam       20.0      R y1    134.000      R y2    166.000
*TITLE
$#                                                                               title
Sean Davids (DVDSEA004) Numerical Model
*CONTROL_ALE
$#     dct       nadv       meth       afac       bfac       cfac       dfac       efac
        -1          1          2       -1.0        0.0        0.0        0.0        0.0
$#   start        end      aafac      vfact       prit        ebc       pref    nsidebc
       0.01.00000E20        0.0        0.0          0          0     0.1013          0
$#    ncpl       nbkt     imascl     checkr
         1         50          0        0.0
*CONTROL_ENERGY
$#    hgen       rwen     slnten      rylen
         2          2          1          1
*CONTROL_TERMINATION
$#  endtim     endcyc      dtmin     endeng     endmas
       2.0          0        0.0        0.0        0.0
*CONTROL_TIMESTEP
$#  dtinit     tssfac       isdo     tslimt      dt2ms       lctm      erode      ms1st
       0.0        0.5          0        0.0        0.0          0          0          0
$#  dt2msf    dt2mslc      imscl     unused     unused      rmscl
       0.0          0          0                             0.0
*DATABASE_ELOUT
$#       dt     binary       lcur      ioopt    option1    option2    option3    option4
4.00000E-4          0          0          1          0          0          0          0
*DATABASE_NODOUT
$#       dt     binary       lcur      ioopt    option1    option2
4.00000E-4          0          0          1        0.0          0
*DATABASE_BINARY_D3PLOT
$#       dt       lcdt       beam      npltc     psetid
      0.01          0          0          0          0
$#    ioopt
         0
*DATABASE_HISTORY_NODE_SET
```

```
$#     id1       id2       id3       id4       id5       id6       id7       id8
         5         0         0         0         0         0         0         0
*DATABASE_HISTORY_SHELL_SET
$#     id1       id2       id3       id4       id5       id6       id7       id8
         1         0         0         0         0         0         0         0
*BOUNDARY_SPC_SET
$#    nsid       cid      dofx      dofy      dofz     dofrx     dofry     dofrz
         3         0         0         1         0         0         0         0
*SET_NODE_LIST_TITLE
Reflective_Boundary
$#     sid       da1       da2       da3       da4    solver
         3       0.0       0.0       0.0       0.0MECH
*BOUNDARY_SPC_SET
$#    nsid       cid      dofx      dofy      dofz     dofrx     dofry     dofrz
         4         0         1         0         0         0         0         0
*SET_NODE_LIST_TITLE
CLAMP
$#     sid       da1       da2       da3       da4    solver
         4       0.0       0.0       0.0       0.0MECH
*EOS_LINEAR_POLYNOMIAL_TITLE
AIR_EOS
$#   eosid        c0        c1        c2        c3        c4        c5        c6
         1       0.0       0.0       0.0       0.00.400000010.40000001       0.0
$#      e0        v0
      0.25       1.0
*EOS_GRUNEISEN_TITLE
CYLINDER
$#   eosid         c         s1        s2        s3     gamao         a         e0
         2    4570.0       1.49       0.0       0.0 1.9299999       0.5       0.0
$#      v0
       1.0
*EOS_JWL_TITLE
PE4_EOS
$#   eosid         a          b        r1        r2      omeg        e0        vo
         3  609800.0   12950.0       4.5       1.4      0.25    9000.0       1.0
*SET_NODE_LIST_TITLE
CYLINDER_PROFILE
$#     sid       da1       da2       da3       da4    solver
         5       0.0       0.0       0.0       0.0MECH
*SET_PART_LIST_TITLE
CYLINDER_PART_LIST
$#     sid       da1       da2       da3       da4    solver
         2       0.0       0.0       0.0       0.0MECH
$#    pid1      pid2      pid3      pid4      pid5      pid6      pid7      pid8
         2         0         0         0         0         0         0         0
*SET_PART_LIST_TITLE
AIR_PE4_PART_LIST
$#     sid       da1       da2       da3       da4    solver
       103       0.0       0.0       0.0       0.0MECH
$#    pid1      pid2      pid3      pid4      pid5      pid6      pid7      pid8
         1         3         0         0         0         0         0         0
*SET_SHELL_LIST_TITLE
Impulse
$#     sid       da1       da2       da3       da4
```

```
         1       0.0       0.0       0.0       0.0
*SET_MULTI_MATERIAL_GROUP_LIST_TITLE
AIR_MULTI_MATERIAL_GROUP_LIST
$#  ammsid
         1
$# ammgid1   ammgid2   ammgid3   ammgid4   ammgid5   ammgid6   ammgid7   ammgid8
         1         0         0         0         0         0         0         0
*SET_MULTI_MATERIAL_GROUP_LIST_TITLE
PE4_MULTI_MATERIAL_GROUP_LIST
$#  ammsid
         2
$# ammgid1   ammgid2   ammgid3   ammgid4   ammgid5   ammgid6   ammgid7   ammgid8
         2         0         0         0         0         0         0         0
*PART
$#                                                                         title
AIR
$#     pid     secid       mid     eosid      hgid      grav    adpopt      tmid
         1         1         1         1         1         0         0         0
*SECTION_ALE2D_TITLE
AIR_SECTION
$#   secid   aleform      aet     elform
         1        11         0        14
*MAT_NULL_TITLE
AIR_MATERIAL
$#     mid        ro        pc        mu     terod     cerod        ym        pr
         11.29300E-6       0.0       0.0       0.0       0.0       0.0       0.0
*HOURGLASS_TITLE
FLUID_HOURGLASS
$#    hgid       ihq        qm       ibq        q1        q2    qb/vdc        qw
         1         11.00000E-6         1       1.5      0.06       0.1       0.1
*PART
$#                                                                         title
CYLINDER
$#     pid     secid       mid     eosid      hgid      grav    adpopt      tmid
         2         2         2         2         0         0         0         0
*SECTION_SHELL_TITLE
CYLINDER
$#   secid    elform      shrf       nip     propt   qr/irid     icomp     setyp
         2        140.83333331         1       1.0         0         0         1
$#      t1        t2        t3        t4      nloc     marea      idof    edgset
       2.0       2.0       2.0       2.0       0.0       0.0       0.0         0
*MAT_JOHNSON_COOK_STOCHASTIC_TITLE
CYLINDER_MATERIAL
$#     mid        ro         g         e        pr       dtf        vp    rateop
         2    0.0079   77000.0  200000.00.30000001       0.0       0.0       0.0
$#       a         b         n         c         m        tm        tr      epso
 280.98001   1319.950.86000001      0.070.89999998    1673.0     293.01.00000E-6
$#      cp        pc     spall        it        d1        d2        d3        d4
     440.0       0.0       2.0       0.0       0.0       0.0       0.0       0.0
$#      d5      c2/p      erod     efmin
       0.0       0.0         01.00000E-6
*PART
$#                                                                         title
PE4
```

```
$#     pid      secid        mid      eosid       hgid       grav     adpopt       tmid
         3          3          3          3          1          0          0          0
*SECTION_ALE2D_TITLE
PE4_SECTION
$#   secid    aleform       aet     elform
         3         11          0         14
*MAT_HIGH_EXPLOSIVE_BURN_TITLE
PE4_MATERIAL
$#     mid         ro          d        pcj       beta          k          g       sigy
         3  0.001601    8193.0   28000.0        2.0        0.0        0.0        0.0
*ALE_MULTI-MATERIAL_GROUP
$#     sid     idtype     gpname
         1          1AIR
         3          1PE4
*INITIAL_DETONATION
$#     pid          x          y          z         lt
         3        0.0     &detp        0.0        0.0
*INITIAL_VOLUME_FRACTION_GEOMETRY
$#   fmsid    fmidtyp     bammg     ntrace
         1          1          1         50
$# conttyp    fillopt     fammg         vx         xy         xz     radvel     unused
         5          0          2        0.0        0.0        0.0          0
$#    xmin       ymin       zmin       xmax       ymax       zmax     unused     unused
       0.0        &y1        0.0      &diam        &y2        0.0
*CONSTRAINED_LAGRANGE_IN_SOLID_TITLE
$#  coupid                                                                        title
         0FSI
$#   slave     master      sstyp      mstyp      nquad      ctype      direc      mcoup
         2        103          0          0          1          4          2         -1
$#   start        end       pfac       fric     frcmin       norm    normtyp       damp
       0.01.00000E10        0.1        0.0        0.1          0          0        0.0
$#      cq       hmin       hmax      ileak      pleak    lcidpor      nvent   blockage
       0.0        0.0        0.0          2        0.1          0          0          0
$#  iboxid    ipenchk    intforc    ialesof     lagmul     pfacmm       thkf
         0          0          0          0        0.0          0        2.0
*CONSTRAINED_LAGRANGE_IN_SOLID_TITLE
$#  coupid                                                                        title
         0FSI
$#   slave     master      sstyp      mstyp      nquad      ctype      direc      mcoup
         2        103          0          0          1          4          2         -2
$#   start        end       pfac       fric     frcmin       norm    normtyp       damp
       0.01.00000E10        0.1        0.0        0.1          0          0        0.0
$#      cq       hmin       hmax      ileak      pleak    lcidpor      nvent   blockage
       0.0        0.0        0.0          2        0.1          0          0          0
$#  iboxid    ipenchk    intforc    ialesof     lagmul     pfacmm       thkf
         0          0          0          0        0.0          0        2.0
```

C.2 Averaged Cylinder Profile

```
function...
    [max_diametric_deflection, shortening] = CylinderProfile(filename, h)
```

```
%THE USER MUST KNOW THE FILENAME, AND THE ELEMENT SIZE THAT WENT WITH IT

format long

%WHERE filename is the name of the csv file (e.g. 'XXX.csv)
%WHERE h is the size of the Lagrangian element (mm)

M = csvread(filename, 2, 0);
%Importing the .csv file to create a matrix called M.
%Reading from the third row and the first column to the end

Time = M(:, 1); %Extracting the times (ms)
X = M(:, 2:330/h + 2); %Extracting the x coordinates (mm)
SX = size(X);
Y = M(:, 330/h + 3:end - 1); %Extracting the y coordinates (mm)
SY = size(Y);
Y_SHIFT = Y + 30; %Shifting the y coordinated by 30 mm

A = zeros(330/h + 1, 2);
%Initialising a matrix
%Row 1 contains the average x coordinate of each node
%Row 2 contains the average y coordinate of each node

%Averaging the transient deflections of each node from half the simulated
%time to the simulated time
for j =  1:330/h + 1

    for i = round(0.5*length(Time)):length(Time)

        A(j, 1) = mean(X(i, j));
        A(j, 2) = mean(Y_SHIFT(i, j));

    end

end


%Plotting the averaged cylinder profile
figure
plot(A(:, 1), A(:, 2)), grid
axis([0, 154, 0, 330])
title('Averaged Cylinder profile')

csvwrite('Cylinder_Profile.csv', A, 0, 0)
%Exporting the averaged x (row 1) and y (row 2) coordinates to a csv file

%Physical quantities that our outputted to screen
max_diametric_deflection = 2*(max(A(:, 1)) - 77);
shortening = 330 - (max(A(:, 2)) - min(A(:, 2)))

end
```

C.3 Richardson Extrapolation

```
%Richardson Extrapolation Code
%Author: Sean Davids
%Student Number: DVDSEA004

%This code is based on the paper by Roache (1997):
%QUANTIFICATION OF UNCERTAINTY IN COMPUTATIONAL FLUID DYNAMICS

function[fextrap, Accuracy] = Richardson_Extrapolation(f1, f2, f3, h3,...
    h2, h1)

format long

%f1 is coarse mesh numerical solution
%f2 is intermediate mesh numerical solution
%f3 is fine mesh numerical solution
%h3 is coarse grid spacing (i.e. element size)
%h2 is intermediate grid spacing
%h1 is fine grid spacing

f = [f1, f2, f3];

r12 = h2/h1;
r23 = h3/h2;
r = [r12, r23]; %Grid refinement ratio vector

epsilon12 = f2 - f1; %Numerical solution difference
epsilon23 = f3 - f2; %Numerical solution difference

omega = 0.5; %Relaxation factor

iterations = 200; %Maximum number of interations

p = zeros(1, iterations); %Order of accuracy vector
p(1) = 2;
beta = zeros(1, iterations); %Mesh refinement ratio vector

fextrap = zeros(1, 2); %The extrapolated values vector

for i = 1:length(r) %Looping through the grid refinement ratio vector

    for j = 1:length(p) %Looping through the order of accuracy vector

        beta(j) = ((r12^p(j) - 1)*epsilon23)/((r23^p(j) - 1)*epsilon12);

        p(j + 1) = omega*p(j) + (1 - omega)*log(beta(j))/log(r(i));

        if p(j + 1) - p(j) == 0 %If the order of accuracy converges EXIT

            break
```

```
        end

    end

    fextrap(i) = f(i) + (f(i) - f(i + 1))/(r(i)^p(j) - 1);
    %EXTRAPOLATED VALUES
    %First value is fextrap23
    %Second value is fextrap12

    Accuracy = [100*(f1/fextrap(1)) 100*(f1/fextrap(2))
        100*(f2/fextrap(1)) 100*(f2/fextrap(2))
        100*(f3/fextrap(1)) 100*(f3/fextrap(2))];
    %ACCURACY MATRIX
    %First column contains the accuracies relative to fextrap(1)
    %Second column contains the accuracies relative to fextrap(2)

end

end
```

C.4 Pendulum-Oscilloscope Impulse Calculator

```
function[I] = Oscilloscope(filename, M)

format long

%M is the mass of the ballistic pendulum

A = csvread(filename, 3, 0); %Importing the csv file

pi = 3.14159265359; %The pi constant

t = A(:, 1); %Time vector (s)
V = A(:, 2); %Voltage vector (V)
lw = 2.9; %Wire length (m)
g = 9.81; %Gravitational acceleration (m/s^2)
Td = 2*pi*sqrt(lw/g); %Pendulum period (s)

d = (30*V - 150)/1000;
%Converting the voltage into displacement (mm)

x1 = abs(max(d))
x2 = abs(min(d))
beta = (2/Td)*log(x1/x2);
v0 = 2*pi*x1*exp(0.25*beta*Td)/Td;
I = M*v0;

plot(t, d), grid

end
```

Appendix D

Assessment of Ethics in Research Projects Form

EBE Faculty: Assessment of Ethics in Research Projects

Any person planning to undertake research in the Faculty of Engineering and the Built Environment at the University of Cape Town is required to complete this form before collecting or analysing data. When completed it should be submitted to the supervisor (where applicable) and from there to the Head of Department. If any of the questions below have been answered YES, and the applicant is NOT a fourth year student, the Head should forward this form for approval by the Faculty EIR committee: submit to Ms Zulpha Geyer (Zulpha.Geyer@uct.ac.za; Chem Eng Building, Ph 021 650 4791). Students must include a copy of the completed form with the thesis when it is submitted for examination.

Name of Principal Researcher/Student: Sean Davids Department: MECH ENG.

If a Student: Degree: MSc Mech. Eng. Supervisor: G S LANGDON

If a Research Contract indicate source of funding/sponsorship:

Research Project Title: Response of tubes subjected to internal blast loading

Overview of ethics issues in your research project:

Question 1: Is there a possibility that your research could cause harm to a third party (i.e. a person not involved in your project)?	YES	(NO)
Question 2: Is your research making use of human subjects as sources of data? If your answer is YES, please complete Addendum 2.	YES	(NO)
Question 3: Does your research involve the participation of or provision of services to communities? If your answer is YES, please complete Addendum 3.	YES	(NO)
Question 4: If your research is sponsored, is there any potential for conflicts of interest? If your answer is YES, please complete Addendum 4.	YES	(NO)

If you have answered YES to any of the above questions, please append a copy of your research proposal, as well as any interview schedules or questionnaires (Addendum 1) and please complete further addenda as appropriate.

I hereby undertake to carry out my research in such a way that

- there is no apparent legal objection to the nature or the method of research; and
- the research will not compromise staff or students or the other responsibilities of the University;
- the stated objective will be achieved, and the findings will have a high degree of validity;
- limitations and alternative interpretations will be considered;
- the findings could be subject to peer review and publicly available; and
- I will comply with the conventions of copyright and avoid any practice that would constitute plagiarism.

Signed by:

	Full name and signature	Date
Principal Researcher/Student:	Sean Andrew Davids	30/01/2015

This application is approved by:

Supervisor (if applicable): G S LANGDON		29-1-2015
HOD (or delegated nominee): Final authority for all assessments with NO to all questions and for all undergraduate research.		03/02/2015
Chair : Faculty EIR Committee For applicants other than undergraduate students who have answered YES to any of the above questions.		

ADDENDUM 1:
Please append a copy of the research proposal here, as well as any interview schedules or questionnaires:

ADDENDUM 2: To be completed if you answered YES to Question 2:

It is assumed that you have read the UCT Code for Research involving Human Subjects (available at http://web.uct.ac.za/depts/educate/download/uctcodeforresearchinvolvinghumansubjects.pdf) in order to be able to answer the questions in this addendum.

2.1 Does the research discriminate against participation by individuals, or differentiate between participants, on the grounds of gender, race or ethnic group, age range, religion, income, handicap, illness or any similar classification?	YES	NO
2.2 Does the research require the participation of socially or physically vulnerable people (children, aged, disabled, etc) or legally restricted groups?	YES	NO
2.3 Will you not be able to secure the informed consent of all participants in the research? (In the case of children, will you not be able to obtain the consent of their guardians or parents?)	YES	NO
2.4 Will any confidential data be collected or will identifiable records of individuals be kept?	YES	NO
2.5 In reporting on this research is there any possibility that you will not be able to keep the identities of the individuals involved anonymous?	YES	NO
2.6 Are there any foreseeable risks of physical, psychological or social harm to participants that might occur in the course of the research?	YES	NO
2.7 Does the research include making payments or giving gifts to any participants?	YES	NO

If you have answered YES to any of these questions, please describe how you plan to address these issues (append to form):

ADDENDUM 3: To be completed if you answered YES to Question 3:

3.1 Is the community expected to make decisions for, during or based on the research?	YES	NO
3.2 At the end of the research will any economic or social process be terminated or left unsupported, or equipment or facilities used in the research be recovered from the participants or community?	YES	NO
3.3 Will any service be provided at a level below the generally accepted standards?	YES	NO

If you have answered YES to any of these questions, please describe how you plan to address these issues (append to form)

ADDENDUM 4: To be completed if you answered YES to Question 4

4.1 Is there any existing or potential conflict of interest between a research sponsor, academic supervisor, other researchers or participants?	YES	NO
4.2 Will information that reveals the identity of participants be supplied to a research sponsor, other than with the permission of the individuals?	YES	NO
4.3 Does the proposed research potentially conflict with the research of any other individual or group within the University?	YES	NO

If you have answered YES to any of these questions, please describe how you plan to address these issues(append to form)